POLITECNICO DI TORINO

Master of Science in Energy and Nuclear Engineering

Rational Energy Use

"Development of a mathematical model for area sizing and performance estimation of a Parabolic Troughs Solar Field"

Supervisor:

Prof. Eliodoro Chiavazzo

Candidate:

Sergio Murro

Co-supervisors:

Prof. Chris Sansom

Dr. Peter King

Academic Year: 2019-2020

Table of content

Abstract

CSP technology is a powerful and smart way that allows to produce power by using mirrors to concentrate solar beams on a small area. This thesis work is focused on theorizing and estimating the performance of a parabolic trough solar field not only from a theoretical point of view but also from a practical one through a Matlab model developed with the help of two professors from department of Water, Energy and Environment of the Cranfield University. Such technology is already in use, and a new one is currently under construction Solar field in NEOM, Saudi Arabia, intended to fuel a Multiple Effect Desalination Water Plant with the help of a thermal storage system. A preliminary analysis, along with the processing of the weather data (specifically, from the meteorological years between 2005 and 2017) has been done in order to gather the necessary information that will allow to develop the best tracking strategy. Along with the yearly weather data, the other main parameters taken into consideration for the development of the model have concerned the inherent features proper of the material and the structure, specifically: geometrical and materials specifications of the collector, the temperature difference between inlet and outlet, number of parallel collector's rows, the spacing between each one of them and the tracking strategy adopted. The same model with a proper different code setup can predict and estimate the reflective area needed to achieve specific design user's requests. The model can estimate the concentrated power $\dot{Q}_{conc}$ along with all the losses involved in the process. As a consequence it is possible thus to calculate the actual useful power (the one absorbed by the heat transfer fluid) $\dot{Q}_{use}$. For this purpose, a very detailed sun tracking model has been implemented as well as another one for the shading losses which depends on the collectors' movements. Optical performances and inaccuracies have been also taken into account and estimated, and in particular a delicate step was the evaluation of the so-called "Intercept Factor" through a statistical approach. Another very detailed approach has been necessary for the evaluation of the heat exchange involved at the receiver: for this purpose a non-linear equation system has been implemented, to be solved with a proper Matlab function. At first, this system is solved multiple times (iteratively, using the Bisection method) for the calculation of the mass flow rate needed to achieve a correct temperature difference, then for the actual performance. The sizing calculation led to results very close to the initial rough estimations, with the user requirements having been the following ones: the temperature difference between the inlet and the outlet section of the field (300° inlet,380°C outlet), some working power value for a specific percentage time the year. Several parametrical studies have been made, a very important one is the spacing sensitivity analysis: the effect of the distance between each row on the annual energy collected has been analyzed. Results showed that by increasing too much this distance no significative gains are obtained. In conclusion, results has been satisfactory and suitable for the sizing and optimization of the Solar Field in NEOM under construction.

1 – Introduction

While the availability of fossil fuels decreases from year to year, there is, at the same time, growing demand for clean and sustainable renewable energy to meet the growing energy needs.

The Sun, the largest source of zero-emission energy, provides the Earth with more energy in an hour than it consumes in a year. Despite this, at the moment, solar energy provides only a very small fraction of the world total energy requirements. A good challenge for research is in the collection and storage for the generation of electrical or thermal power.

There are several ways to collect solar energy, three are the main macro groups:

- Solar thermal panels
- Photovoltaic panels
- Concentrated Solar power (CSP)

Solar thermal are used to convert solar energy into thermal energy by heating up a thermal storage system, usually they can use either forced convection or natural convection. Photovoltaic panels convert solar energy in electrical energy by means of the Photoelectric Effect. These two technologies are widely used in civil applications.

CSP technology essentially uses mirrors and lenses to redirect the solar beams and concentrate them in a medium which can usually be a heat transfer fluid. Some of the possible applications are: feeding a turbine or a thermal engine for electricity production, producing thermal energy by heating up a thermal storage system…etc. Despite the principle being relatively simple, the CSP presents several applicative options which must be carefully selected depending on the case.

One of the most common way to apply this technology is the use of Parabolic Troughs collectors. Such mirrors can rotate on a single axis and track the Sun, concentrating the beams on a linear receiver tube (for this reason they are also called “Linear collectors”) which is positioned in the focal point of the parabola. Inside the tube a liquid flows (called “Heat Transfer Fluid”, HTF) that absorbs the energy and moves it in an heat exchanger and/or in a heat storage system.

This Thesis work is about the development of a mathematical model on the software Matlab which allows to size a Parabolic Trough Solar Field and estimate as much as possible the performances of such a plant.

The work was carried out thanks also to the help of the staff of the "School of Water, Energy and Environment" department of the Cranfield University and turned out to be useful for the sizing and design of a solar field currently under construction in NEOM, Saudi Arabia, an industrial city under construction in the province of Tabuk. This field supplies power to a 3-stage MED (Multiple Effect Distillation) saltwater desalination plant, the first of them is a solar dome with additional reflecting heliostats.

In this report a consistent literature review is provided as well as the model development with a large discussion of the results obtained.

Main steps of the model development regarded the theoretical study of every factor influencing the collected amount of energy. In the software implementation of the model, particular attention was paid to the following points:

- Evaluation of the solar angles (Sun position in the sky);
- Weather data analysis in the target location;
- Sun tracking strategy;
- Study of any possible optical imperfection disrupting the perfect absorption of sunlight by the absorber, with particular attention to the shading phenomenon caused by the spatial proximity of two collectors;
- Thermodynamic analysis of the receiver with useful heat evaluation and thermal losses;
- Evaluation of the figures of merit and validation of the results.

Figure 1 – Location on the map of the solar field.

Figure 2 – Working site in the solar field location.

2 – Literature review

2.1 – Available Solar energy

In this paragraph a detailed review of everything about the available energy incoming from the Sun is provided. Most of the information in this paragraph can be found in [1].

2.1.1 – The Solar Constant

The Sun is an extremely hot sphere made of gaseous matter with a diameter of $1.39 \times 10^9 m$, it is away from the Earth, on average, $1.5 \times 10^{11} m$ ($1\ au$), it turns out to have an effective blackbody temperature of $5777\ K$. The energy emitted by the sun is the result of different nuclear fusion reactions happening in the solar core, the most important one happens when hydrogen (4 protons) combines and produce helium with a certain mass loss which is transformed into energy according to Einstein's Law. $E = mc^2$.

The emitted radiation by the Sun along with its distance from the Earth results in an intensity of extraterrestrial radiation called *Solar Constant* G_{sc}.

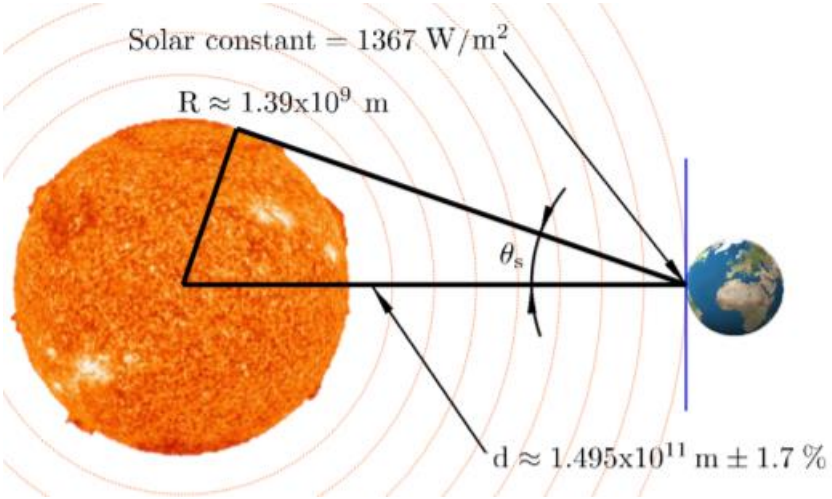

Figure 3 - Sun-earth relationships [D. Rodriguez (2017)]

Solar Constant is defined as: the thermal power received out of the atmosphere per unit area normal to the propagation direction of the radiation, being everything calculated at the average distance between Sun and Earth. *World Radiation Center* (WRC) uses a value of $1367\ W/m^2$ with a relative percentage error of *1%*. This is the value used in this report.

As well as the total energy received, it is also important to know the spectral distribution of the extraterrestrial radiation which is the one we would receive in absence of the atmosphere. The standard spectral curve has been drawn by means of high-altitudes space measurements.

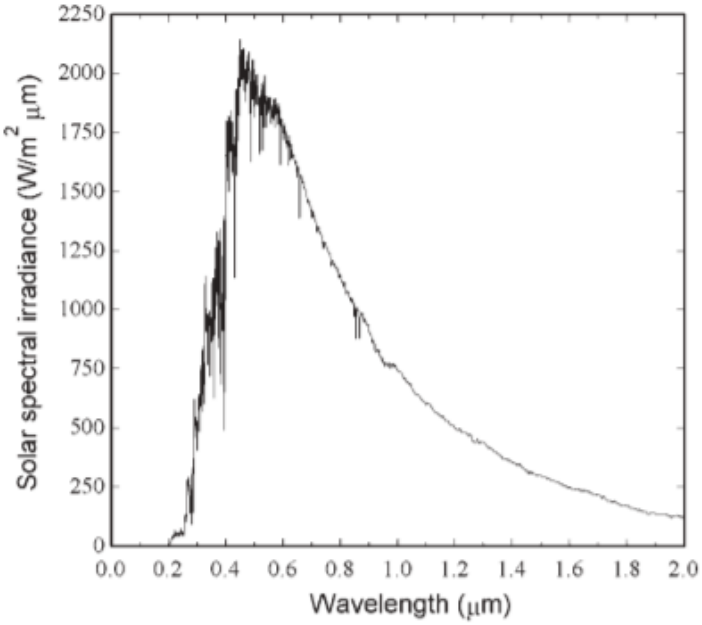

Figure 4 - The WRC standard spectral irradiance curve at mean earth-sun distance [J. A. Duffie et al.].

The following table provides the same information of the previous graph in numbers. The average energy $G_{sc,\lambda}$ (in $W/m^2\mu m$), over small bands centered in wavelength λ are reported in the second column. The fraction $f_{0-\lambda}$ of the total energy of the whole spectrum that is between wavelength 0 e λ is listed in the third column.

λ (μm)	$G_{sc,\lambda}$ (W/m^2 μm)	$f_{0-\lambda}$ (−)	λ (μm)	$G_{sc,\lambda}$ (W/m^2 μm)	$f_{0-\lambda}$ (−)	λ (μm)	$G_{sc,\lambda}$ (W/m^2 μm)	$f_{0-\lambda}$ (−)
0.250	81.2	0.001	0.520	1849.7	0.243	0.880	955.0	0.622
0.275	265.0	0.004	0.530	1882.8	0.257	0.900	908.9	0.636
0.300	499.4	0.011	0.540	1877.8	0.271	0.920	847.5	0.648
0.325	760.2	0.023	0.550	1860.0	0.284	0.940	799.8	0.660
0.340	955.5	0.033	0.560	1847.5	0.298	0.960	771.1	0.672
0.350	955.6	0.040	0.570	1842.5	0.312	0.980	799.1	0.683
0.360	1053.1	0.047	0.580	1826.9	0.325	1.000	753.2	0.695
0.370	1116.2	0.056	0.590	1797.5	0.338	1.050	672.4	0.721
0.380	1051.6	0.064	0.600	1748.8	0.351	1.100	574.9	0.744
0.390	1077.5	0.071	0.620	1738.8	0.377	1.200	507.5	0.785
0.400	1422.8	0.080	0.640	1658.7	0.402	1.300	427.5	0.819
0.410	1710.0	0.092	0.660	1550.0	0.425	1.400	355.0	0.847
0.420	1687.2	0.105	0.680	1490.2	0.448	1.500	297.8	0.871
0.430	1667.5	0.116	0.700	1413.8	0.469	1.600	231.7	0.891
0.440	1825.0	0.129	0.720	1348.6	0.489	1.800	173.8	0.921
0.450	1992.8	0.143	0.740	1292.7	0.508	2.000	91.6	0.942
0.460	2022.8	0.158	0.760	1235.0	0.527	2.500	54.3	0.968
0.470	2015.0	0.173	0.780	1182.3	0.544	3.000	26.5	0.981
0.480	1975.6	0.188	0.800	1133.6	0.561	3.500	15.0	0.988
0.490	1940.6	0.202	0.820	1085.0	0.578	4.000	7.7	0.992
0.500	1932.2	0.216	0.840	1027.7	0.593	5.000	2.5	0.996
0.510	1869.1	0.230	0.860	980.0	0.608	8.000	1.0	0.999

[a] $G_{sc,\lambda}$ is the average solar irradiance over the interval from the middle of the preceding wavelength interval to the middle of the following wavelength interval. For example, at 0.600 μm. 1748.8 W/m^2 μm is the average value between 0.595 and 0.610 μm.

Figure 5 - Extraterrestrial Solar Irradiance (WRC Spectrum) in Increments of Wavelength [J. A. Duffie et al.]

2.1.2 – Spectral distribution of extraterrestrial radiation

Solar radiation data can be available in different ways. Here the most common:

- They can be instantaneous (Irradiance) or integrals over a given period of time (Irradiation), usually daily or hourly;
- They can be beam, diffuse or total radiation;
- Depending on the instrument used for the detection;
- The surface orientation (usually beam or horizontal);
- If they are averaged, the average period.

Most of the data available are referred to horizontal surfaces and detected with thermopile pyranometers or detected by means of the satellite.

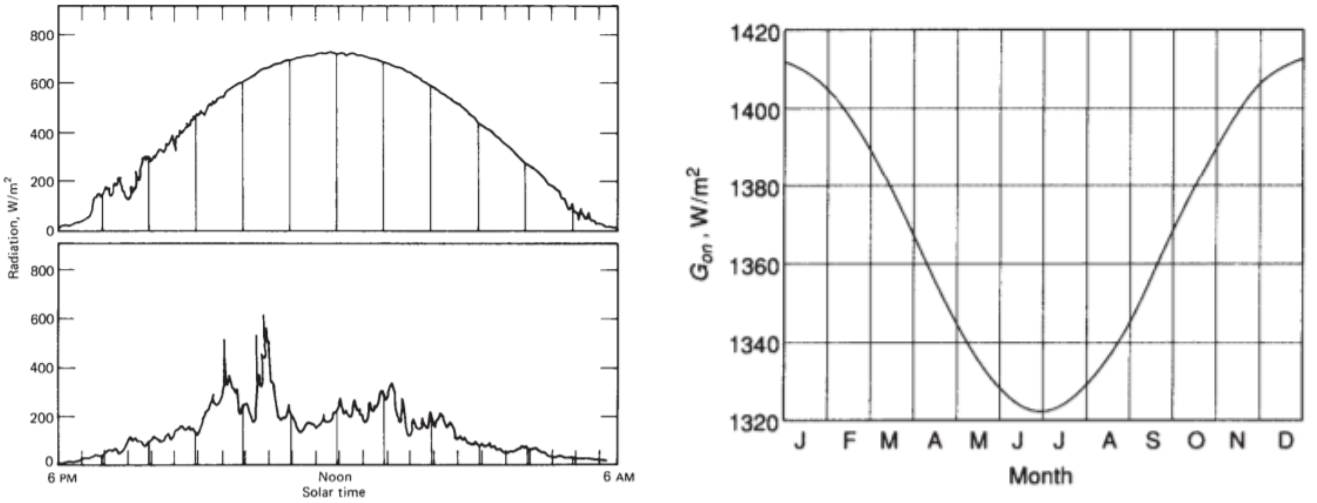

Figure 6 - (Left) Total (beam and diffuse) solar radiation on a horizontal surface versus time for clear and largely cloudy day, latitude 43°, for days near equinox. (Right) Variation of extraterrestrial solar radiation with time of year. [J. A. Duffie et al.]

Beam radiation received by a collector is lowered, with respect to the extraterrestrial radiation, by the variation of the extraterrestrial radiation and two very important phenomena:

- Scattering of radiation caused by interaction with air molecules, water droplets and dust. Main factors used to determine how this affect the attenuation are the number of molecules the beam must pass through and the particle size, which is related with the beam wavelength. An important value in this topic is the $Air\ Mass\ m$:

$$m = \frac{1}{\cos(\theta)}$$

  This represents the ratio of the mass of the atmosphere the beam must pass through divided by the same one calculated when the Sun is at Zenith (at sea level, Sun at Zenith, *m = 1*). Air molecules size is very small compared to the wavelength, and since Rayleigh scattering law

depends on λ^{-4}, the spectral band above $0.6\,\mu m$ has not that much of effect on the atmospheric attenuation. Dust and water particles are generally larger resulting in a more complex approach, one of the best model available is given by the Angstrom's turbidity equation for the atmospheric transmittance:

$$\tau_{a,\lambda} = \exp(-\beta\lambda^{-\alpha}m)$$

Being β is the Turbidity coefficient (0 = very clean , 0.4 = very turbid atmospheres) , α the lumped wavelength exponent (1.3 is commonly used), λ the wavelength [µm], and m the air mass along the path. β and α vary depending on the atmospheric conditions.

- Absorption is especially due to ozone (ultraviolet band), water vapor and carbon dioxide (infrared band). At the summit of the atmosphere there is almost total absorption of the short-wave radiation (lower than 0.29 µm). Water vapor absorbs mostly in the spectral band with wavelength centered in 1.0, 1.4 and 1.8 µm.

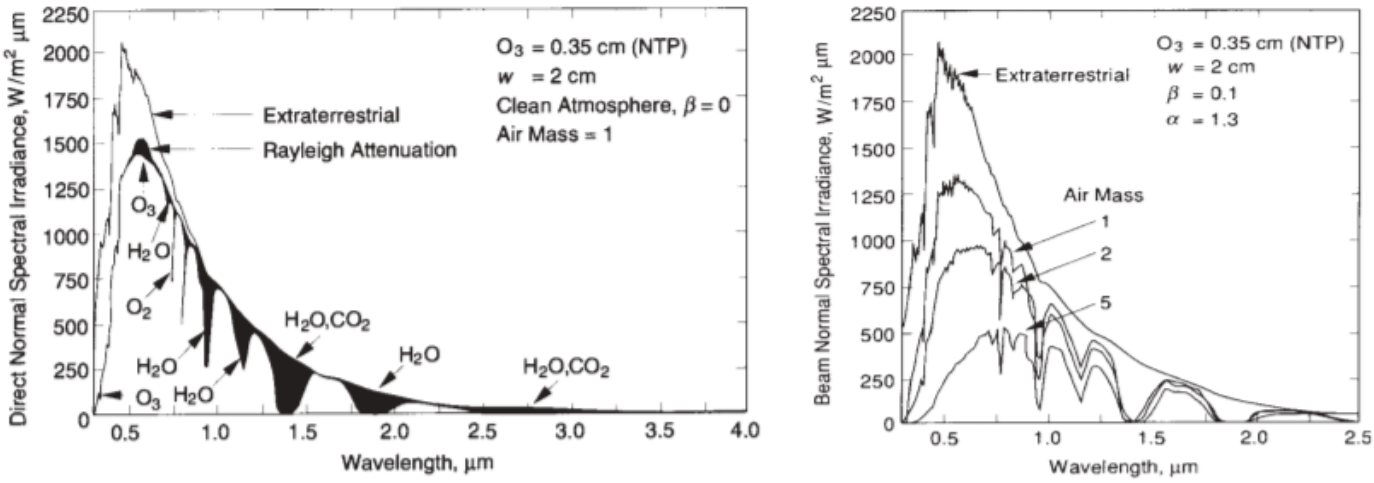

Figure 7 - (Left) An example of the effects of Raleigh scattering and atmospheric absorption on the spectral distribution of beam irradiance. (Right) An example of spectral distribution of beam irradiance for air masses of 0, 1, 2, and 5. [J. A. Duffie et al.]

For λ > 2.5 µm even the extraterrestrial represents just the 5% of the total radiation and there is almost no energy hitting the ground. The Rayleigh scattering phenomena in the figure is represented by the huge difference at those peaks around 0.5-0.6 µm.

An analogy can be seen in the total radiation's spectral distribution and that of diffuse radiation especially at short wavelength (0.35 – 0.80 μm). The diffuse radiation shows a pretty similar distribution but translated to the short wave range of the spectrum, this can be explained with the scattering theory (scattering especially at shorter wavelength). Calculation made by Iqbal (1983)

pointed out that, for usual weather conditions (like the figure), for wavelength higher than 1 µm, the almost complete radiation is beam.

So said, it can be concluded that for most practical purposes, the wavelength distribution range of the diffuse and beam radiation can be considered the same and is basically between 0.29 and 2.5 μm.

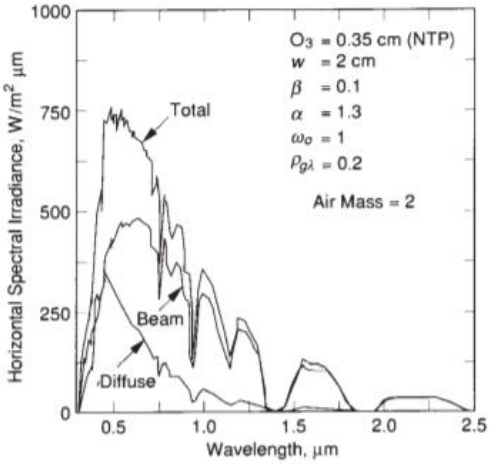

Figure 8 - An example of calculated total, beam, and diffuse spectral irradiances on a horizontal surface for typical clear atmosphere [J. A. Duffie et al.]

2.1.3 – Sky models

Two important definition should be now introduced:

- Beam/Direct Radiation I_b: radiation received from the Sun that is not scattered by the atmosphere and is directed along the joining line between the observer and the Sun.
- Diffuse Radiation I_d: radiation received from the Sun whose direction is changed by the scattering with atmosphere.

Such figures are present in every climate data file. However they are presented in other ways, which means referred to tilted surfaces:

- DNI (Direct Normal Irradiance): direct radiation, referred to a surface normal to the direction of the joining line between the observer and the Sun;
- DHI (Diffuse Horizontal Irradiance): diffuse radiation, referred to an horizontal surface;
- GHI (Global Horizontal Irradiance): total incoming radiation from the Sun, referred to an horizontal surface. It is defined as follows:

$$GHI = DHI + DNI * \cos(\vartheta_z)$$

Each of these radiative terms can be applied on a frequency band of the Solar Spectrum.

In order to evaluate, for a practical purpose, the available energy coming from the Sun, it is necessary to estimate the solar radiation on a given tilted surface which is in our case the collector. For a generally tilted surface of area A_c:

$$A_c I_T = I_b R_b A_c + I_{d,iso} A_s F_{s-c} + I_{d,cs} R_b A_c + I_{d,hz} A_{hz} F_{hz-c} + \sum_i I_i \rho_i A_i F_{i-c}$$

The first term is the beam radiation, the second one is the diffuse isotropic (being A_s and F_{s-c} the sky undefined area and the view factor), the third is the circumsolar coming from the same direction as the beam, the fourth is the horizon diffuse radiation coming from the undefined Horizon Area (the thin band in the figure) A_{hz}. The last term is the sum of all the reflected radiations streams (such as buildings, ground,…etc), surfaces are assumed to be diffuse reflective.

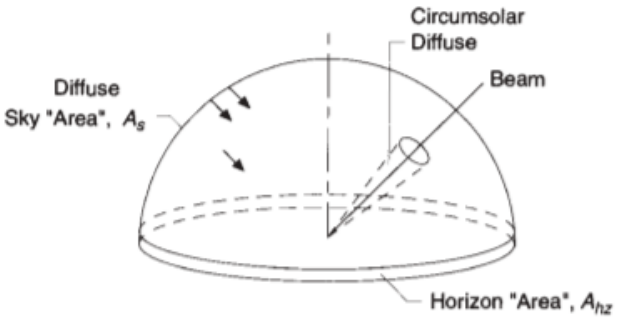

Figure 9 - Schematic of the distribution of diffuse radiation over the sky dome showing the circumsolar and horizon brightening components added to the isotropic component. [J. A. Duffie et al.]

R_b is the geometric factor, it must be included every time when data referred to horizontal surfaces are available, it is defined as the ratio of the radiation on the tilted surface to that on the horizontal one:

$$R_b = \frac{G_{bt}}{G_b} = \frac{G_{bn}\cos(\theta)}{G_{bn}\cos(\theta_z)} = \frac{\cos(\theta)}{\cos(\theta_z)}$$

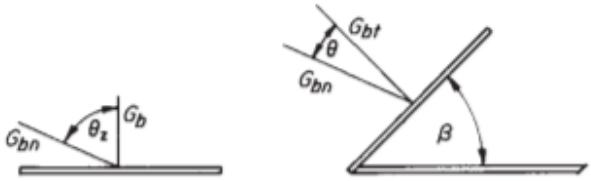

By assuming, for the last term, a huge reflective ground, by interchanging view factors and areas and canceling the common A_c, we obtain an equation which parameters can be calculated either empirically or theoretically:

$$I_T = I_b R_b + I_{d,iso} F_{c-s} + I_{d,cs} R_b + I_{d,hz} F_{c-hz} + I\rho_g F_{c-g}$$

As just said, I_T still can't be calculated, however many models have been developed and they are all about how the diffuse term are determined. The simplest way is to assume that the beam radiation predominates and that the diffuse concentrated in the Sun's area. Obviously by following this way I_T is overestimated and the procedure is not recommended, better models are shown in the following section.

2.1.3.1 – Isotropic Sky

The isotropic diffuse model was developed by Liu and Jordan (1963), according to this the radiation hitting the collector's surface can be split in three parts: beam, isotropic diffuse, and diffuse radiation reflected from the ground (still being part of the diffuse component). The third and fourth terms of the previous equation are null (since the diffuse comes entirely from an isotropic sky).

Let's consider a surface tilted with angle β, the view factor to the sky is $F_{c-s} = (1 + \cos(\beta))/2$, the view factor to the ground is $F_{c-g} = (1 - \cos(\beta))/2$, thus the previous equation becomes:

$$I_T = I_b R_b + I_d \left(\frac{1 + \cos(\beta)}{2}\right) + I\rho_g \left(\frac{1 - \cos(\beta)}{2}\right)$$

This is not hard to understand, easy to implement and tends to underestimate I_T which is a good thing. Anyway, better models are available in literature.

2.1.3.2 – Anisotropic Sky

Different better models have been developed during the years. Hay and Davies (1980) model improved the isotropic model by splitting the diffuse radiation in two component: the circumsolar and the isotropic. The circumsolar radiation is the energy coming from the solar aureole, it can be measured with the Circumsolar Ratio CSR which is a parameter describing the weather condition, it is defined as the circumsolar irradiance divided by the total irradiance (circumsolar plus solar disc irradiance, which can be measured with a pyrheliometer):

$$CSR = \frac{I_{cs}}{I_{cs} + I_s}$$

Anyway, the model's equation is:

$$I_T = (I_b + I_d A_i) R_b + I_d (1 - A_i) \left(\frac{1 + \cos(\beta)}{2}\right) + I\rho_g \left(\frac{1 - \cos(\beta)}{2}\right)$$

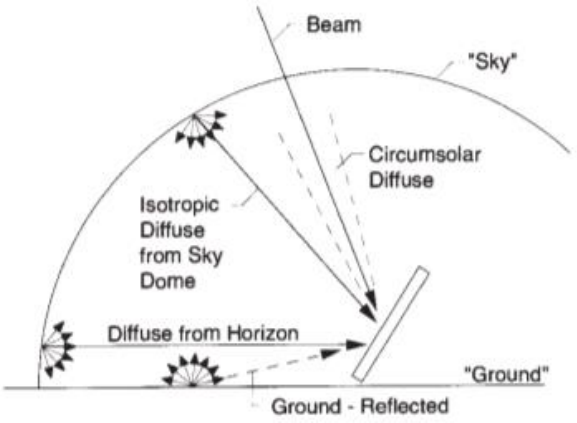

Figure 10 - Beam, diffuse, and ground-reflected radiation on a tilted surface. [J. A. Duffie et al.]

A_i is the anisotropic index, which identifies the forward scattered portion of the horizontal diffuse radiation:

$$Ai = \frac{I_{bn}}{I_{on}} = \frac{I_b}{I_o}$$

Being I_o the extraterrestrial radiation in that moment.

This leads to a slightly higher value of I_T with respect to the isotropic model. However, this still doesn't take into account the radiation diffuse from the horizon.

Temps and Coulson (1977) accounted for horizon radiation by multiplying the isotropic diffuse term by a factor of *1 + sin³(β/2)* to the isotropic diffuse. Klucher (1979) in turn modified this factor by multiplying a coefficient f to account for cloudiness. The final formula for the radiation on a tilted surface becomes:

$$I_T = (I_b + I_d A_i)R_b + I_d(1 - A_i)\left(\frac{1 + \cos(\beta)}{2}\right)\left[1 + f sin^3\left(\frac{\beta}{2}\right)\right] + I\rho_g\left(\frac{1 - \cos(\beta)}{2}\right)$$

And the modulating factor is defined as:

$$f = \sqrt{\frac{I_b}{I}}$$

2.1.4 – Direction of beam radiation

By considering what has been said so far, it's easy to understand the importance of the knowledge of the Sun position in the sky in every moment of the day and every day of the year, to do so several angles and coefficients are now defined:

- Solar Time: time based on the appearent movement of the Sun in the sky, having as noon the moment when the Sun passes through the observer meridian.

This time is used in almost all the angle relationships and doesn't coincide with the time everyone can read on common clocks. It is necessary to convert the Standard Time in Solar Time by applying two corrections: at first, there is a constant difference between the meridian's longitude of the observer's location and the Standard Longitude (on which the Standard Time is based), the Sun takes 4 minutes to cross 1° longitude; then we must consider the variation of the Earth rotation, which affects the time when the Sun crosses the meridian's longitude. This can be done by means of the "*Time Equation*". The difference in minutes between Solar and Standard Time is:

$$Solar\ Time - Standard\ Time = 4(L_{st} - L_{loc}) + E$$

Where L_{st} is the Standard Longitude for the local time zone, L_{loc} is the location's longitude. Both are in degree west: $0° < L < 360°$.

$$E = 229.2(0.000075 + 0.001868\ cos(B) - 0.032077\ sin(B) - 0.014615\ cos(2B) - 0.04089\ sin(2B))$$

B is given by the following equation:

$$B = (n-1)\frac{360}{365}$$

Being *n* the day of the year, according to the following table:

Month	*n* for *i*th Day of Month	For Average Day of Month		
		Date	*n*	δ
January	i	17	17	−20.9
February	$31 + i$	16	47	−13.0
March	$59 + i$	16	75	−2.4
April	$90 + i$	15	105	9.4
May	$120 + i$	15	135	18.8
June	$151 + i$	11	162	23.1
July	$181 + i$	17	198	21.2
August	$212 + i$	16	228	13.5
September	$243 + i$	15	258	2.2
October	$273 + i$	15	288	−9.6
November	$304 + i$	14	318	−18.9
December	$334 + i$	10	344	−23.0

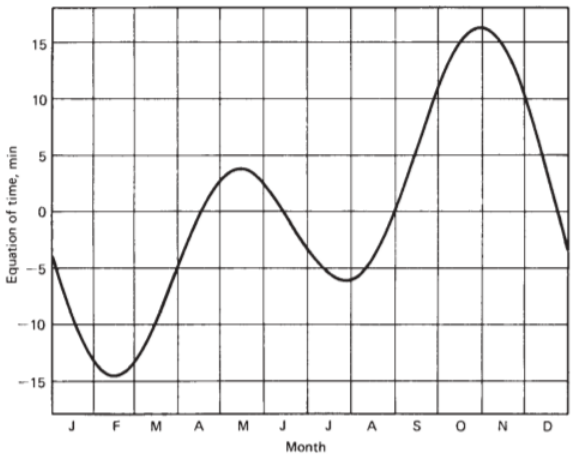

Figure 11 - The equation of time E in minutes as a function of time of year. [J. A. Duffie et al.]

Sun's position angle and some sign rules are here defined:

- $Latitude\ \varphi$: angular position at north or south of the equator (positive if northern emisphere) $(-90° \leq \varphi \leq 90°)$;
- $Declination\ \delta$: angular position of the Sun at noon with respect to the equator's plane $(-23{,}45° \leq \delta \leq 23{,}45°)$;

This can be calculated by means of Spencer's equation:

$$\delta = (\frac{180}{\pi})(0{,}006918 - 0{,}399912\cos(B) + 0{,}070257\sin(B) - 0{,}006758\cos(2B) + 0{,}000907\ sin\ (2B) - 0{,}002697\cos(3B) + 0{,}00148\sin(3B))$$

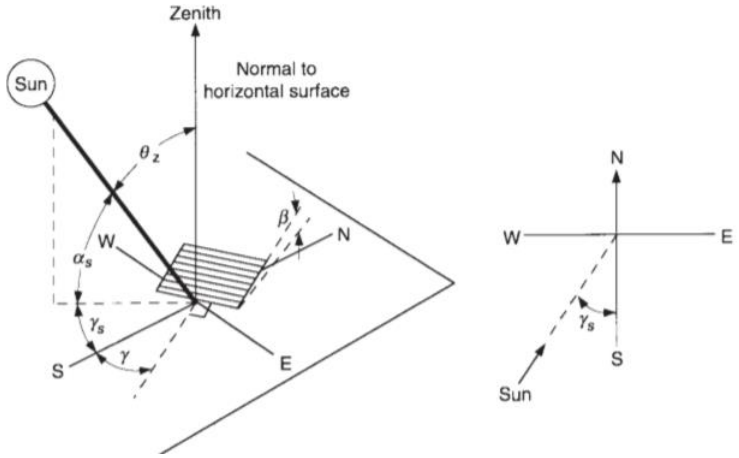

Figure 12 - (Left) Zenith angle, slope, surface azimuth angle, and solar azimuth angle for a tilted surface. (Right) Plan view showing solar azimuth angle. [J. A. Duffie et al.]

- $Slope\ \beta$: angle between the normal to the collector's surface and the horizontal direction $(0° \leq \beta \leq 180°)$;
- $Surface\ azimuth\ angle\ \gamma$: angle between the ground projection of the normal to the surface and the south direction (if collector points toward west, then $\gamma = 90°$, east $\gamma = -90°$);
- $Hour\ angle\ \omega$: angle between the local meridian and the Sun due to the rotation of the Earth (morning negative, afternoon positive);
- $Angle\ of\ incidence\ \theta$: angle between the Sun's connecting line with the observer and the normal to the collector;
- $Zenith\ angle\ \theta_z$: angle between the vertical direction and the Sun's connecting line with the observer;
- $Solar\ altitude\ angle\ \alpha_s$: angle between the horizontal direction and the Sun's connecting line with the observer (basically $\alpha_s = 90 - \theta_z$);
- $Solar\ azimuth\ angle\ \gamma_s$: angle between the ground projection of the Sun's connecting line with the observer and the South direction (west positive, east negative).

Useful relationships between these angles are here provided:

$$\omega = 15(Solar\ Time - 12)$$

$$cos(\theta_z) = cos\ (\varphi)\ cos\ (\delta)\ cos(\omega) + sin(\varphi)\ sin(\delta)$$

$$\gamma_S = sign(\omega)\left|\cos^{-1}\left(\frac{\cos(\theta_z)\sin(\varphi) - \sin(\delta)}{\sin(\theta_z)\cos(\varphi)}\right)\right|$$

2.1.5 – Angles of tracking surfaces

Angles β, γ depend on the tracking strategy chosen, for big parabolic trough collectors only a single axis movement is allowed, two are the possibilities:

- North-South rotation axis (collector faces eastward at dawn, westward at sunset):

$$\gamma = \begin{cases} +90° & if\ \gamma_S > 0 \\ -90° & if\ \gamma_S \leq 0 \end{cases}$$

$$\tan(\beta) = \tan(\theta_z)\,|\cos(\gamma - \gamma_s)|$$

- East-West rotation axis (movements depend on the location):

$$\gamma = \begin{cases} 0° & if\ |\gamma_S| > 90° \\ 180° & if\ |\gamma_S| \leq 90° \end{cases}$$

$$\tan(\beta) = \tan(\theta_z)\,|\cos(\gamma_s)|$$

As soon as angles β and γ are calculated, the $Angle\ of\ incidence\ \theta$ can be calculated as follows:

$$\cos(\theta) = \cos(\theta_z)\cos(\beta) + \sin(\theta_z)\sin(\beta)\cos(\gamma - \gamma_s)$$

2.1.6 – Shading phenomenon

The shading phenomena is something to cope with every time a solar technology is involved. It leads to the energy losses and depends on the size of the collectors used as well as the radiation available in that moment. Generally, there are three kind of shading that could occur:

1. Caused by nearby trees, building or whatever relatively big and around the receiver, sometimes complex model could needed when the geometry of the obstruction is irregular.

2. It happens when multiple rows of collectors are present, all the rows but the first one are shaded by the collectors in the adjacent row. Practically speaking, every collector casts a shadow on the other one in the back row;
3. The third situation is the shading of a window caused by an overhang or a wingwall.

In the current project work we will care mostly about the second case.

The model that will be presented in this paragraph has been developed by [V.M. Sharma et al.] for Parabolic Trough Collectors (PTC) solar fields with multiple rows with single axis tracking, of course every row having the same number of collectors connected in series.

Important parameters required for the calculation of the *Shading Coefficient* η_s are the total length of the row(s) *L*, the width of the collectors chosen *w* and the spacing between each row (so called pitch) *p*. The fundamental concept around this model is the fact that every row is separated with the same *p*, moreover the shadow cast from each of them is rectangular in shape, being every row parallel, moving identically and with rectangular aperture areas.

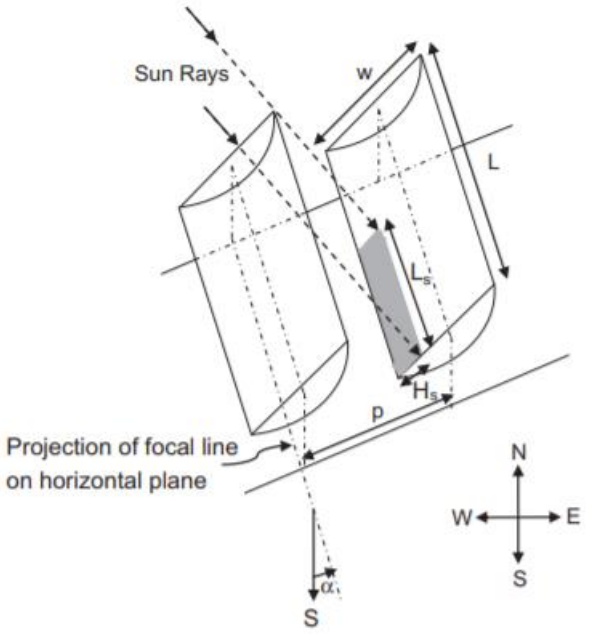

Figure 13 - Shading of one row due to the next one. [V.M. Sharma et al.]

Basically, sun rays are stopped by a collector before hitting the one next to it and this depends heavily on the tracking strategy chosen, which means on several angles defined previously. The calculation is made of two main steps:

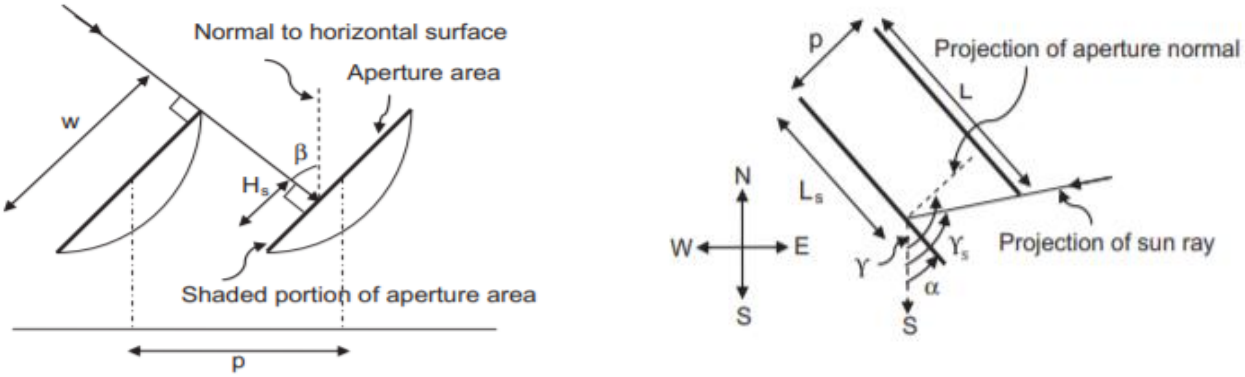

Figure 14 - (Left) Shaded height H_s. (Right) Shaded length L_s. [V.M. Sharma et al.]

1. Calculation of the rectangle height H_s of the shadow cast:

$$H_s = [w - p\cos(\beta)]^+;$$

2. Calculation of the rectangle length L_s of the shadow cast:

$$L_s = [L - |p\tan(\gamma - \gamma_s)\,|]^+;$$

Where "+" means that only positive values has to be considered.

Thus, the shaded area will be;

$$A_s = \begin{cases} H_s L_s & if\ \theta_z \leq 90° \\ 0 & otherwise \end{cases}$$

By defining as A_{coll} the total reflective area of one row and keeping in mind that the first row is never shaded, the formula needed for the calculation of η_s is:

$$\eta_{shad} = 1 - \left(\frac{N_{rows} - 1}{N_{rows}}\right)\left(\frac{H_s}{W}\right)\left(\frac{L_s}{L}\right) = 1 - \left(\frac{N_{rows} - 1}{N_{rows}}\right)\left(\frac{A_s}{A_{coll}}\right)$$

Eventually, if needed, it is also possible to calculate another factor, called *Shading Factor SF* , which is pretty useful to estimate the shading phenomena effect over a given period of time so defined:

$$SF = \frac{\int_{t_1}^{t_2} A_s\, dt}{\int_{t_1}^{t_2} A_{coll}\, dt} \approx \frac{\sum_{i=1}^{N}(A_s)_i(\Delta t)_i}{\sum_{i=1}^{N}(A_{coll})_i(\Delta t)_i}$$

where N is the number of intervals in which the time period $[t_1,t_2]$ is divided and Δt is the interval where the parameters are assumed as constant.

2.2 – CSP Technology

For some application is necessary to deliver energy at higher temperatures. The basic principle is: reducing the area involved in the heat losses by putting an optical device between the Sun and the receiver, this is the main difference between this technology and the flat plate collector one.

In order to avoid confusion, the word “collector” will be used to the total system, including collector and receiver; the “receiver” is that part of the collector where the energy is absorbed and includes the absorber and its associated covers and insulations. The concentrator is the optical system, which deviates the sun rays on the receiver. The Aperture Area is the effective surface through which the solar radiation enters the system.

There are multiple kind of configuration that can be chosen:

- Concentrators can be either of the reflector type or a refractor, can be shaped as a cylinder or a revolution surface;
- Receivers can be shaped either convex, concave or flat and then covered by further covers;

One of the most important figures in this topic is the *Concentration Ratio*, there are actually different definition that can be used but the most usual is the ratio of the areas of the receiver and that of the collector (Aperture Area):

$$C = \frac{A_c}{A_r}$$

This ratio has an upper limit which depends on the geometry of the system, the higher we want the temperature of the energy delivered, the higher must this ratio be.

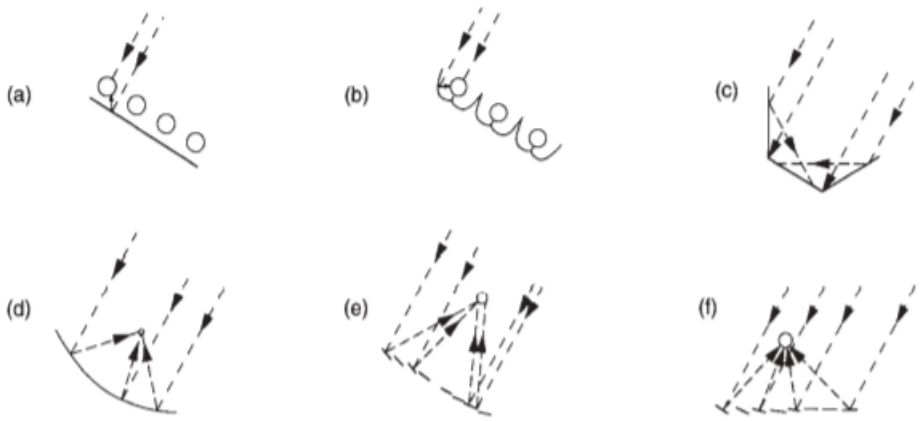

Figure 15 - Possible concentrating collector configurations: (a) tubular absorbers with diffuse back reflector; (b) tubular absorbers with specular cusp reflectors; (c) plane receiver with plane reflectors; (d) parabolic concentrator; (e) Fresnel reflector; (f) array of heliostats with central receiver. [J. A. Duffie et al.]

Generally speaking, these devices can be classified either as linear imaging or non-imaging collectors. Non-imaging collectors have usually low concentration ratios, linear collectors have intermediate concentration ratios. There are also three-dimensional concentrators with much higher value of the concentration ratio (they can even work at a ratio of 10^5), in fact some of these concentrators are named for this reason “*Solar furnaces*”. Except for very low concentration ratios, these systems require a tracking movement that allow them to redirect the sun onto the receiver.

This is because if the area of the receiver is much smaller than that of the concentrator only the beam radiation will be effective, this is one of the disadvantages this kind of system has with respect to the flat-plate technology and let's not forget also about the new requirements for the maintenance work, especially to retain the quality of the optical system. The Sun tracking system can provide a very frequent (nearly continuous) adjustment in order to make the collector compensate the movement of the Sun. Tracking system can be either manual or mechanized.

Manual tracking depends mostly on the correction skills of the worker, it can be a good option if the concentration ratio is not very high and when the labor price is not prohibitive.

Mechanized system can be either sun-seeking systems, which use detectors to determine misalignment, or programmed system which make the collectors move in a predetermined manner and may need some maintenance work to check the correct functioning.

2.2.1 – Concentrator optics

Let's consider a solar concentrator with perfect optics that concentrates radiation from a collector to a receiver with reflection and emission losses. Let's calculate the efficiency of such a device.

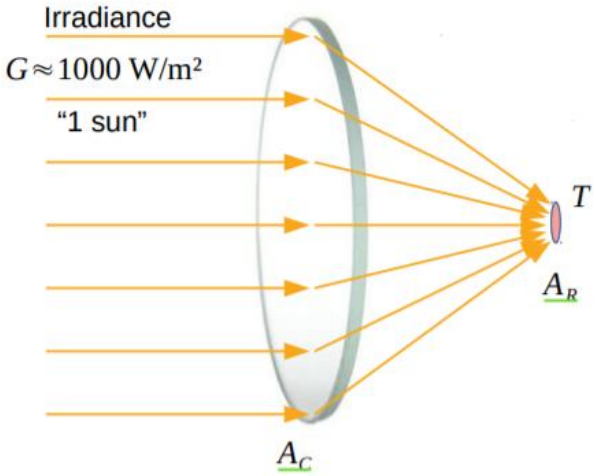

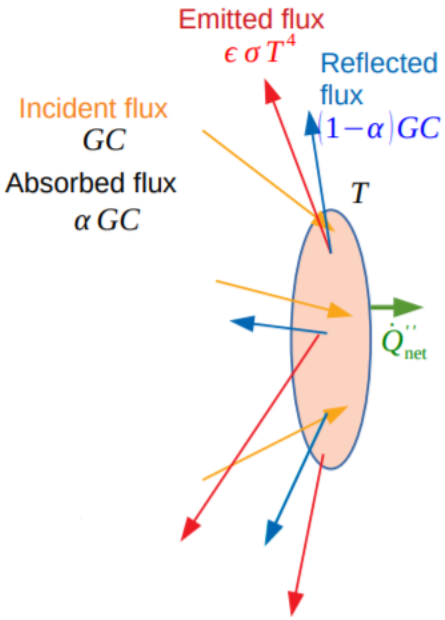

Receiver thermal energy balance:

$$\dot{Q}_{net} = \alpha GC - \epsilon\sigma T^4$$

Then, the thermal efficiency of the receiver it's going to be:

$$\eta_{th} = \frac{(\dot{Q}_{net} A_c)}{GCA_c} = \alpha - \epsilon \frac{\sigma T^4}{GC}$$

Let's assume the collector as an ideal black body cavity with $\alpha = \epsilon = 1$. We would have:

$$\eta_{th} = 1 - \frac{\sigma T^4}{GC}$$

Let's suppose to use the heat extracted by the receiver to power a Carnot engine with cold reservoir at T_0, the efficiency of the Carnot engine is:

$$\eta_c = 1 - \frac{T_0}{T}$$

Overall:

$$\eta = \eta_{th}\eta_c = \left(1 - \frac{T_0}{T}\right)\left(1 - \frac{\sigma T^4}{GC}\right)$$

Solving for $\eta = 0$ we obtain two temperatures:

- $T = T_0$;
- "$Stagnation\ temperature$":

$$1 - \frac{\sigma T^4}{GC} = 0 \quad \leftrightarrow \quad T_{st} = \sqrt[4]{\frac{GC}{\sigma}}$$

We look also for the maximum efficiency, for a given concentration ratio, it will lead to the optimal temperature:

$$\frac{d\eta}{dT} = 0 = \left(1 - \frac{T_0}{T}\right)\frac{\sigma}{GC} 4T^3 + (1 - \frac{\sigma T^4}{GC})\frac{-T_0}{T^2}$$

$$\leftrightarrow \quad \frac{\sigma T^4}{GC}(4T - 3T_0) - T_0 = 0$$

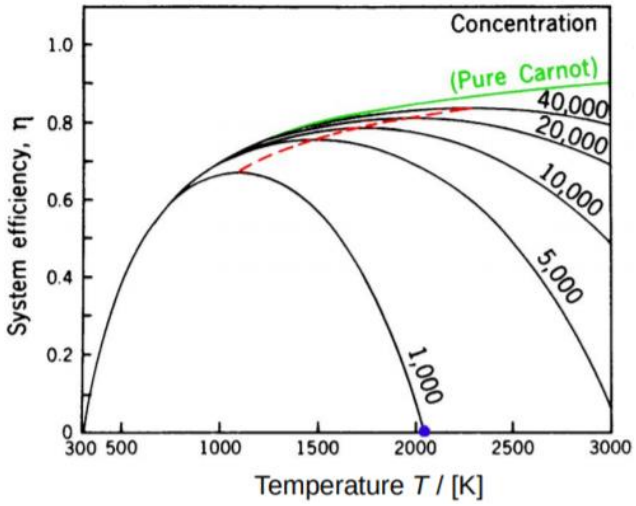

Figure 16 - Variation of ideal system efficiency with temperature at various solar concentration ratios. The dashed line goes through the efficiency maximum at each concentration. [E. A. Flatcher et al.]

Which means that efficient systems require high concentration and high temperature.

It's been mentioned before the concentration ratio has an upper limit, the incident irradiance arriving at the Earth is :

$$G = E_0\left(\frac{r^2}{R^2}\right) = E_0\left(\frac{\left(Rsin(\theta)\right)^2}{R^2}\right) = E_0\sin^2(\theta)$$

Being $E_0 = \sigma T_s^4$ and T_s the temperature of the Sun.

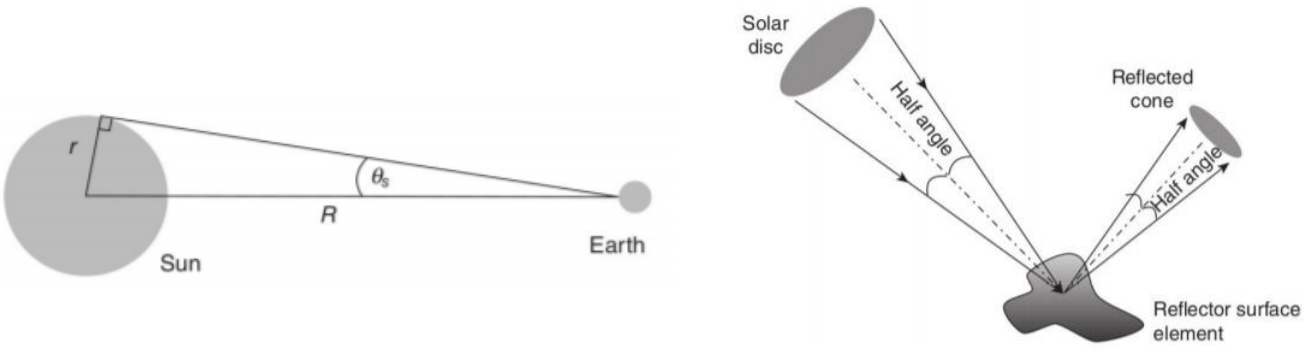

Figure 17 - (Left) Radiation flux from a spherically symmetric black body falls off as $1/R^2$. (Right) Points on a reflector surface reflect direct solar irradiation in a cone of rays. [K. Lovegrove et al.]

Let's consider now this radiation to be incident to a device with a surface A_c and, in turn, concentrated on a receiver with smaller area A_R with ideal black-body features at temperature T_R:

$$\sigma\, T_S^4\ A_c\, sin^2\, \theta_s = \sigma\, T_R^4\, A_R$$

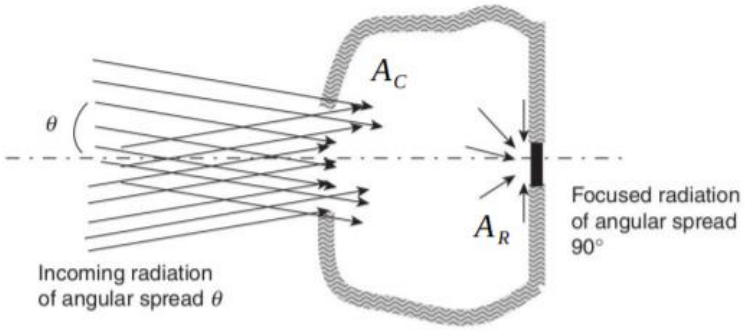

Figure 18 - A concentrator that takes radiation with angular spread half-angle θ and concentrates it to a receiver with a final angular spread of half-angle 90°. [K. Lovegrove et al.]

We can immediately observe that, at equilibrium, the receiver's temperature cannot be higher than the Sun temperature because of the Second Law of Thermodynamics (Clausius statement):

$$T_R \leq T_S$$

This results in an upper bound of the Concentration Ratio:

$$C_{g,pt} = \frac{A_c}{A_R} \leq \frac{1}{\sin^2 \theta_S}$$

This result is valid for point concentrators. We can extend the idea by considering a third surface A_{out}:

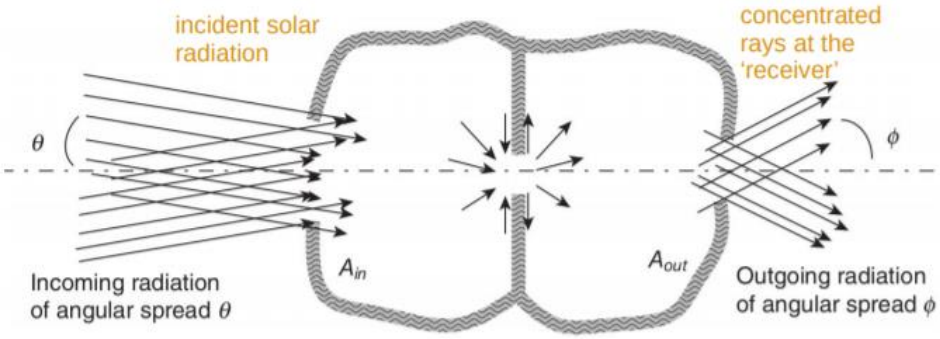

Figure 19 - An arbitrary concentrator accepting radiation with a half-angle θ over area A_{in} and sending it out over area A_{out} with half-angle ϕ. [K. Lovegrove et al.]

$$\sigma T_R^4 A_R = \sigma T_S^4 A_{out} \sin^2(\varphi)$$

The concentration limit will be a function of the acceptance angle of the receiver. The next formula is known as "*Conservation of étendue*":

$$A_{in} \sin^2(\theta_s) = A_{out} \sin^2(\varphi)$$

As before we obtain:

$$C_{g,pt} = \frac{A_{in}}{A_{out}} \leq \frac{\sin^2(\varphi)}{\sin^2(\theta)}$$

But if the concentration takes place only in angular direction (not two as before) we are talking about a linear concentrator:

$$C_{g,lin} = \frac{A_C}{A_R} \leq \frac{\sin(\varphi)}{\sin(\theta)} < \frac{1}{\sin(\theta)}$$

We evaluated the concentration ratio with the solar half-angle of 0.266° and receiver acceptance angle of 90°. We obtain:

Point concentrator	Linear concentrator
46250	215

2.2.2 – Receivers

A receiver is a component of a concentrating solar thermal system that absorb concentrated sunlight and transfers the energy to a heat transfer medium.

There are different types (class) of receivers that can be used based mainly on the heat transfer mechanism: tubular, volumetric…etc. Also very important is the heat transfer medium to be used, here some examples:

- Two phase/multiphase: water (phase changing), carbon dioxide (supercritical), sodium (saturated);
- Gas: Air, Hydrogen, Helium, carbon dioxide;
- Liquids (unpressurised): Heat transfer oils, molten salts, molten metals, molten carbonates, ionic liquids;
- Solids (particles): Sand, Silicon carbide.

As mentioned before, the concentration ratio can be written as:

$$C_{geom} = \frac{A_c}{A_r}$$

But this is actually the "*geometric*" definition of the ratio which is very easy to calculate and doesn't take into account imperfections like mirror reflectivity and other optical effects. A better idea of this is given by the *"Optical concentration ratio"*, defined as the radiation intensity absorbed by the receiver divided by the un-concentrated radiation from the Sun:

$$C_{opt} = \frac{I}{I_{solar}}$$

This can be evaluated everywhere in the system, so a more useful measure is the average one:

$$\bar{C} = \frac{\int I \, dA_{apert}}{A_{apert} \, I_{solar}}$$

Designing a high efficiency collector forces us to pay attention to a wide range of optical and thermal losses which have to be minimized. Thermal losses are generally proportional to the scale of the receiver (they all depends on the area of it).

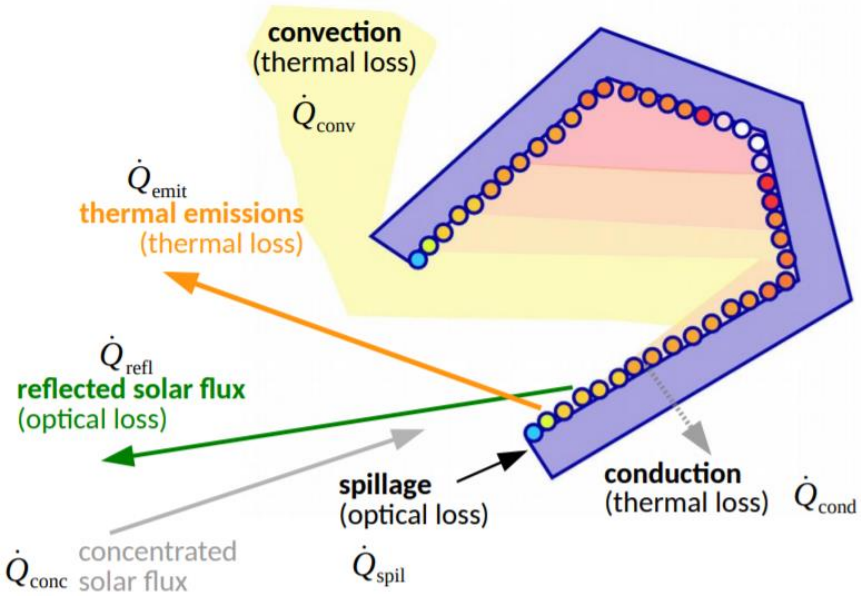

Energy balance : $\dot{Q}_{\text{useful}} = \dot{Q}_{\text{conc}} - \dot{Q}_{\text{spil}} - \dot{Q}_{\text{refl}} - \dot{Q}_{\text{emit}} - \dot{Q}_{\text{conv}} - \dot{Q}_{\text{cond}}$

The optical analysis is useful to quantify:

- $\dot{Q}_{\text{conc}}$: Concentrated radiation pointing at the receiver;
- $\dot{Q}_{\text{spil}}$: Radiation that misses the aperture area, it will be always present, even at small degrees;
- $\dot{Q}_{\text{refl}}$: Radiation reflected out of the receiver;
- $\dot{Q}_{\text{abs}}$: Radiation absorbed by the receiver;

Generally we have:

$$\dot{Q}_{\text{conc}} = \dot{Q}_{\text{abs}} + \dot{Q}_{\text{spil}} + \dot{Q}_{\text{refl}}$$

Absorbed radiation formula is as follows:

$$\dot{Q}_{\text{abs}} = \alpha_{eff} \bar{C} G A_{apert}$$

Being *G* the Direct Normal Irradiance (DNI) and α_{eff} the effective absorptivity which is a property of the material of which the receiver is made, for cavities (or in general, non-convex surfaces) it should

take into account the multiple reflections and absorption. Further analysis can be required to investigate on the dependence between directional and absorptivity effects.

$\dot{Q}_{\text{emit}}$ are the thermal emission losses, every surface radiates energy by thermal emission. Emissivity ε can have sometimes a directional and spectral variation but grey and diffuse surfaces assumptions are considered most of times reasonable. Anyway receivers can be very often cavities where emitted radiation bounces and is re-reflected or absorbed and thus an "effective emissivity" needs to be defined, let's think about an isothermal receiver with surface area A_{cav} and aperture area A_{apert}:

$$\varepsilon_{eff} = \frac{\varepsilon}{\frac{A_{apert}}{A_{cav}}\varepsilon\left(1 - \frac{A_{apert}}{A_{cav}}\right)}$$

So we can calculate the thermal emission losses:

$$\dot{Q}_{\text{emit}} = \sigma\varepsilon_{eff}A_{apert}(\bar{T}_{ext}^4 - T_{amb}^4)$$

Problems arises when the receiver surface's temperature is not uniform, in that case the solving of a radiation balance problem could be needed (for example by means of the "radiosity method").

As shown so far, absorbed radiation and emission losses depends on the intrinsic properties of the receiver's material. Thus we can define a selective surface efficiency:

$$\eta_{sel} = \frac{\alpha_{sol}\bar{C}G - \varepsilon_{th}\sigma T^4}{\bar{C}G}$$

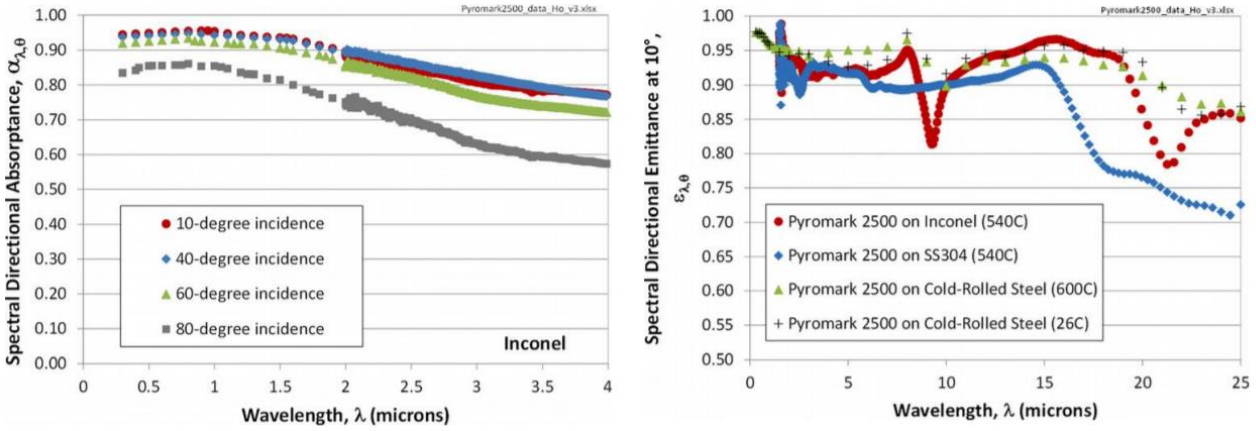

Figure 20 - Pyromark 2500 paint (Left) Absorption wavelengths. (Right) Emission wavelengths.

To summarize, we can aim at minimizing radiative losses, there are mainly two strategies that can be applied:

1. Using cavity-shaped receivers to decrease reflection and emission losses, we want to achieve: lower temperature on the external surface, higher temperature on the internal surface
2. Using selective surfaces, i.e. high solar weighted absorptivity (solar spectral range) and at the same time low thermal weighted emissivity (blackbody spectral range).

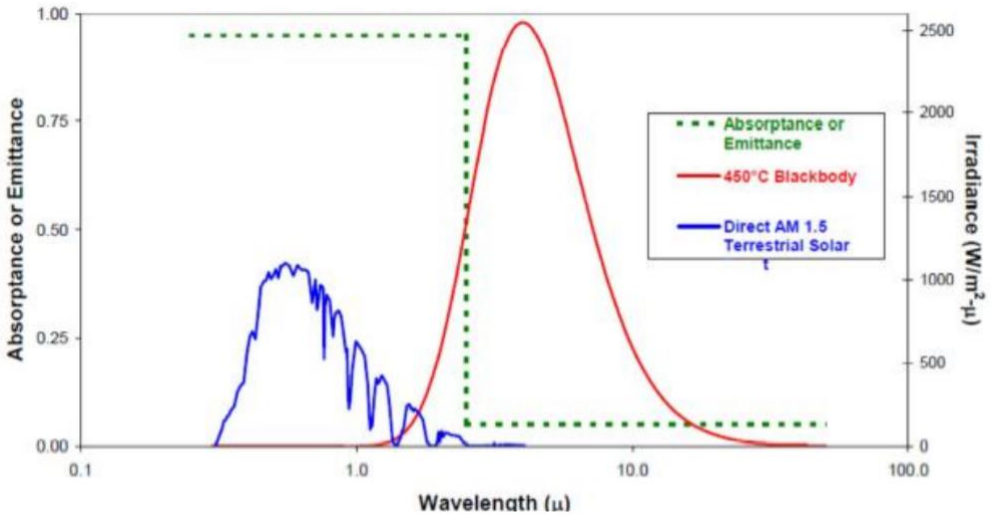

Figure 21 - Comparison between the spectrum of the Sun, the 450°C blackbody spectrum and how a selective surface works.

An ideal selective surface has a very good absorption in the spectral range between around 0.3 and 2.5 μm and almost no emission of blackbody radiation. At higher temperatures, it become harder to apply a selective surface because of spectral overlapping.

The evaluation of convective losses is based mainly on the calculation of the "convective heat transfer coefficient" h_{conv} , which joins the effects of both natural and forced convection on the external surface A_{ext}. The general convective heat exchange law is:

$$\bar{Q}_{conv} = h_{conv} A_{ext} (\bar{T}_{ext} - T_{amb})$$

h_{conv} can be calculated using the Nusselt number definition:

$$h_{conv} = \frac{Nu\, k_{air}}{L}$$

Being k_{air} the thermal conduction of air and *L* a representative dimension which depends on the geometry of the system (e.g. if the system is a pipe, then L will be the diameter).

- Natural convection: caused by the buoyancy effects of air heated by the receiver its self. Usually in this case the Nusselt number depends on two more dimensionless numbers:

$$Nu = f(Ra, Pr)$$

Ra is the Rayleigh number and is an indicator which gives a clue of how strong buoyancy forces are compared to viscosity forces. *Pr* is the Prandtl number, ratio of the momentum diffusivity to thermal diffusivity:

$$Ra = \frac{g\beta_0 \Delta T L^3}{\nu \alpha_0} \qquad Pr = \frac{\mu c_p}{k} = \frac{\nu}{\alpha}$$

g is the gravity acceleration, β_0 is the thermal expansion coefficient at temperature T_0 (equals to $1/T_0$, for ideal gases), ν is the kinematic viscosity, ΔT is the temperature difference between the surface in question and the quiescent air, α_0 is the thermal diffusivity at temperature T_0, *L* as before is a representative dimension of the system, μ is the dynamic viscosity of the fluid (air), c_p is the isobaric specific heat of air.

- Forced convection: caused by wind on the receiver. Nusselt number now depends on:

$$Nu = f(Re, Pr)$$

Being *Re* the Reynold number, ratio of the inertial forces and viscosity forces in the phenomena:

$$Re = \frac{\rho u L}{\mu}$$

Where *u* is the speed of the fluid, *L* is again a certain representative length.

Usually happens that *Nu* decreases slightly with increasing receiver's temperature but h_{conv} slightly increases because k_{air} increases with the temperature as well.

Some strategy to reduce convective heat losses consists in:

- Enclosing the receiver in a glass cover (maybe a window);
- Using an active air curtain to retain (as for large shops entrance doors) the hot currents (for cavities).

Receiver windows find their only weakness in increasing the reflection losses (sun rays bounces away from the glass) but, on the other hand, they can be useful to reduce thermal emissions, for example using glass with low transmissivity in the infrared spectral range (greenhouse effect).

Now let's talk about the useful heat, the one absorbed by the working fluid. Let's see the case of a tubular receiver, it must pass through different layers:

- Surface coating;
- Tube material (tube wall);
- Internal convection boundary layer inside the pipe

Each of these layers has a thermal resistance (*R* value) which implies a temperature difference between the external surface and the fluid, the equivalent R value is based on the external absorbing surface area:

$$R_{eq} = \sum_i R_i$$

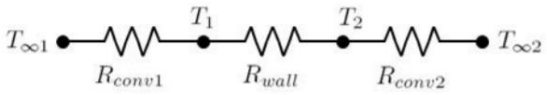

Thus the useful heat transferred to the fluid will be:

$$\dot{Q}_{use} = A_{ext}\frac{(T_{ext} - \bar{T}_f)}{R}$$

For this application, we are looking for the smaller possible thermal resistance.

Let's expand the steady state energy balance written before:

$$A_{ext}\frac{(T_{ext} - \bar{T}_f)}{R_{wall}} = \alpha_{eff}\bar{C}GA_{apert} - \sigma\varepsilon_{eff}A_{apert}(\bar{T}_{ext}^4 - T_{amb}^4) - h_{conv}A_{ext}(\bar{T}_{ext} - T_{amb}) - A_{ext}\frac{(T_{ext} - T_{amb})}{R_{cond}}$$

This equation may be solved numerically for the external surface temperature T_{ext}. After all the heat fluxes are known we can calculate the receiver energy efficiency:

$$\eta_I = \frac{\dot{Q}_{use}}{\dot{Q}_{conc}}$$

2.3 – Parabolic Troughs

Parabolic troughs collectors (PTCs) are the most mature technology within all the CSPs. These collectors are composed of a parabolic-shaped mirror which reflects the radiation on the focal plane, where the absorber tube is located. PTCs produces heat at temperatures between 50°C and 400°C, such temperatures are high enough for usuals industrial processes and applications (they usually have an exercise temperature lower than 300°C).

PTCs have relatively light structures, they are supported from the ground by simple pedestals at both ends and are composed of a sheet of reflective material, usually silvered acrylic, bent into a parabolic shape. Several modules can be put in a line in order to obtain a much longer trough. The receiver is generally a black metal pipe protected by a glass cover which lowers the convection heat losses. The receiver is covered with a selective coating with high solar absorbance and low thermal emissivity in the black body spectral range, the glass tube is also covered with an anti-reflective coating which enhances transmissivity.

The HTF (Heat Thermal Fluid) flows inside the receiver transporting the energy to the plant downstream (it is usually an electricity generation system, this can usually be a thermal oil or water but thermal oil is preferred because of its higher boiling temperature and low volatility. Anyway recent innovation promotes the use of molten salts (ionic liquids) as they are more heat-resilient than oil and corrode the heat pipe less, however they are quite expensive and so is the maintenance of such a solar field, therefore a pretty accurate cost analysis should be done in order to choose the best HTF. Because of PTC's structure, they can track the Sun only by moving on a single-axis that

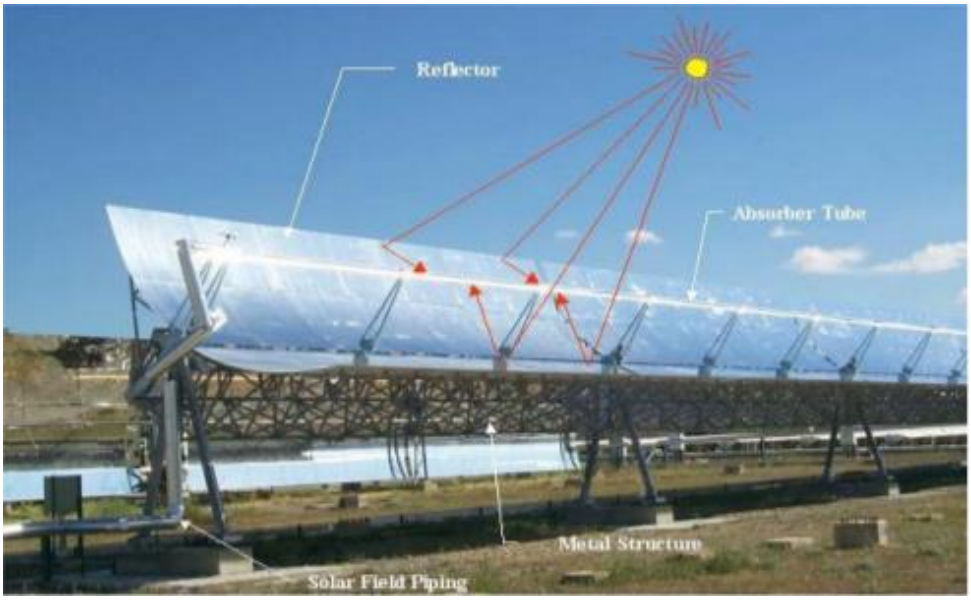

Figure 22 – Eurotrough parabolic troughs collector. [M.A. Geyer et al. (2003)]

keeps incident light focused on the receiver throughout the day, two are the possibilities: North-South and East-West axis alignment. Generally the best one is the latter because it allows to collect more energy throughout the year, the former allows to collect more energy during the summer, that is the period when the Sun reaches the top for more (Zenith); anyway, it heavily depends on the location and early predictions can easily be wrong.

However, these collectors suffer from some practical problem which must be properly considered in order to achieve a consistent and efficient design. These problems are mostly about the optics of the collector which depend on the tracking strategy, the geometry and the materials.

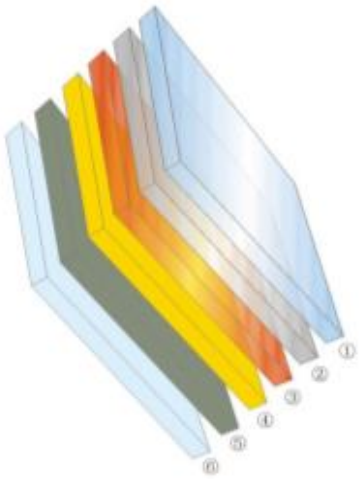

Figure 23 - Flat mirror layers (From SUNDHI brochure) 1. Glass 2. Silver 3. Copper 4. Base coating 5. Intermediate coating 6. Top coating.

2.3.1 – Geometry and optical properties

It is necessary to explain carefully the geometry and the optical properties of the collector in order to understand how the image of the beams cone (the distribution of the solar radiation at the receiver) is affected. Important thing is to know what happen for a collector perfectly aligned with the Sun and what actually changes in the image reflected in the practical experience, since perfect alignment is ideal.

The main component of a PTC is the parabolic mirror, the equation of the parabola is:

$$y^2 = 4fx$$

The "aperture width" is *a* and the "focal length" is *f*. The focal length is the distance between the vertex of the parabola and the focal point.

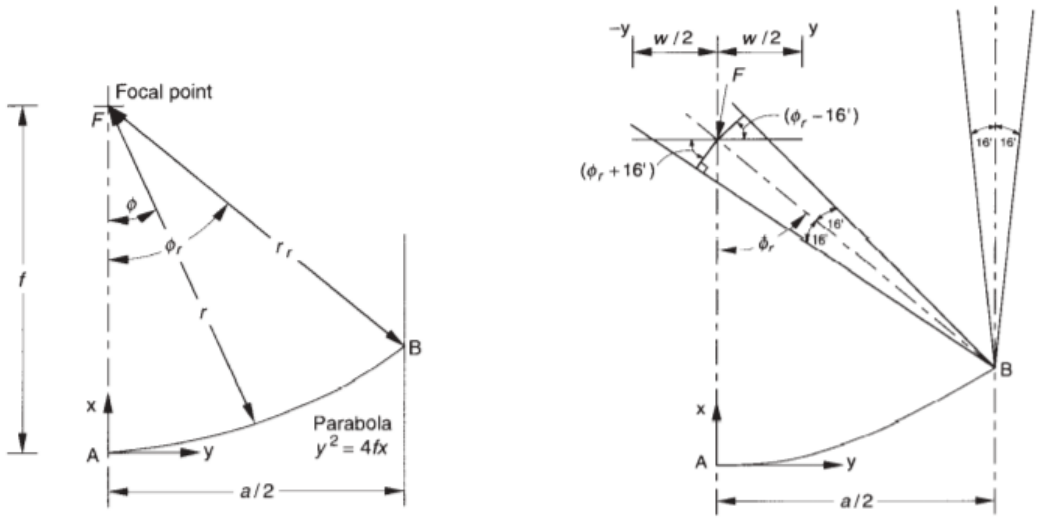

Figure 24 – (Left) Section of a linear parabolic concentrator showing major dimensions and the x, y,z coordinates. (Right) Image dimensions for a linear concentrator. [J. A. Duffie et al.]

φ_r is the "Rim Angle" and is given by:

$$\varphi_r = \tan^{-1}\left[\frac{8\left(\frac{f}{a}\right)}{16\left(\frac{f}{a}\right)^2 - 1}\right] = \sin^{-1}\left(\frac{a}{2r_r}\right)$$

It's pretty useful to plot this angle as a function of the *f/a* ratio.

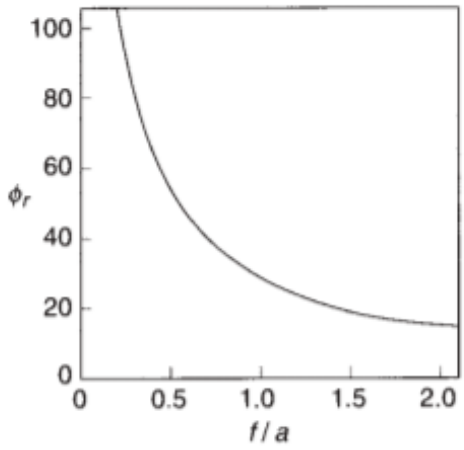

Figure 25 - Rim angle ϕr as a function of focal length – aperture ratio. [J. A. Duffie et al.]

r_r is the "maximum mirror radius" that is the distance between the focal point and the edge of the collector. We can evaluate the generic radius "r" as:

$$r = \frac{2f}{1 + \cos(\theta)}$$

A generic beam of solar radiation has a semi-amplitude of $\theta_S = 0.267°$ (or 4,653 *mrad*), so the amplitude of the solar bundle is 0.53° (or 32'). For the current purpose, let's assume a symmetrical concentrator and the beam radiation normal to the aperture.

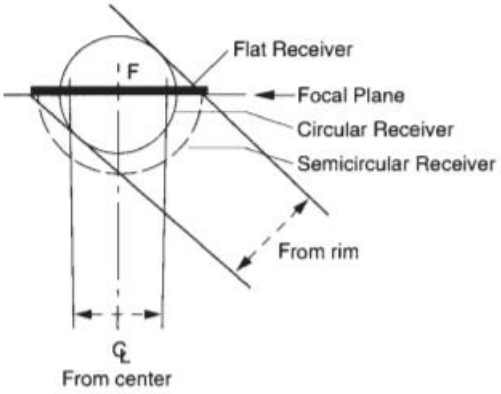

Figure 26 - Schematic of reflected radiation from center and rim of a (half) parabolic reflector, with minimum plane, circular, and semicircular receivers to intercept all reflected radiation from a full parabola. [J. A. Duffie et al.]

Two are the most widely used receiver geometries: flat and cylindrical.

The width of the image in the focal plane increases with the rim angle.

If we assume perfect shape and alignment we can the receiver diameter intercepting all the beam can be calculated:

$$D = 2r_r \sin(\theta_S) = \frac{a \sin(\theta_S)}{\sin(\varphi_r)}$$

The width "*W*" required for a flat receiver (or semi-circular) is:

$$W = \frac{2r_r \sin(\theta_S)}{\cos(\varphi_r + \theta_S)} = \frac{a \sin(\theta_S)}{\sin(\varphi_r)\cos(\varphi_r + \theta_S)}$$

Essentially, the focal length is the most determining factor for the image size; the aperture area for the energy collected. As a consequence, the image brightness as well as the energy collected will be a function of the ratio *f/a*.

The radiation incident on an element of area of a reflector can be though as a cone having an angle at the vertex of 0.53°, if we consider a perfect linear reflector, the reflected cone will have the same amplitude and the interception of this cone with the receiver determines the image size and shape for that reflector's element. The total image is going to be the sum of all the images reflected.

The energy is not distributed uniformly in the cone, several non-uniform solar disk model are proposed in the literature. These models take into account the fact that the Sun radiates mostly from the center of the disk rather than from the edge.

Let's assume a trough with cylindrical receiver with radius "*t*". *R* is the generic normal distance between the axis and the reflector, then we calculate the geometric concentration ratio:

$$C_{geom} = \frac{A_C}{A_R} = \frac{R}{\pi\, t}$$

where:

$$t = r \sin(\theta_S) = \frac{R \sin(\theta_S)}{\sin(\varphi_R)}$$

Then:

$$C_{geom} = \frac{\sin(\varphi_R)}{\pi \sin(\theta_S)}$$

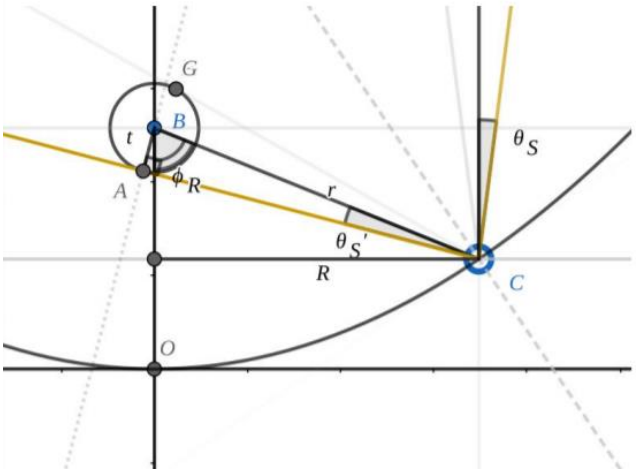

Figure 27 – Scheme of a reflected beam cone, cylindrical receiver.

For the maximum concentration ratio:

$$\frac{dC_{geom}}{d\varphi_R} = \frac{\cos(\theta_R)}{\pi \sin(\theta_S)} = 0 \qquad \text{at } \frac{\pi}{2} = 90°$$

At the end:

$$C_{geom,max} = \frac{1}{\pi \sin(\theta_S)} \approx 68.5$$

This is 1/π times the thermodynamic limit.

The Local Concentration Ratio:

$$C_l = \frac{I(y)}{I_{b,ap}}$$

Is the ratio between a collector's element radiation intensity and the one on the aperture area.

This is a function of the rim angle: as this increases, the ratio increases as well and so does the size of the image.

The $Intercept\ Factor\ \gamma$ is the fraction of the radiation that hits the receiver surface. If the receiver extends from A to B, then:

$$\gamma = \frac{\int_A^B I(w)\, dw}{\int_{-\infty}^{+\infty} I(w)\, dw}$$

So, if the objective is to reduce thermal losses from the absorber by decreasing the receiver's exchanging area, we must consider also the effect it has on γ.

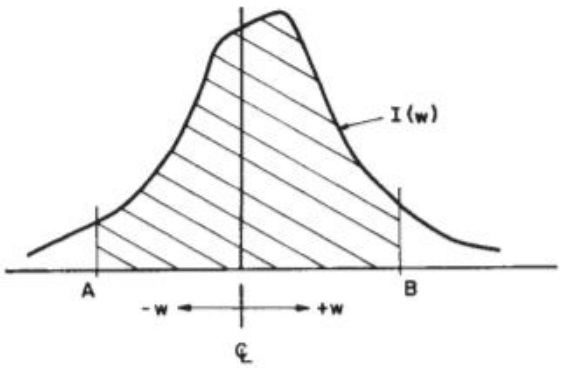

Figure 28 – An example of a flux distribution in the focal plane of a linear imaging concentrator. The receiver extends from A to B. [J. A. Duffie et al.]

It is quite interesting to calculate and plot the Intercept Factor and the Local Concentration Ratio as a function of the distance from the image center expressed as *y/f*.

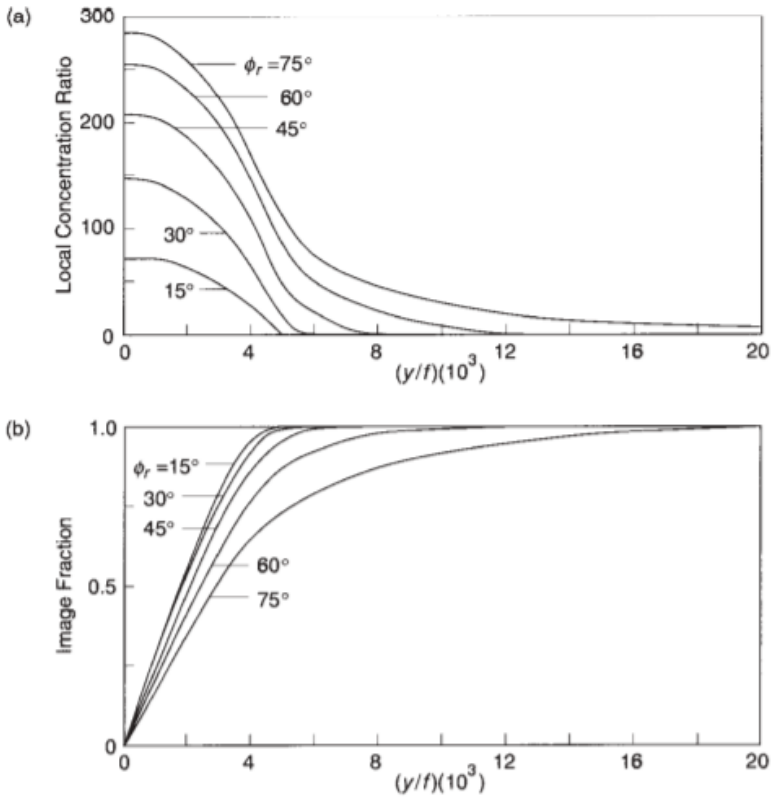

Figure 29 – (Up) Image distributions for perfect concentrators for the nonuniform solar disk. (Down) Intercept factors for images from perfect concentrators obtained by integrating areas under curves of (Up). [J. A. Duffie et al.]

To this point we are considering $\theta = 0°$ (perfect alignment), two variation can occur: pointing error in the *x-y* plane, tracking errors which leads to angular inaccuracies in the *x-z* plane.

The first variation leads to a displacement of the image from the focal point, displacement of the receiver from the focal point leads as well to significant changes in the nature of the image.

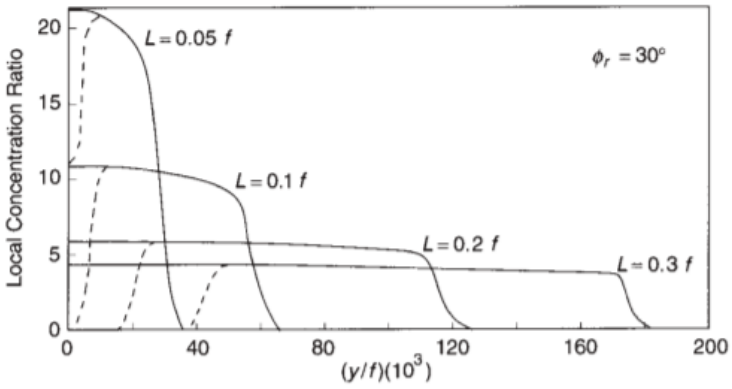

Figure 30 – Reflectance = 1. Image distributions for 30◦ rim angle reflectors for several displacements of the plane of the image from the focal plane. The dashed curve shows the effect of shading of the reflector by the absorber. [J. A. Duffie et al.]

The figure shows how the displacement *L* (distance from the axis) affects the Local Concentration Ratio, it is clear that the effect increases as the rim angle increases.

PTC can be oriented in several ways during the tracking activity, in general the beam radiation will be in the *x-z* plane but not normal to the aperture. Basically as θ increases, the half-angle subtended by the Sun increases as $1/\cos(\theta)$. It is possible to express the resulting image as follows:

$$W = \frac{2r_r \sin\left(\frac{\theta_S}{\cos(\theta)}\right)}{\cos(\varphi_r + \frac{\theta_S}{\cos(\theta)})}$$

The effect of the incident angle can be better understood by writing the ratio between the widths of the new and the original image:

$$\frac{W}{W_0} = \frac{\sin\left(\frac{\theta_S}{\cos(\theta)}\right)}{\sin(\theta_S)} \frac{\cos(\varphi_r + \theta_S)}{\cos(\varphi_r + \frac{\theta_S}{\cos(\theta)})} \approx \frac{1}{\cos(\theta)}$$

Before θ becomes large the second fraction doesn't vary too much and the significant effect is given by the first fraction, moreover the sine of a small angle can be approximated as the angle its self. This result tells us that if the collector is oriented on the East-West axis the image is modified a lot during the day, especially in the early and late hours of the day. This happens for less if the collector is aligned along the North-South axis. Of course the effect on the image width is additional to the loss of energy in the bundle caused by θ.

Every result so far is valid for a perfect reflector, with no slope errors or imperfection of any kind. If instead a reflector has small, two-dimensional slope errors the image reflected on the receiver will be larger. Let's consider the reflected beam to have an angular amplitude of $(0.53° + \delta)$, where δ is the "Dispersion Angle" which represent a measure of the angular errors of the reflected surface. The diameter of a cylindrical receiver intercepting all the beams would be, in this case:

$$D = 2r_r \sin(\theta_S + \delta/2) = \frac{a \sin(\theta_S + \delta/2)}{\sin(\varphi_r)}$$

The image width on the focal plane would be:

$$W = \frac{2r_r \sin(\theta_S + \delta/2)}{\cos(\varphi_r + \theta_S + \delta/2)} = \frac{a \sin(\theta_S + \delta/2)}{\sin(\varphi_r)\cos(\varphi_r + \theta_S + \delta/2)}$$

It is possible to calculate δ from flux distribution measurement, according to Duffie et al. (2013) a ray-trace method by assuming normally distributed angular errors could be a pretty accurate model.

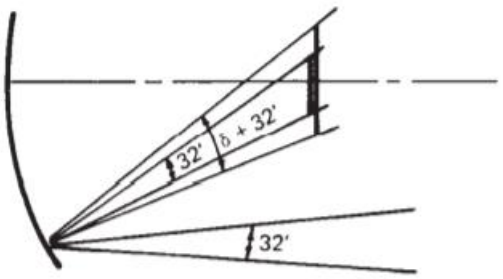

Figure 31 – Schematic of a portion of a concentrator with a dispersion angle δ added to the 0.53◦ solar intercept angle. [J. A. Duffie et al.]

Deterministic ray-tracing is, nowadays, available and effective for parabolic troughs optical errors measurement. However it can result a complex a time consuming method to evaluate such errors to assess the quality of a complete solar field consisting of thousands of square-meters of reflective surface. The computational effort can be reduced with the statistical approach of Bendt and Rabl (1979). This approach adopts a normal distribution to describe all kind of optical imperfection and the Sun's shape. Thus, the *Intercept Factor* is calculated. This coefficient accounts for imperfection such as:

- Tracking inaccuracies;
- Mirror Shape errors;
- Mirror support positions errors;
- Mirror support angular errors;
- Absorber Tube position displacement;
- Modules misalignments;
- Collector torsions (no wind);

A spread of the image depends also on the angle of incidence of beam radiation θ. These effects can be represented by biaxial "*Incident Angle Modifiers*" coefficients in the *x-y* and *x-z* planes. In the x-y plane γ would drop a lot if that component increases, in the x-z plane we must consider two very important effects: the image spread and the variation of the materials' optical problems. The Incident Angle Modifier formula is obtained by experimental results, the one that is used in this work is the following one:

$$K(\theta) = \cos(\theta) + 0.000884 * \theta + 0.00005369 * \theta^2$$

The equation is obtained by tests conducted at SNL [Dudley et al. 1994].

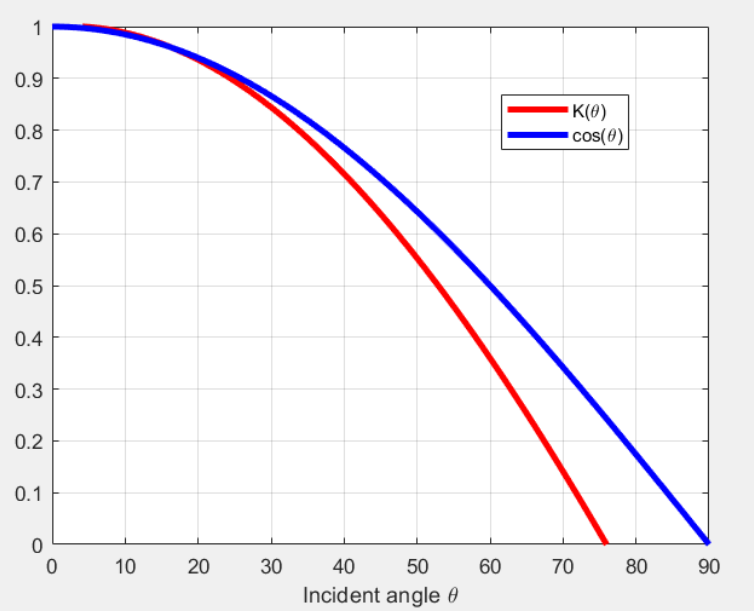

Figure 32 – Incident Angle Modifier vs Angle of Incidence cosine.

Essentially this coefficient accounts for incident angle losses, which includes trough end shading, changes in reflection and refraction, selective coating incident angle effects

2.3.1 – Receiver tube and thermal performance

The HCE (Heat collecting element) is composed by a stainless steel absorber tube inside a glass envelope with bellows at both end. The stainless steel absorber is coated with a special coating (selective coating) to provide the required optical properties. The glass cover has the main purposes of decreasing the heat losses and avoiding the degradation of the absorber, it is usually made of borosilicate glass which maintains good mechanical and thermal properties even under higher temperatures. This cover goes through an anti-reflective treatment to reduce reflective heat losses (a slight chemical etching). The space between the glass cover and the absorber is under vacuum. There is also a getter bridge installed in the annulus, it consists in metallic compounds which can absorb hydrogen that could occasionally permeate from the HTF and reduce the collector's performance if left in the annulus. The getter is an indicator which turns white if vacuum losses are detected in the annulus (when it gets in contact with oxygen).

The bellows provides a seal between metal and glass and allow thermal expansion, moreover they allow the absorber to protrude from the glass so that a welding becomes possible and a long, continuous receiver line is obtainable. In the space obtained between each receiver segment the HCE support brackets can be attached.

Figure 33 – Pictures of Parabolic Trough receivers

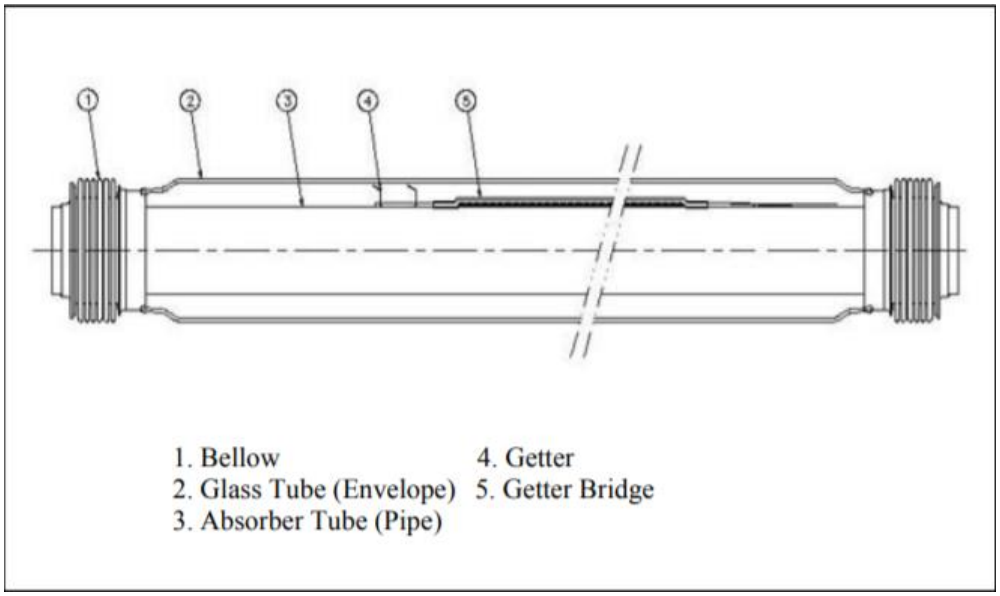

Figure 34 – Scheme of an HCE [R. Forristall (2003)]

Let's discuss now the thermal performance of such a receiver, here is the scheme of the transversal section and the energy fluxes:

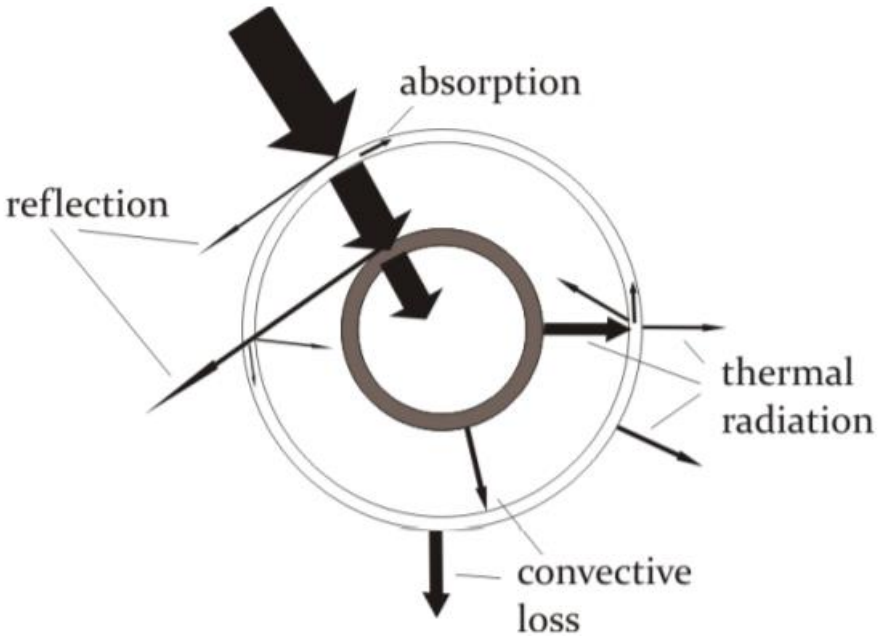

Figure 35 – Energy fluxes at a parabolic trough receiver [D. Rodriguez (2017)]

The Sun energy is concentrated by the reflector but before being absorbed is reflected and absorbed by the glass cover at first and then reflected again by the absorber tube its self. This happens because the glass cover is not fully transparent and the black coating not a black body. This energy is then mostly absorbed by the HTF, the leftover is lost as thermal radiation and convective flux both in the annulus vacuum section and to the environment by the glass cover.

In this report the following assumption will be made:

- Glass doesn't absorbs any energy from the Sun: the glass absorbance value is around 2% and doesn't contribute that much to increase the cover temperature (it would slightly decrease the radiation heat exchange with the absorber);
- The whole receiver pipe (glass + absorber) is assumed to be a grey object surrounded by a large blackbody cavity (the sky);
- Glass doesn't change the beam direction when they pass through (no Snell's Law);
- Receiver's thickness equal to zero (because of the high conductive properties of stainless steel);
- Uniform temperature of absorber and glass cover in circular direction;
- Uniform temperature of HTF in the cross section.

The concentrated energy, according to what has been said so far, is:

$$\dot{Q}''_{conc} = DNI * K(\theta) * \eta_{shad} * \eta_{opt} \quad [W/m^2]$$

η_{opt} is the optical efficiency which accounts for:

- Not perfect receiver absorption properties → *Receiver absorbance* α_{abs};
- Not perfect glass cover transmissive properties → *Glass cover transmittance* τ_{glass};
- Not perfect mirror reflective properties → *Mirror reflectance* ρ_{coll} ;
- Shadow image of the receiver and supports themselves on the mirror → *HCE Shadowing* C_{shad}; (HCE = Heat Collecting Elements)
- *Intercept Factor.*

$$\eta_{opt} = \alpha_{abs} * \tau_{glass} * C_{shad} * \rho_{coll} * \gamma$$

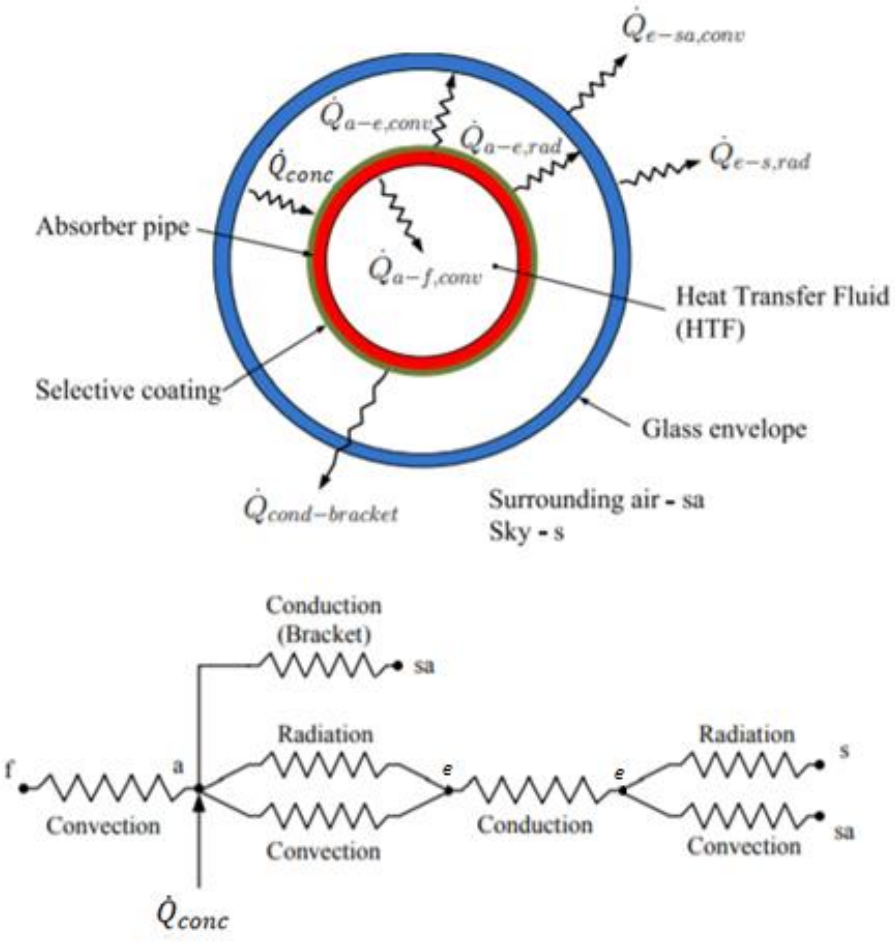

$\dot{Q}_{conc}$ reaches the absorber and is immediately split in two components, the lost and the useful component (absorbed by the HTF).

The Useful Power transferred by convection to the HTF is given by the Newton Law of Cooling:

$$\dot{Q}_{a-f,conv} = \dot{Q}_{use} = h_f A_a (T_a - T_f)$$

h_f is the heat transfer coefficient accounting for convection, A_a is the exchange area of the receiver (unique, according to assumptions made), T_a is the absorber temperature, T_f the HTF one.

The expression of h_f is obtainable from the Nusselt number definition. The following equation is valid only if $Re > 2300$ which happens when the flow is turbulent or transitional and has been developed by Gnielinski (1976):

$$Nu_f = \frac{\left(\frac{f}{8}\right)(Re_f - 1000)Pr_{f,1}}{1 + 12.7\sqrt{\frac{f}{8}}(\mathrm{Pr}_{f,1}^{\frac{2}{3}} - 1)}\left(\frac{Pr_{f,1}}{Pr_{f,2}}\right)$$

With : $$f = \left(1.82\log_{10}(Re_f) - 1.64\right)^{-2}$$

Where:

- f : friction factor for the inner surface of the absorber pipe;
- $Pr_{f,1}$: Prandtl number evaluated at the HTF temperature, T_f;
- $Pr_{f,2}$: Prandtl number evaluated at the absorber inner surface, T_a;

More specifically, the correlation is valid for $0.5 < Pr_{f,1} < 2000$ and $2300 < Re_f < 5E6$. Except for $Pr_{f,2}$ all the properties are calculated at T_1. This formula assumes uniform heat flux and temperatures. If the Reynold number is lower than 2300 the flow is laminar and the Nusselt number will be constant [Incropera et al. (2007)]:

$$Nu_f = 4.36$$

The remaining energy component ($\dot{Q}_{conc} - \dot{Q}_{use}$) is loss from the external surface of the absorber, it is split in two components.

The losses by convection happening in the vacuum annulus must be considered even if their amount is usually much lower than that of the radiation.

If the HCE annulus is under vacuum (< 1 torr) the phenomenon happening will be the free molecular convection [Ratzel et al.1979]

$$\dot{Q}_{a-e,conv} = h_{ann}A_a(T_a - T_{ci})$$

With:

$$h_{ann} = \frac{k_{std}}{\frac{D_a}{2}\ln\left(\frac{D_{ci}}{D_a}\right) + b\lambda\left(\frac{D_a}{Dci}\right)}$$

$$b = \frac{(2-a)(9\gamma-5)}{2a(\gamma+1)}$$

$$\lambda = \frac{2.331 * 10^{-20} * (T_{ann} + 273.15)}{P_a \delta^2}$$

Where:

- D_a = outer absorber surface diameter [m];
- D_{ci} = inner glass envelope surface diameter [m];
- h_{ann}= convection heat transfer coefficient for the annulus gas at T_{ann} [W/m^{2}K];
- T_{ci} = inner glass envelope surface temperature [°C];
- k_{std} = thermal conductance of the annulus gas at standard temperature and pressure [W/mK];
- b = interaction coefficient;
- λ = mean-free-path between collisions of a molecule [cm];
- a = accommodation coefficient
- γ = ratio of specific heats for the annulus gas
- T_{ann} = average temperature (T_a + T_{ci})/2 [°C]
- P_a = annulus gas pressure [mmHg]
- δ = molecular diameter of annulus gas [cm]

This correlation is valid for $Ra < \left(\frac{D_{ci}}{D_{ci}-D_a}\right)^{\frac{4}{3}}$ but overestimates the losses for very low pressures $P_a \leq 0.0001\ torr$.

Annulus Gas	k_{std} [W/m-K]	b	λ [cm]	γ	δ [cm]	h_{34} [W/m^2-K]
Air	0.02551	1.571	88.67	1.39	3.53E-8	0.0001115
Hydrogen	0.1769	1.581	191.8	1.398	2.4E-8	0.0003551
Argon	0.01777	1.886	76.51	1.677	3.8E-8	0.00007499
T_{1avg} = 300 °C, Insolation = 940 W/m^2						

Figure 36 – Heat Transfer Coefficients and Constants for Each Annulus Gas [R. Forristall (2003)]

If $P_a > 1\ torr$ (lost vacuum) the heat exchange occurs by natural convection. The equation used is the Raithby and Holland's correlation for natural convection in annular spaces [Bejan (1995)]:

$$\dot{Q}_{a-e,conv} = \frac{2.425\ k_{ann}(T_a - T_{ci})\left(\frac{PrRa}{0.861+Pr}\right)^{\frac{1}{4}} L}{\left(1+\left(\frac{D_a}{D_{ci}}\right)^{\frac{3}{4}}\right)^{\frac{5}{4}}}$$

With:

$$Ra = \frac{g\beta(T_a - T_{ci})D_a^3}{\nu\alpha}$$

For an ideal gas:

$$\beta = \frac{1}{T_{ann}}$$

Where:

- k_{ann} = thermal conductance of annulus gas at T_{ann} [W/mK];
- L = length of the absorber tube;
- β = volumetric thermal expansion coefficient [1/K]

This correlation is valid for horizontal, long, concentric cylinders at uniform temperatures with $Ra < \left(\frac{D_{ci}}{D_{ci}-D_a}\right)^4$. All physical properties evaluated at T_{ann}.

However most of the losses between the absorber and the envelope occur because of thermal radiation. These losses are estimated by the following equation [Incropera et al. (2007)]:

$$\dot{Q}_{a-e,rad} = \frac{\sigma A_a(T_a^4 - T_{ci}^4)}{\frac{1}{\varepsilon_c} + \frac{1-\varepsilon_e}{\varepsilon_e}\left(\frac{D_a}{D_{ci}}\right)}$$

Where:

- ε_c = thermal emissivity of the selective coating;
- ε_e = thermal emissivity of the glass envelope;

Several assumption has been made here: gas doesn't interfere at all with the exchange, grey surfaces, diffuse reflection and irradiation, glass envelope is considered opaque to infrared radiation and long concentrical isothermal cylinders. Actually, neither glass envelope nor the absorber coating

are grey and the glass is not completely opaque to those radiation, anyway any errors deriving from these assumptions should be small [R. Forristall (2003)].

Another small energy component is lost from the support brackets which are connected with the absorber tube. In a long Parabolic Trough line there must be a support bracket about every 4 meters receiver length. The support brackets are very important because they fix the receiver in the focal point position.

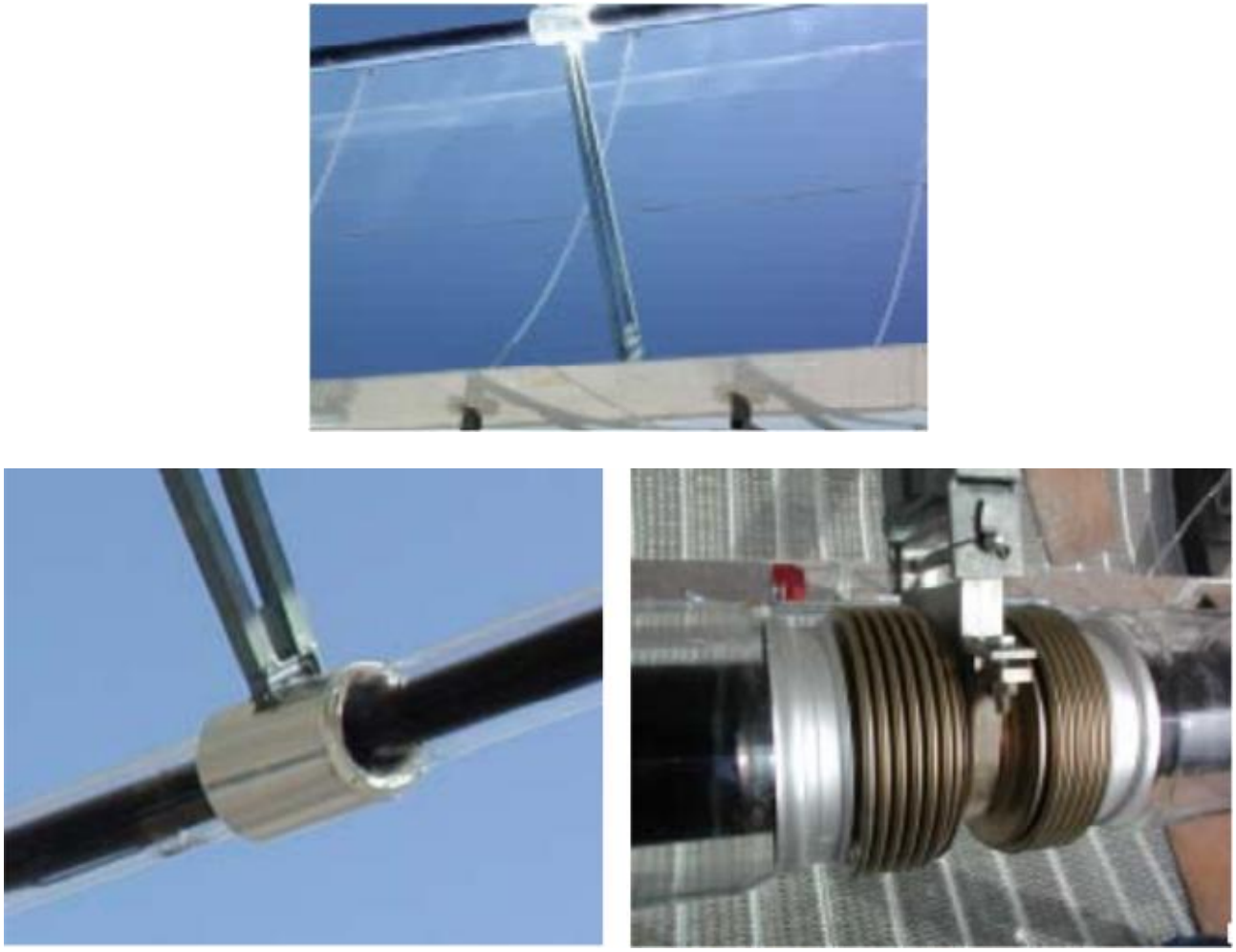

Figure 37 – Example of solar trough receiver support brackets [R. Forristall (2003)]

R. Forristall [3] proposed a good approach for these losses. These are calculated by treating the bracket as an infinite fin with base temperature 10°C less than that of the absorber where the bracket is attached. This temperature accounts for the losses occurring in the short distance between the absorber surface and the minimum cross-sectional area.

The formula used is given by Incropera et al. (2007) [4]:

$$\dot{Q}_{cond-brackets} = N_{HCE}(T_{base} - T_{air})\sqrt{\bar{h}_b P_b k_b A_{cs,b}}$$

- $\bar{h}_b$ = average convection coefficient of bracket [W/m^{2}K];
- P_b = perimeter of bracket [m];
- k_b = thermal conductivity [W/mK];
- $A_{cs,b}$ = minimum cross-sectional area of bracket [m^2];
- T_{base} = temperature at base of bracket [°C];
- T_{air} = ambient temperature [°C];
- N_{HCE}= number of support brackets per HCE.

The perimeter P_b is the one around the two square tubes that run from the absorber attachment to the collector structure. $A_{cs,b}$ is the cross-sectional area of the two small connection tabs connecting the square tubes to the attachment. The smaller this area is, the smaller will be the conduction losses. $\bar{h}_b$ depends on the wind speed, for this calculation purpose the brackets'support can be considered as horizontal tubes [3]: if there is no wind ($< 0.1\ m/s$), Nusselt number is estimated with the Churchill and Chu correlation for natural convection [Incropera et al. (2007)]:

$$Nu_b = \left\{ 0.60 + \frac{0.387 Ra_b^{\frac{1}{6}}}{\left[1 + \left(\frac{0.559}{Pr_{b,air}}\right)^{\frac{9}{16}}\right]^{\frac{8}{27}}} \right\}^2$$

With:

$$Ra_b = \frac{g\beta_{b,air}(T_{base} - T_{air})d_{eff}^3}{\nu_{b,air}\alpha_{b,air}}$$

$$T_{b,air} = \frac{T_{base} + T_{air}}{2}$$

$$Pr_{b,air} = \frac{\nu_{b,air}}{\alpha_{b,air}}$$

Where d_{eff} is the effective diameter of the support. Every term with the subscript "*b,air*" is calculated at $T_{b,air}$. This formula is valid for $10^5 < Ra_b < 10^{12}$.

If there is wind ($> 0.1\ m/s$), Zhukauskas' correlation is used [Incropera et al. (2007)]:

$$Nu_b = C\ Re_b^m\ \mathrm{Pr}_{air}^n \left(\frac{Pr_{air}}{Pr_b}\right)^{\frac{1}{4}}$$

With:

$$Re_b = \frac{\rho_{air} W_s d_{eff}}{\mu_{air}}$$

Re	C	m
1-40	0.75	0.4
40-1000	0.51	0.5
1000-200000	0.26	0.6
200000-1000000	0.076	0.7

And:

$$\begin{cases} n = 0.37 & if\ Pr_{air} \leq 10 \\ n = 0.36 & if\ Pr_{air} > 10 \end{cases}$$

Pr_b is the Prandtl number calculated at the support's temperature.

This correlation is valid for $0.7 < Pr_{air} < 500$ and $1 < Re_b < 10^6$

k_b is the thermal conductivity of the support bracket, the material "plain carbon steel" can be assumed for this purpose, if this is considered at 600 K [R.Forristall (2003)]:

$$k_b = 48\ W/mK$$

With T_{base} in [K].

Coming back to the absorber pipe, the sum $(\dot{Q}_{a-e,rad} + \dot{Q}_{a-e,conv})$ is then transferred by conduction through the glass envelope. This passage of the model is fundamental because allows to calculate the outer diameter temperature and its knowledge is mandatory for the followings calculations. The equation is well known:

$$Q_{e,cond} = \frac{2\pi k_e L(T_{ci} - T_{co})}{\ln\left(\frac{D_{co}}{D_{ci}}\right)}$$

Where k_e is the thermal conductivity of the glass envelope.

At this point, once the heat flux has reached the external surface of the envelope it is lost to the surrounding by convection with the air and by radiation with the sky.

The convection component is again heavily dependent on the wind speed, the same set of formulas is used again. This time we don't have to look for an effective diameter since the exchanging surface is an actual pipe:

$$\dot{Q}_{e-sa,conv} = h_{sa} A_{co} (T_{co} - T_{air})$$

No wind case:

$$Nu_{co} = \left\{ 0.60 + \frac{0.387 Ra_{co}^{\frac{1}{6}}}{\left[1 + \left(\frac{0.559}{Pr_{co,air}}\right)^{\frac{9}{16}}\right]^{\frac{8}{27}}} \right\}^2$$

With:

$$Ra_{co} = \frac{g \beta_{co,air} (T_{co} - T_{air}) D_{co}^3}{\nu_{co,air} \alpha_{co,air}}$$

$$T_{film} = \frac{T_{co} + T_{air}}{2}$$

$$Pr_{co,air} = \frac{\nu_{co,air}}{\alpha_{co,air}}$$

Wind case:

$$Nu_b = C \; Re_{co}^m \; \mathrm{Pr}_{\mathrm{air}}^n \left(\frac{Pr_{air}}{Pr_{co}}\right)^{\frac{1}{4}}$$

With:

$$Re_{co} = \frac{\rho_{air} W_s D_{co}}{\mu_{air}}$$

The listed ranges of validity for the support brackets losses remain valid.

The last term to analyze is the radiation transfer between the glass envelope and sky, this quantity depends mostly on the temperature difference between the outer glass envelope and the sky. We must remember about the assumption of grey convex object in large blackbody cavity. The net radiation transfer is:

$$\dot{Q}_{e-s,rad} = \sigma \varepsilon_e A_{co} (T_{co}^4 - T_{sky}^4)$$

Where the sky temperature T_{sky} is assumed to be 8°C below the ambient temperature [R. Forristall (2003)]:

$$T_{sky} = T_{air} - 8$$

Although not necessary, it is possible to estimate several heat transfer coefficients which can be very useful for the setting up of a multi-equation system.

The following equations can be written:

$$\dot{Q}_{loss} = h_{ann} A_a (T_a - T_{ci}) + \frac{\sigma A_a (T_a^4 - T_{ci}^4)}{\frac{1}{\varepsilon_e} + \frac{1-\varepsilon_c}{\varepsilon_c}\left(\frac{D_a}{D_{ci}}\right)} + N_{HCE}(T_{base} - T_{air})\sqrt{\bar{h}_b P_b k_b A_{cs,b}} =$$

$$= \frac{2\pi k_e L (T_{ci} - T_{co})}{\ln\left(\frac{D_{co}}{D_{ci}}\right)} + N_{HCE}(T_{base} - T_{air})\sqrt{\bar{h}_b P_b k_b A_{cs,b}} =$$

$$= h_{sa} A_{co} (T_{co} - T_{air}) + \varepsilon_e \sigma A_{co}\left(T_{co}^4 - T_{sky}^4\right) + N_{HCE}(T_{base} - T_{air})\sqrt{\bar{h}_b P_b k_b A_{cs,b}}$$

All the heat loss coefficients can be grouped in one term this way:

$$\dot{Q}_{loss} = U_L A_a (T_a - T_{air})$$

U_L is called "*Loss coefficient*" and accounts for all the loss phenomena involved in the system.

For a linear concentrating system with cylindrical receivers, the "*Overall heat transfer coefficient*" can be defined (neglecting the thickness of the absorber tube):

$$U_0 = \frac{1}{U_L^{-1} + h_f^{-1}}$$

It accounts for all the heat transfers between the HTF and the surrounding.

The useful energy transferred at the HTF is, as mentioned [Duffie et al. (2013)]:

$$\dot{Q}_{use} = \dot{Q}_{conc} - \dot{Q}_{loss} =$$

$$= A_{apert} \dot{Q}''_{conc} - A_a U_L (T_a - T_{air}) =$$

$$= h_f A_a (T_a - T_f)$$

Where A_{apert} is the Aperture Area of the collector, if T_a is eliminated from the two previous equations we obtain:

$$\dot{Q}_{use} = F' A_{apert}\left[\dot{Q}''_{conc} - \frac{A_a}{A_{apert}} U_L (T_f - T_{air})\right]$$

Where F' is the "*Collector Efficiency Factor*" defined as:

$$F' = \frac{U_L^{-1}}{U_L^{-1} + h_f^{-1}}$$

As a consequence:

$$F' = \frac{U_0}{U_L}$$

This coefficient represents the ratio of the actual useful energy gain to the useful gain that we would obtain if the absorbing surface was at the average fluid temperature.

It is also useful to define a coefficient that relates the actual energy gain of a collector to the gain we would have if the whole absorber surface was at the fluid inlet temperature. This figure is called "collector heat removal factor" F_R:

$$F_R = \frac{\dot{m}_f c_{p,f}(T_{f,i} - T_{f,o})}{A_{apert}\left[\dot{Q}''_{conc} - \frac{A_a}{A_{apert}} U_L(T_{f,i} - T_{air})\right]}$$

Equivalently:

$$\dot{Q}_{use} = F_R A_{apert}\left[\dot{Q}''_{conc} - \frac{A_a}{A_{apert}} U_L(T_{f,i} - T_{air})\right]$$

Where $T_{f,i}$ and $T_{f,o}$is the inlet/outlet fluid temperature at the respective tube sections of the considered length of HCE. It would be worth noting that the two coefficients F_R and F' are equivalent if the fluid temperature gradient is null.

Just to make things more clear, T_f is the average local temperature in the HTF pipe: we reach this temperature only in one spot of the tube length section *L* considered and is not defined as the arithmetic mean:

$$T_f \neq \frac{T_{f,o} + T_{f,i}}{2}$$

This number appears in all the correlations where the HTF heat exchange is involved and makes the calculation locally inaccurate. The shorter the length section *L* considered, the more accurate all the calculation are going to be.

3 – Weather data processing

The following analysis is based on the available weather data, this is a mandatory passage of this work because it will allow to look at the final results in the proper way. In other words we cannot say how good the field is if we don't know the available amount of energy and it is distributed. This data is a typical meteorological year (TMY) based on the years 2005-2017.

3.1 – DNI, GHI and DHI

The total annual energy per square meter from DNI and GHI is calculated:

Total annual energy from DNI: 2167 kWh/m^2/yr.

Total annual energy from GHI: 2148 kWh/m^2/yr.

The average daily energy received from DNI is 5.9 kWh/m^2/day, with a small variation across the year, minimum is 5.1 kWh/m^2/day in September, maximum is 6.8 kWh/m^2/day in March.

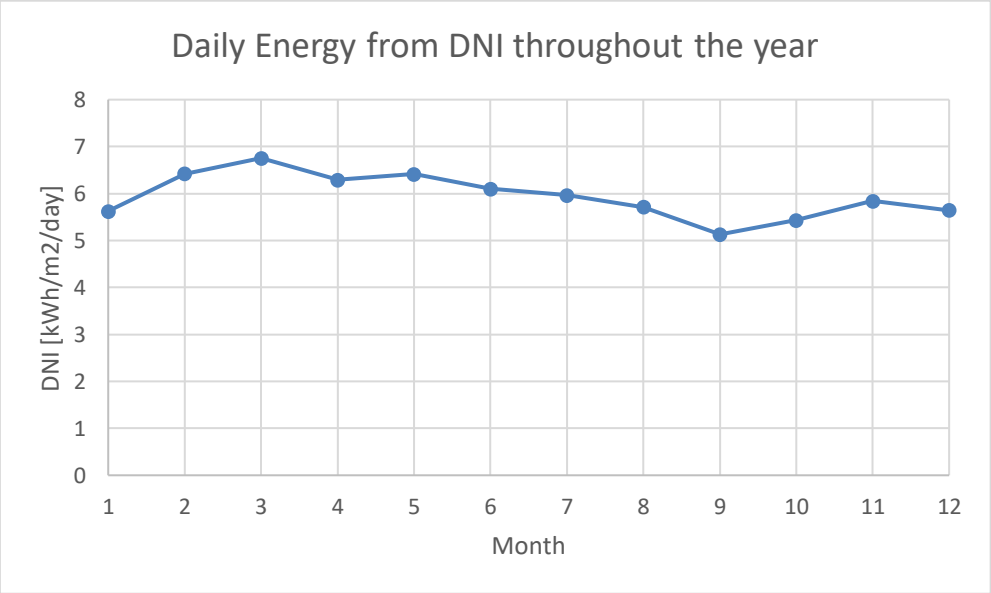

Figure 38 – Daily energy from DNI.

The average and maximum DNI per month show a similar tendence, with an average DNI (zero values are not considered in the calculation) ranging between 472 W/m2 and 619 W/m2. There is a consistent maximum DNI of 850-880 W/m2 throughout the year.

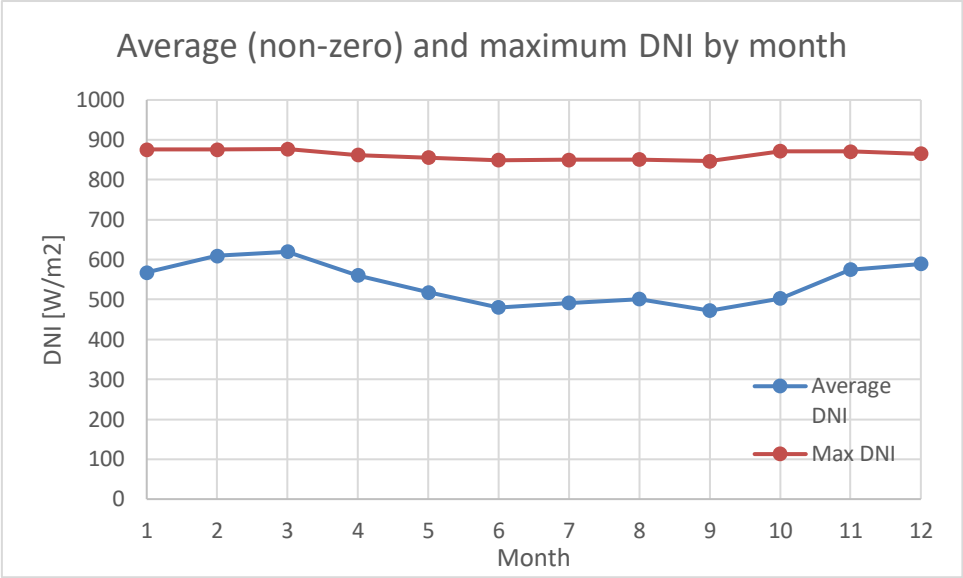

Figure 39 – Average and maximum DNI by month.

If the solar field is well designed, its performance should be consistent across the year, with peak useful energy obtained in March.

Between April and October there is a drop in the DNI during the early afternoon, which may affect negatively the performance of the system.

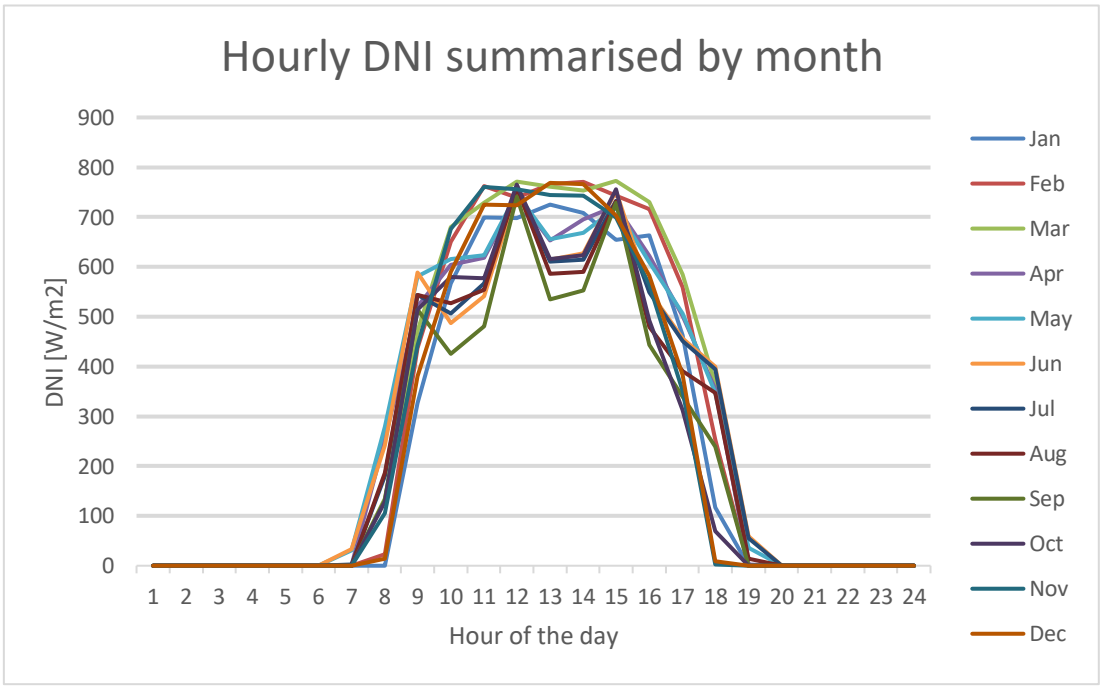

Figure 40 – Hourly DNI summarized by month.

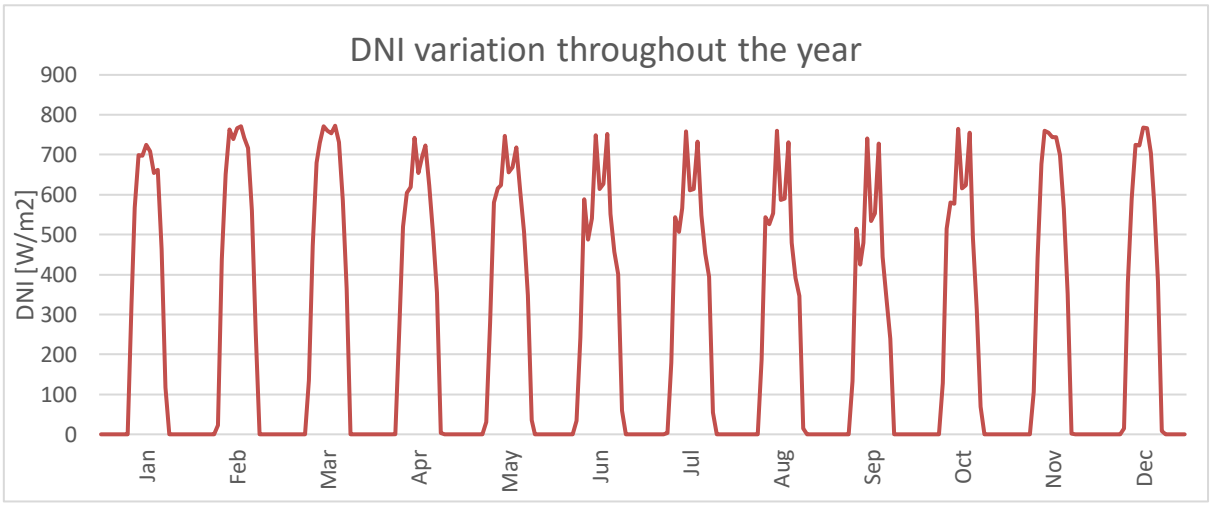

Figure 41 – DNI variation throughout the year.

3.2 – Wind data

The yearly average wind speed is 4.0 m/s. The wind speed varies a little throughout the year. The monthly average varies from 3.1 m/s in December to 4.9 m/s in June. The maximum wind speed during the year was 13.4 m/s in February.

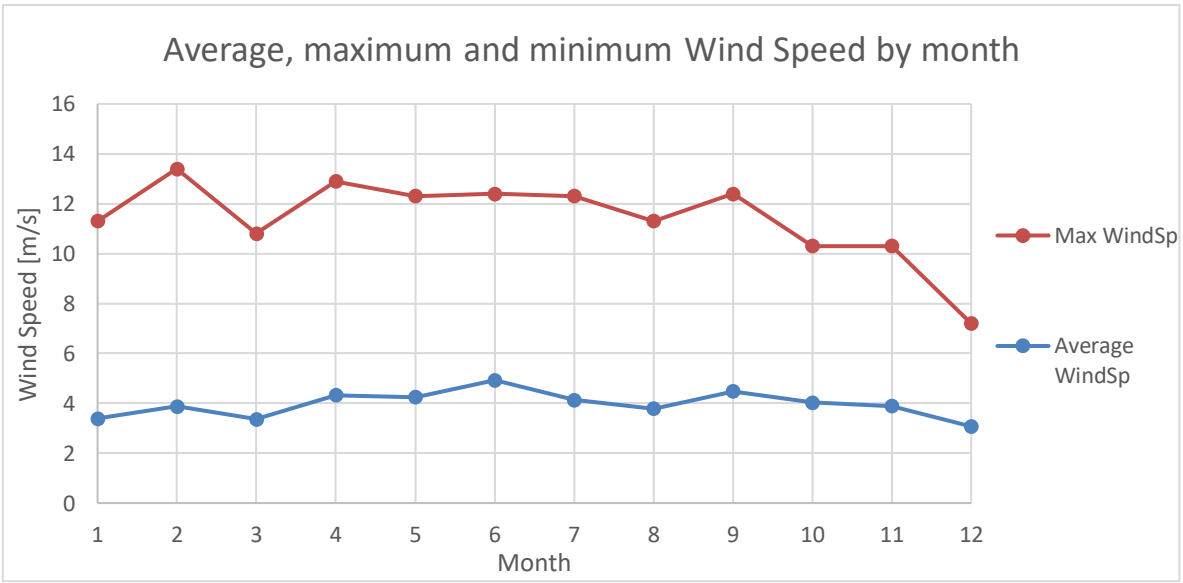

Figure 42 – Average, maximum and minimum wind speeds by month.

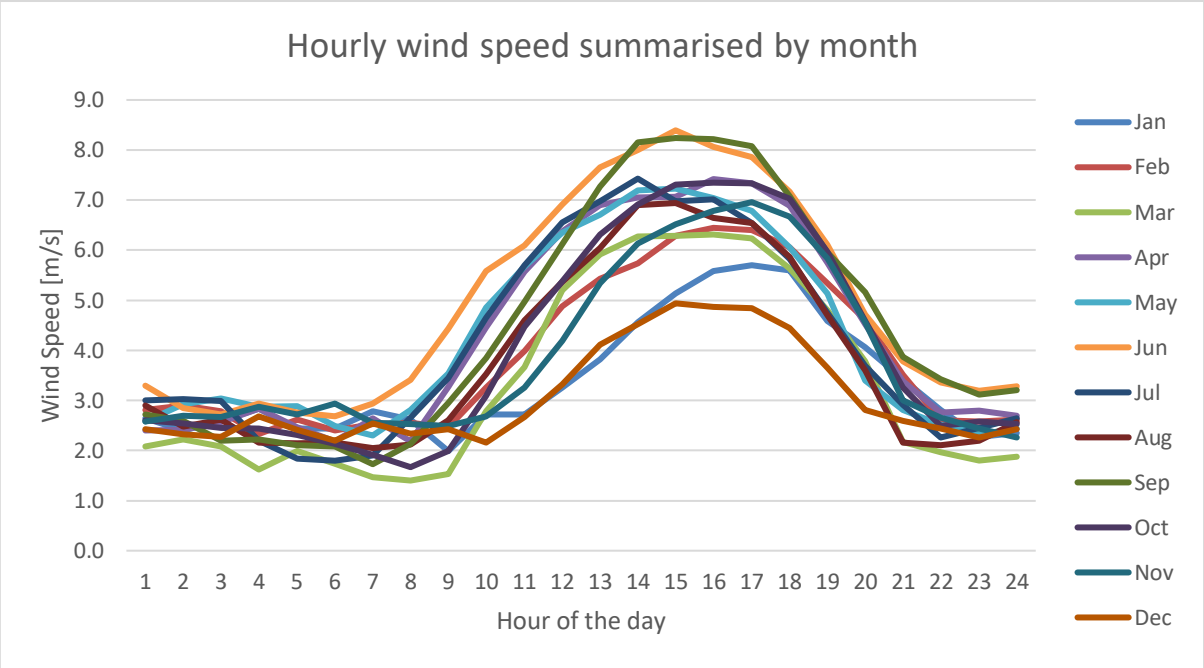

Figure 43 – Hourly wind speed summarized by month.

The figure shows that there is a significant difference between the wind speed during the day and during the night. During the night there is a consistent wind speed ranging between 2 m/s and 3 m/s throughout the year. However, during the day there is a peak in wind in the early afternoon, minimum is 5 m/s in December, maximum is 8.4 m/s in June.

The annual wind rose shows the most frequent directions the wind assumes. Two are the most frequent directions, the North-West and the North-North-East. The lower wind speeds usually come from the NNE direction with the higher wind speeds from the NW.

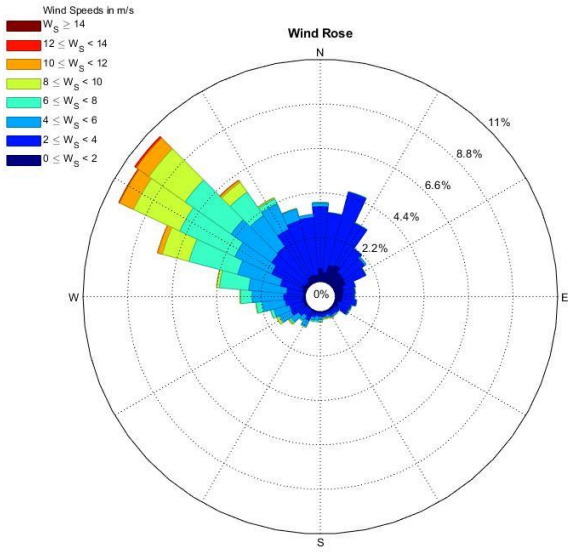

Figure 44 – Wind rose.

3.3 – Sandstorms and dust considerations

Saudi Arabia is a country where dust activity is pretty frequent and, since dust has a significant effect on the obtainable energy from a concentrated solar power system, it is an key aspect to consider. Studies have been done on the dust frequency throughout the year in different regions of Saudi Arabia.

Labban (2016) used data obtained over 29 years from meteorological stations across Saudi Arabia to analyze the seasonal frequency and type of dust activity. Three kind of dust events were identified - Haze, Local Dust Events (LDE), and Dust Storms (DS). Haze is defined as the suspension of dust in the air caused by a dust storm, which may have either occurred in the site its self or from another site nearby. LDEs are defined as raised dust or sand, well developed dust whirls, or distant or past dust storms. Dust Storms are defined as such only when they are characterized by visibility less than 1 km. In the case of CSP, all three categories would have a significant negative effect on the incoming solar radiation.

The table below shows the average number of days per season that each type of activity occurs, along with the annual average for Tabuk, which is approximately 150 km from the solar field site.

	Winter	***Spring***	***Summer***	***Autumn***	***Annual***
Haze	*8*	*19*	*11.1*	*8.6*	*46.8*
LDE	*10.9*	*23.9*	*13*	*8.5*	*56.4*
DS	*0.2*	*0.7*	*0.2*	*0.1*	*1.2*
Total	*19.1*	*43.6*	*24.3*	*17.2*	*104.4*

By summing the total number of days affected by dust activity we can obtain 104 days per year. Dust activity is higher during the spring (February-April).

A significant dust fall on the solar field would lead to a reduction of the reflectance of the mirrors and so of the performance of the dome. Regular maintenance washing activity of the mirrors will be required to maintain the reflectance and keep the optical efficiency of the reflectors high. It should be done with a frequency of once every one or two weeks. The actual frequency required will depend mostly on the season and can be monitored by regularly measuring the reflectance of the mirrors with a reflectometer.

3.4 – Temperature and humidity

The yearly average temperature is 26.1 °C, with a minimum of 13.6 °C in October and a maximum of 42 °C in September.

The figure below shows the temperature variation during the year, where it can be seen that the average temperature varies between 20°C and 30 °C, the minimum temperature is relatively constant around 15 °C and the maximum ranges from 27 to 42 °C.

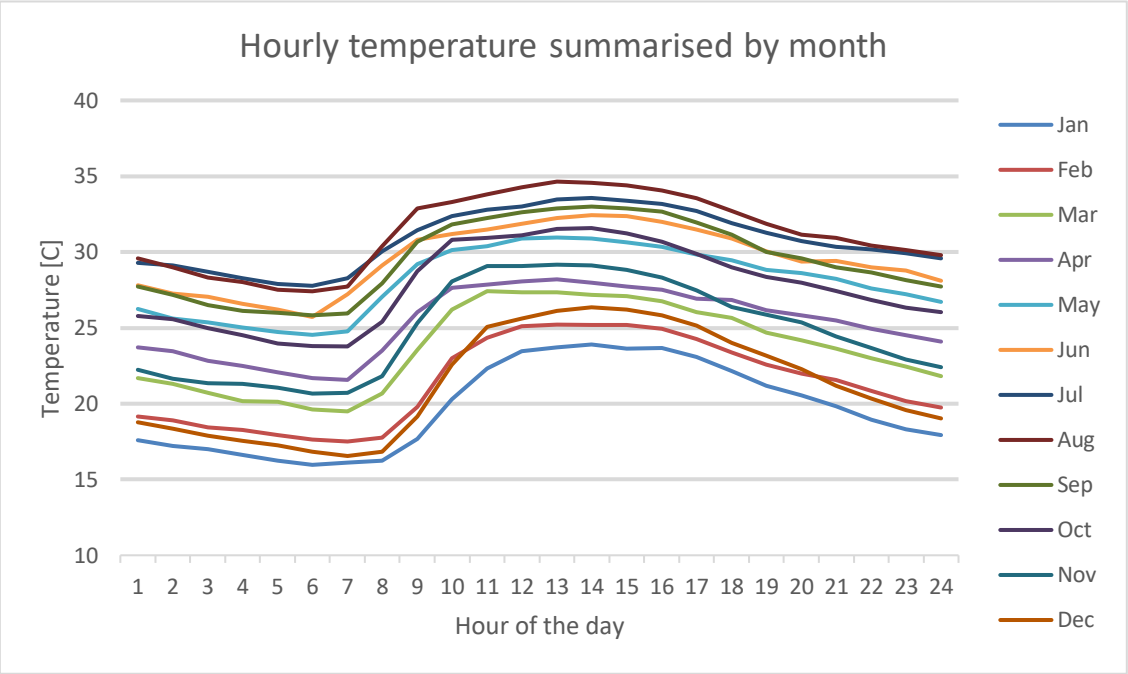

Figure 45 – Average, maximum and minimum temperature by month.

The next figure shows that during the day the temperature rapidly rises starting from 7am and reaches its maximum around 1pm. It then decreases much slowly throughout the day and the night, with no sudden drop. The temperature profile follows the same pattern throughout the year rising and falling with the average temperature.

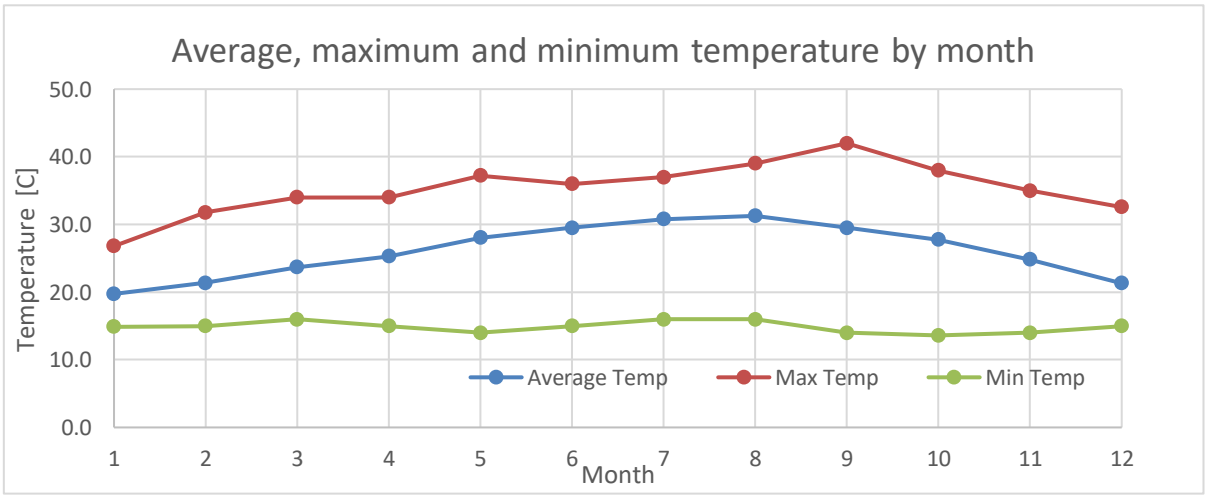

Figure 46 – Hourly temperature summarised by month.

The yearly average relative humidity is 65%, a reasonable value given the location. The humidity ranges between 20% and 100%. The next figure shows that there is a very small change in the average humidity throughout the year, between 56% in March and 77% in September.

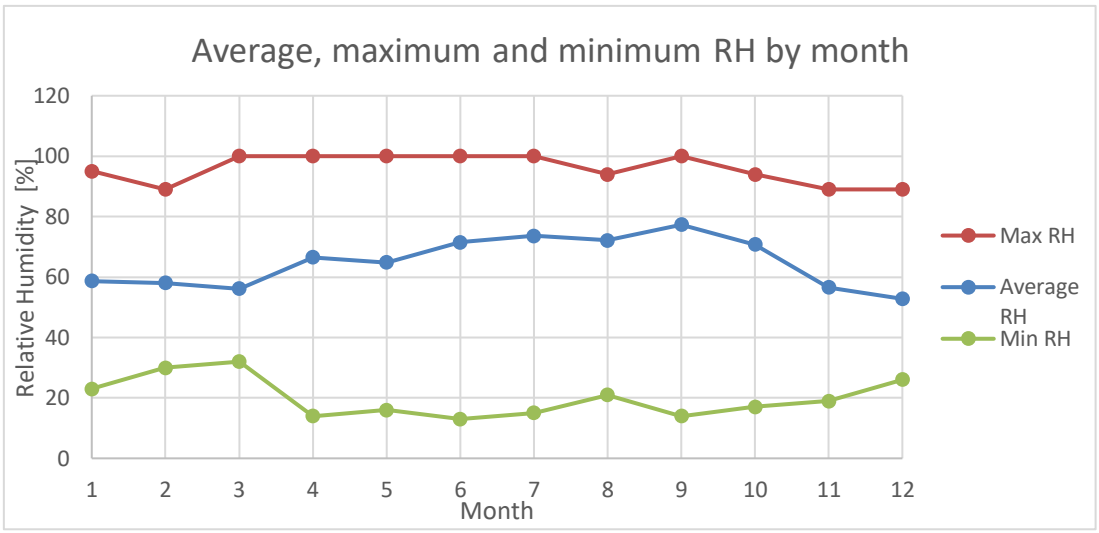

Figure 47 – Average, maximum and minimum RH by month.

The humidity appears, in general, to be higher during the night time, when the temperature generally drops. It rapidly drops during the morning and then slowly increases throughout the following day and night.

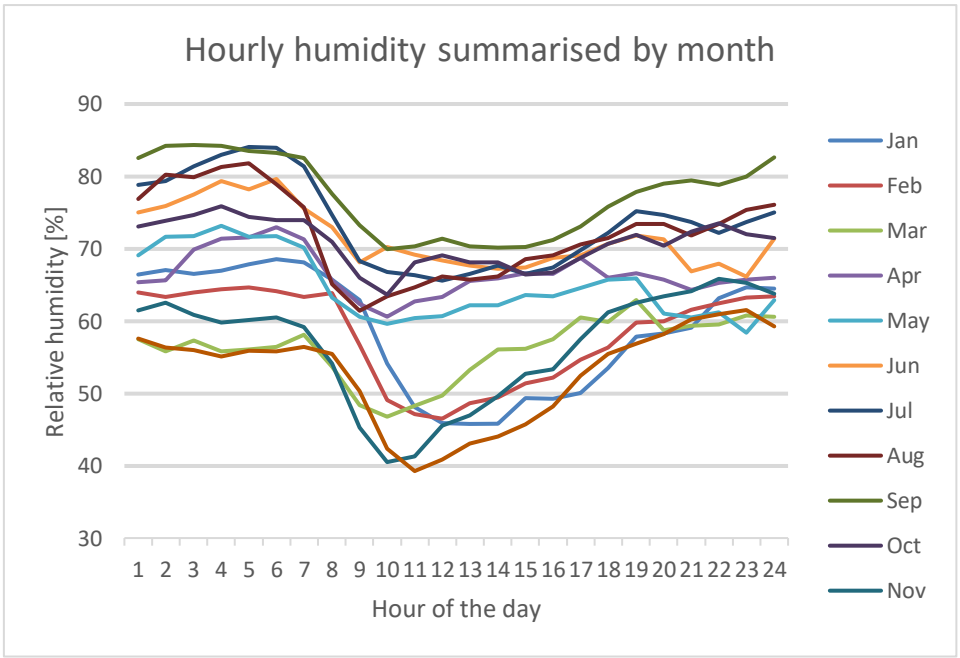

Figure 48 – Average humidity summarized by month.

4 – Model development

The model developed allows to calculate the performances of a Parabolic Trough solar field in steady state conditions given input weather conditions. However, with a slight modification of the Matlab code, it is also possible to estimate the reflective area needed to fulfill a given power and temperature difference requirement.

It is possible to summarize the working principle of the model in different steps:

- Setting geometry of collectors and layout (number of parallel rows and rows length);
- Weather data processing: Sun tracking and Shading evaluation (available energy calculation);
- Optical inaccuracies calculation;
- Non-linear equation system solving for mass flow rate needed, this will lead to a first guess of this value that should result in an outlet temperature of 380°C;
- Similar non-linear equation system solving (using mass flow rates just obtained) for performance calculation. Multiple iteration of this one could be needed in order to achieve a good accuracy for the outlet temperature;
- Post-processing for efficiencies and figure of merit evaluation.

These steps will be executed every hour of the year but only the hours where a $\dot{Q}''_{conc}$ of more than *130 W/m²* results will be taken into account for the final step and the figure of merit calculation. This is because, in general, with relatively low $\dot{Q}''_{conc}$ values and sufficiently high wind speeds, the system will be unable to work correctly by reaching an unwanted thermodynamic equilibrium state before the outlet.

4.1 – Requirements

The model has been developed for sizing and estimating the energetic performances of a Solar Field (main purpose is the calculation of the reflective area). For ease of installation, cost and maintenance, standard parabolic troughs with standard evacuated tube receivers is the type of collector chosen (the company is not known), the heat transfer fluid chosen is the synthetic oil *Therminol VP-1*, a very thermally stable HTF with possible performances in the range of 12°C - 400°C. Such field is intended to fuel a 3 stage Multiple Effect Distillation (MED) saltwater plant by means also of a thermal storage that would allow night-time operation but not without a corresponding oversizing of the solar field.

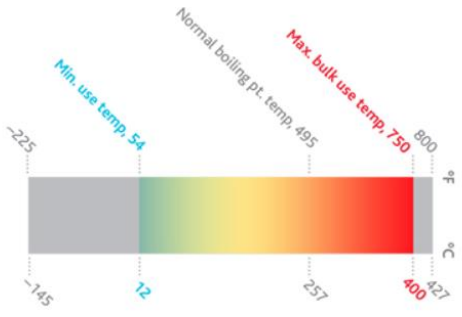

Figure 49 – Working range of Therminol VP-1

With all this information in mind, operational parameters required are:

- $T_{in,field} = 300°C$
- $T_{out,field} = 380°C$

- Working time with $\dot{Q}_{use} = 3\ MW : 58\%\ of\ the\ year$
- Working time with $\dot{Q}_{use} = 4.5\ MW : 23\%\ of\ the\ year$

The available Solar Field area is:

- $170\ m\ length\ North - South$
- $110\ m\ width\ East - West$

4.2 – Tracking strategy

First thing first, the choice of the tracking strategy. As mentioned before, there are two possible way of tracking the Sun in our case:

- North-South horizontal rotation axis (collectors point at East in the morning, at West in the afternoon);
- East-West horizontal rotation axis

The choice depends mainly on the location because the sun paths in the sky depend on it. In this case, since the location in question is relatively close to the equator, the strategy that allows to minimize the Incident Angle θ and maximize the energy obtained in one year will most likely be the "North-South rotation axis", however the other strategy is very well known to be valid for an homogeneous and consistent distribution of $\dot{Q}_{use}$ throughout the year.

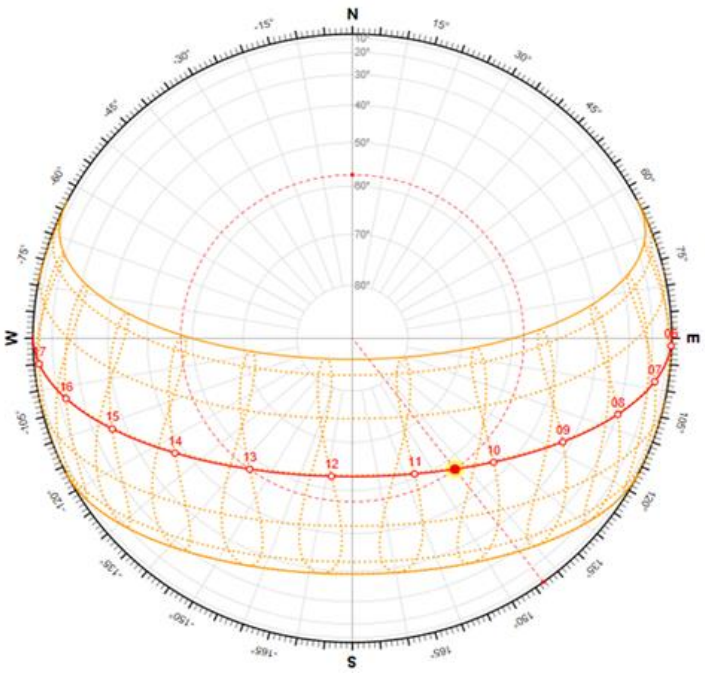

Figure 50 – Sun path diagram of the Solar Field location.

Then, for the calculation of the available energy we must consider only the *DNI* column of the weather data file, this is because parabolic troughs are unable to concentrate the diffuse component of the radiation.

4.3 – Optical inaccuracies calculation

Parabolic troughs collectors suffer, apart from sun tracking losses, from other reduction on the available energy that can be concentrated. These reduction are mostly caused by optical properties of the materials and installation inaccuracies. The coefficient that account for these losses is the *Optical Efficiency.* In this paragraph the assumption made and some values are shown.

The Optical Efficiency is defined as:

$$\eta_{opt} = \alpha_{abs} * \tau_{glass} * C_{shad} * \rho_{coll} * \gamma$$

The following values have been used in the simulation:

Factor	***Value***
Receiver absorbance α_{abs} (Solel UVAG Avg coating)	*0,955*
Glass cover transmittance τ_{glass} (Borosilicate glass)	*0,970*
HCE Shadowing C_{shad} (NREL report [Price et al. (2002)])	*0,974*
Mirror reflectivity ρ_{coll} (Flabeg silver mirrors)	*0,935*

There are more reductions caused by optical inaccuracies, those ones which change the direction of the beam after they bounce off the reflector. The "*Intercept factor*" γ accounts for all of them and is calculated by means of the statistical ray-tracing method of Bendt and Rabl [16]. This method uses Normal Distribution as Probability Density Functions of angular deviations from the perfect optics to describe all kinds of geometric imperfections as well as the Sun shape. Thus, a

Monte Carlo method has been implemented, here each component contributing to the intercept factor quality is described by the standard deviation σ_i ("*Beam Spread*") of its distribution function:

The effect of geometry imperfections can be represented by summing the squares of the individual standard deviations, thus the variance σ^2 ("*Total Beam Spread*") is given by the following formula:

$$\sigma_{total}^2 = \sum_i (a_i * \sigma_i)^2 + \sigma_{sun}^2$$

Where σ_{sun} is the Solar Acceptance Angle, having a value of 0.267° (4.653 *mrad*). For all the other σ_i these numbers are adopted, they are typical for an *Eurotrough* collector [7], so they can be assumed as reliable. Parameters for the mirror slope are weighted by 2 to account for the double effect of mirror slope deviation on total beam spread:

Optical inaccuracy	$\boldsymbol{\sigma}$ ***in mrad***	***Weighting factor*** $\boldsymbol{a_i}$
Mirror Shape	*1.9*	*2*
Mirror Support Position	*0.8*	*2*
Mirror Support Angle	*1.0*	*2*
Absorber Tube Position	*1.4*	*1*
Module Alignment	*1.0*	*1*
Collector Torsion (no wind)	*1.0*	*1*
Tracking Accuracy	*1.0*	*1*
Linear Sun Shape	*4.653*	*1*

According to Bendt and Rabl [16], the Intercept Factor γ is a function of the product $(C\sigma_{total})$:

$$\gamma = \int_{-\infty}^{+\infty} d\theta \, f(C\theta) \frac{1}{\sigma_{total}\sqrt{2\pi}} \exp\left(\frac{\theta^2}{2\sigma_{total}^2}\right)$$

Since the cone image width increases with the parabolic radius, a unique, average radius was needed:

$$\overline{r_r} = \int_{-\varphi_R}^{\varphi_R} r_r \, d\varphi = \int_{-\varphi_R}^{\varphi_R} \frac{2f}{1+\cos(\varphi)} \, d\varphi$$

200000 experiments has been run (each one of them is a Solar beam) and the *Sample Average* $\xi_i^{(N)}$ has been calculated:

$$\gamma = \xi_i^{(N)} = \frac{1}{N} \sum_{i}^{N} \xi_i$$

At the end the calculation gave back a result of $\gamma = 0.9864$

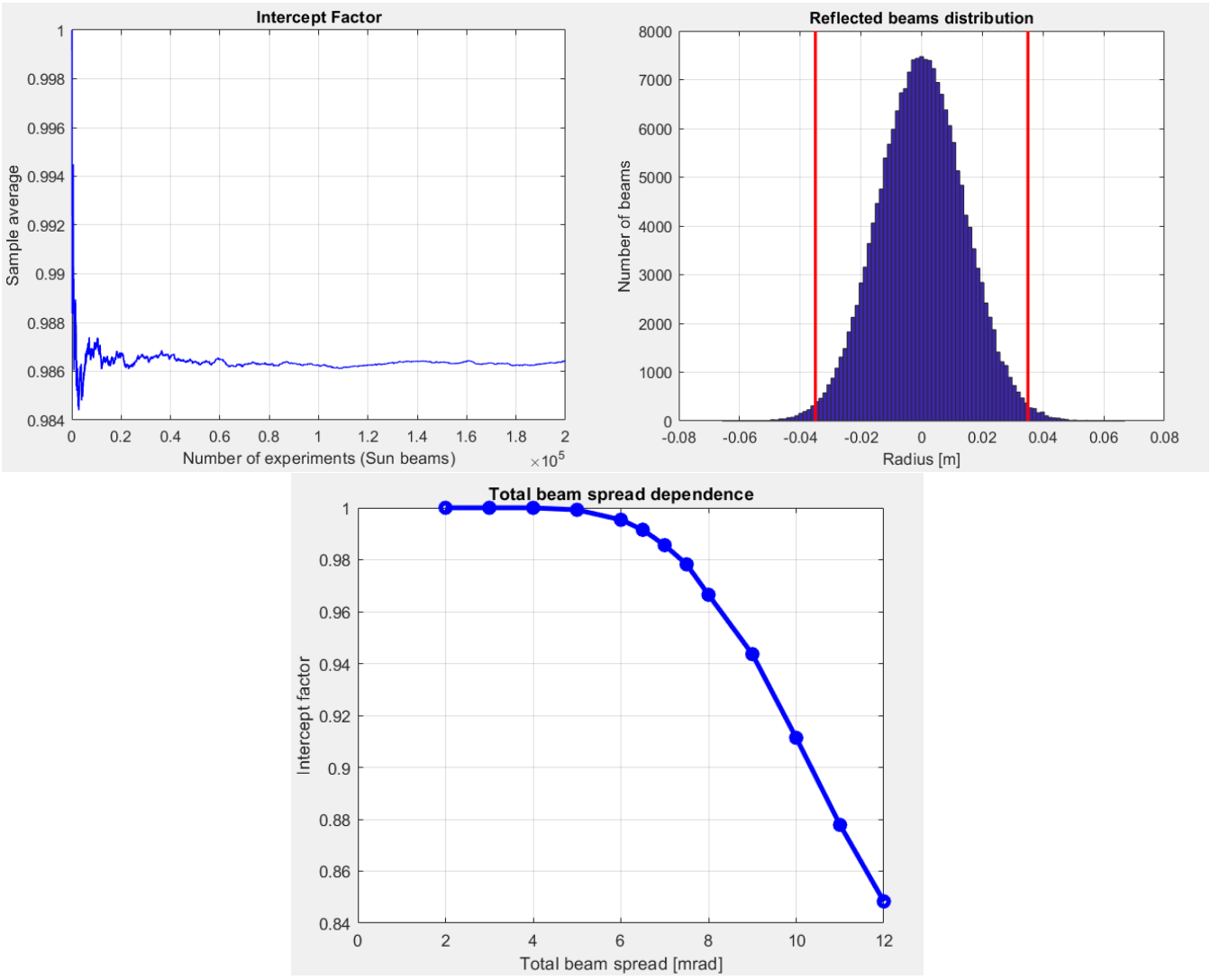

Figure 51 – (Left) Distribution of the beams around the focal point. (Right) Sample average calculation. (Down) Correlation between Total Beam Spread and Intercept Factor.

Now, we can calculate the "Optical Efficiency" η_{opt} as follows:

$$\eta_{opt} = \alpha_{abs} * \tau_{glass} * C_{shad} * \rho_{coll} * \gamma = 0.832$$

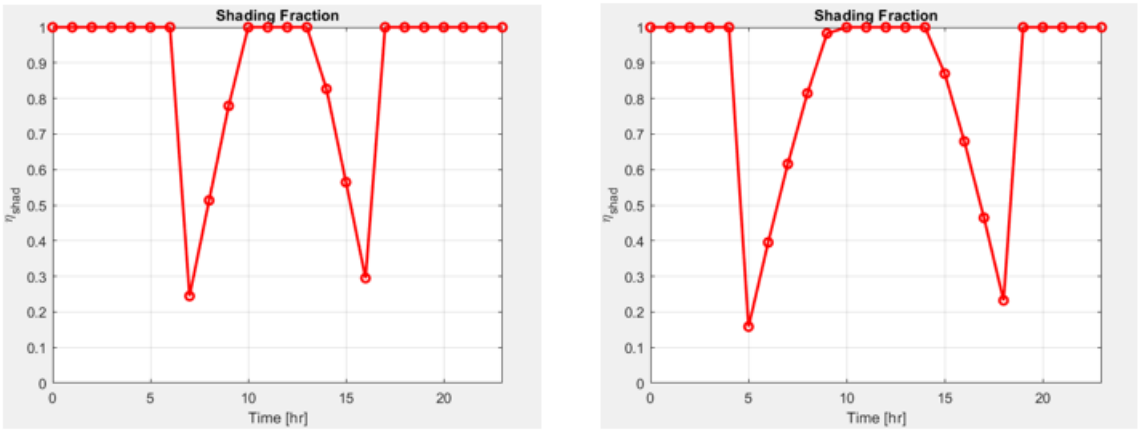

Figure 52 – Shading coefficient p = 7 m. (Left) December 21st. (Right) June 21st.

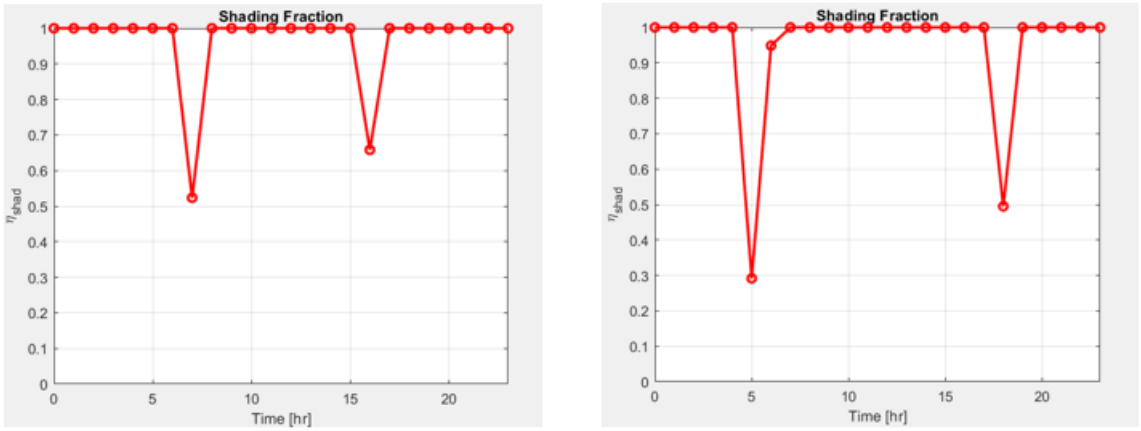

Figure 53 – Shading coefficient p = 20 m. (Left) December 21st. (Right) June 21st.

Eventually, by multiplying everything by the *Shading Coefficient*, the energy concentrated in the receiver is:

$$\dot{Q}''_{conc} = DNI * K(\theta) * \eta_{shad} * \eta_{opt} \quad [W/m^2]$$

This value will be used as input in the next step.

4.4 – Mass flow rate and performance calculation

In this paragraph the working principle of the performance calculation is described.

As mentioned, input data of this code are the number of rows of the parallel configuration and the number of collector elements in each row. It is important to keep in mind that the number of collector elements isn't, in general, the actual number of parabolic troughs modules present in each row. It represent a discretization of a continuous, longer, collector divided for this purpose in

elements having length "*L*". Between each collector, no thermal losses are considered. It now appears obvious that it will approximate better the performances of a field made of continuous collectors.

In order to calculate properly the performances of the field, we require the outlet temperature to be 380°C (inlet is 300°C). The following law is always valid:

$$\dot{Q}_{use} = \dot{m}_f c_{p,f} \Delta T_{field}$$

Since $\dot{Q}_{use} = \eta_I \dot{Q}_{conc}$ and η_I is almost constant with $\dot{m}_f$, ΔT_{field} changes according to $\dot{m}_f$. Thus, with good approximation:

$$\dot{m}_f \Delta T_{field} = cost$$

The code will solve two non-linear equation system. Each one of them is solved for every collector but considering only one row because all the others behaves exactly the same (they all have the same temperature difference between inlet and outlet) and everything will be needed afterwards is an easy multiplication.

Thus, for each hour of the year with $\dot{Q}''_{conc} \geq 130 \frac{W}{m^2}$ resulting from the previous process:

- The first system is solved using as input data the temperature at the inlet and outlet section of every collector (element). We calculate as follows the ΔT_{coll} in each of them:

  $$\Delta T_{coll} = \frac{T_{out,field} - T_{in,field}}{N_{coll}}$$

  The mass flow rate $\dot{m}_f$ needed in order to reach 380°C at the outlet of the field is obtained. Obviously this is not going to be, in general, a precise result because the ΔT_{coll} is not actually constant along the row but still a good initial guess to start the iterative method.

- The second system is solved using the mass flow rate value just obtained as input. A tolerance limit is fixed, if the resulting outlet temperature doesn't fit in the range:

  $$[380° - tolerance\ , 380° + tolerance]$$

  Then this system is solved again using another value of $\dot{m}_f$, calculated according to a chosen iterative method.

First system:

$$
\begin{cases}
\dot{Q}_{use} = F_R LW\left[\dot{Q}''_{conc} - \dfrac{\pi D_a}{W} U_L (T_{in} - T_{air})\right] \\
\dot{Q}_{use} = F' LW\left[\dot{Q}''_{conc} - \dfrac{\pi D_a}{W} U_L (T_f - T_{air})\right] \\
\dot{Q}_{use} = h_f L \pi D_a (T_a - T_f) \\
\dot{Q}_{use} = \dot{m}_f c_{p,f} (T_{out} - T_{in}) \\
\dot{Q}_{loss} = \dfrac{\sigma A_a (T_a^4 - T_{ci}^4)}{\dfrac{1}{\varepsilon_c} + \dfrac{1-\varepsilon_e}{\varepsilon_e}\left(\dfrac{D_a}{D_{ci}}\right)} + \dfrac{2.425\, k_{ann}(T_a - T_{ci})\left(\dfrac{PrRa}{0.861+Pr}\right)^{\frac{1}{4}} L}{\left(1 + \left(\dfrac{D_a}{D_{ci}}\right)^{\frac{3}{4}}\right)^{\frac{5}{4}}} + N_{HCE}(T_{base} - T_{air})\sqrt{\bar{h}_b P_b k_b A_{cs,b}} \\
\dot{Q}_{loss} = \dfrac{2\pi k_e L (T_{ci} - T_{co})}{\ln\left(\dfrac{D_{co}}{D_{ci}}\right)} + N_{HCE}(T_{base} - T_{air})\sqrt{\bar{h}_b P_b k_b A_{cs,b}} \\
\dot{Q}_{loss} = h_{sa} A_{co}(T_{co} - T_{air}) + \varepsilon_e \sigma A_{co}(T_{co}^4 - T_{sky}^4) + N_{HCE}(T_{base} - T_{air})\sqrt{\bar{h}_b P_b k_b A_{cs,b}} \\
\dot{Q}_{loss} = L \pi D_a U_L (T_a - T_{air}) \\
F_R = \dfrac{\dot{m}_f c_{p,f}}{\pi D_a L U_L}\left[1 - exp\left(-\dfrac{\pi D_a L U_L F'}{\dot{m}_f c_{p,f}}\right)\right] \\
F' = \dfrac{U_L^{-1}}{U_L^{-1} + h_f^{-1}} \\
h_f = \left[0.027 * \left(\dfrac{4\dot{m}_f}{D_a \pi \mu_f}\right)^{\frac{4}{5}} * Pr_f^{\frac{1}{3}}\right] * \dfrac{k_f}{D_a}
\end{cases}
$$

Unknown array: $[\dot{Q}_{use} \;\; \dot{Q}_{loss} \;\; T_a \;\; T_{co} \;\; T_{ci} \;\; T_f \;\; U_L \;\; F_R \;\; F' \;\; \dot{m}_f \;\; h_f]$;

Second system:

$$
\begin{cases}
\dot{Q}_{use} = F_R L W \left[\dot{Q}''_{conc} - \dfrac{\pi D_a}{W} U_L (T_{in} - T_{air})\right] \\
\dot{Q}_{use} = F' L W \left[\dot{Q}''_{conc} - \dfrac{\pi D_a}{W} U_L (T_f - T_{air})\right] \\
\dot{Q}_{use} = h_f L \pi D_a (T_a - T_f) \\
\dot{Q}_{use} = \dot{m}_f c_{p,f} (T_{out} - T_{in}) \\
\dot{Q}_{loss} = \dfrac{\sigma A_a (T_a^4 - T_{ci}^4)}{\dfrac{1}{\varepsilon_c} + \dfrac{1-\varepsilon_e}{\varepsilon_e}\left(\dfrac{D_a}{D_{ci}}\right)} + \dfrac{2.425\, k_{ann} (T_a - T_{ci}) \left(\dfrac{PrRa}{0.861 + Pr}\right)^{\frac{1}{4}} L}{\left(1 + \left(\dfrac{D_a}{D_{ci}}\right)^{\frac{3}{4}}\right)^{\frac{5}{4}}} + N_{HCE} (T_{base} - T_{air}) \sqrt{\bar{h}_b P_b k_b A_{cs,b}} \\
\dot{Q}_{loss} = \dfrac{2\pi k_e L (T_{ci} - T_{co})}{\ln\left(\dfrac{D_{co}}{D_{ci}}\right)} + N_{HCE} (T_{base} - T_{air}) \sqrt{\bar{h}_b P_b k_b A_{cs,b}} \\
\dot{Q}_{loss} = h_{sa} A_{co} (T_{co} - T_{air}) + \varepsilon_e \sigma A_{co} (T_{co}^4 - T_{sky}^4) + N_{HCE} (T_{base} - T_{air}) \sqrt{\bar{h}_b P_b k_b A_{cs,b}} \\
\dot{Q}_{loss} = L \pi D_a U_L (T_a - T_{air}) \\
F_R = \dfrac{\dot{m}_f c_{p,f}}{\pi D_a L U_L} \left[1 - exp\left(-\dfrac{\pi D_a L U_L F'}{\dot{m}_f c_{p,f}}\right)\right] \\
F' = \dfrac{U_L^{-1}}{U_L^{-1} + h_f^{-1}}
\end{cases}
$$

Unknown array: $[\dot{Q}_{use} \;\; \dot{Q}_{loss} \;\; T_a \;\; T_{co} \;\; T_{ci} \;\; T_f \;\; U_L \;\; F_R \;\; F' \;\; T_{out}]$;

The iterative method chosen has been the “Bisection Method”. This method is very well known for being very easy to implement and stable, ensuring the success of the operation, despite having quite restrictive assumptions.

4.4.1 – Bisection Method

Let $f : [a, b] \to \mathbb{R}$; $f \in C([a, b])$ and let $f(a)f(b) < 0$. Under these assumption then exists at least one value in the interval $[a, b]$ for which the function is null. A succession of intervals will be created $\{I_k\}_{k=0}^{\infty}$ with $I_0 = [a_0, b_0] \equiv [a, b]$ so that:

- $I_{k+1} \subset I_k$;
- $\alpha \in I_k, \; \forall k \geq 0$;
- $The\ width\ of\ I_k\ tends\ to\ zero\ when\ k \to +\infty$

At first we set:

$$I_0 = [a_0, b_0] = [a, b]$$

And we calculate the midpoint:

$$c_1 = \frac{a_0 + b_0}{2}$$

Se $f(c_1) = 0$ then $\alpha = c_{k+1}$, otherwise we set:

$$I_1 = [a_1, b_1] \equiv \begin{cases} a_1 = a_0 \quad b_1 = c_1 \quad if\ f(a_0)f(c_1) < 0 \\ a_1 = c_1 \quad b_1 = b_0 \quad if\ f(a_0)f(c_1) > 0 \end{cases}$$

Now, starting from $I_1 = [a_1, b_1]$ the same procedure is repeated.

By generalizing, at step *k*:

$$c_{k+1} = \frac{a_k + b_k}{2}$$

Se $f(c_{k+1}) = 0$ then $\alpha = c_{k+1}$, otherwise we set:

$$I_{k+1} = [a_{k+1}, b_{k+1}] \equiv \begin{cases} a_{k+1} = a_k \quad b_{k+1} = c_{k+1} \quad if\ f(a_k)f(c_{k+1}) < 0 \\ a_{k+1} = c_{k+1} \quad b_{k+1} = b_k \quad if\ f(a_k)f(c_{k+1}) > 0 \end{cases}$$

The succession of intervals I_k obtained automatically fulfills the first two conditions. About the third one we can say:

$$b_k - a_k = \frac{b_{k-1} - a_{k-1}}{2} = \frac{b_0 - a_0}{2^k}$$

Which means that the width of I_k tends to zero when $k \to +\infty$. The third condition is then fulfilled.

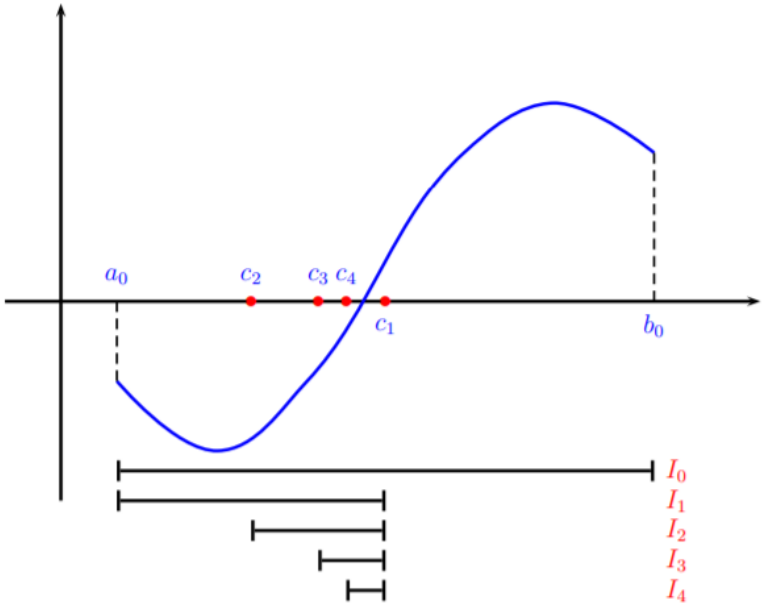

Figure 54 – Bisection Method graphics.

Because of roundoff errors what happens is that the condition $f(c_k) = 0$ never becomes satisfied. Because of this we must stop the process when we are satisfied by the result. A stop criteria must be set, it can be an absolute error with a tolerance ϵ:

$$b_k - a_k = \epsilon$$

We can understand from all of this, the importance of choosing a proper initial interval [a,b]. It must be enough wide to contain inside the mass flow rate value we are looking for but not too much because the method chosen is not that fast in fact of convergence speed and we want to save computational time.

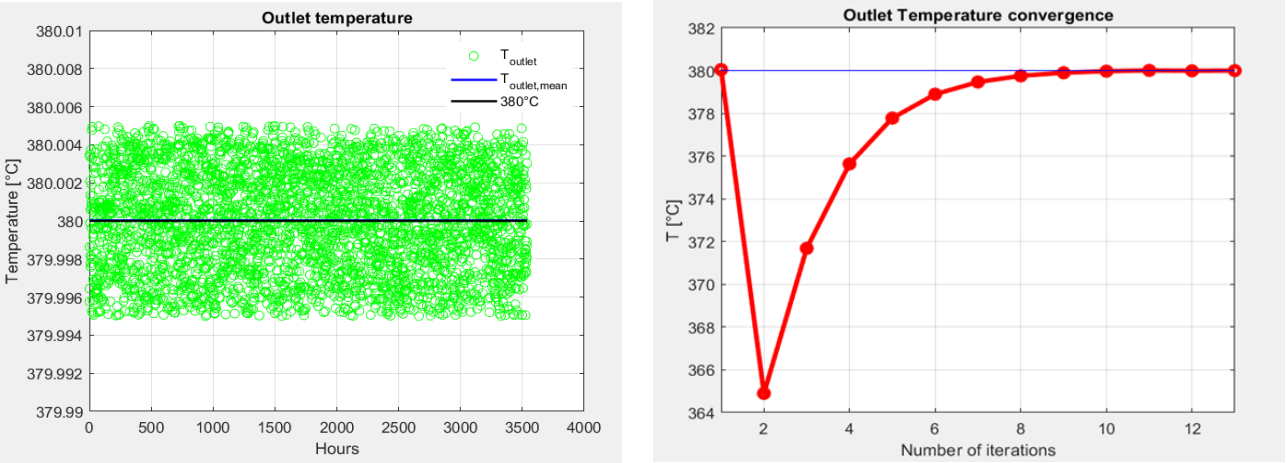

Figure 55 – (Left) Map distribution of the outlet temperatures (tolerance = 0.005). (Right) Temperature convergence.

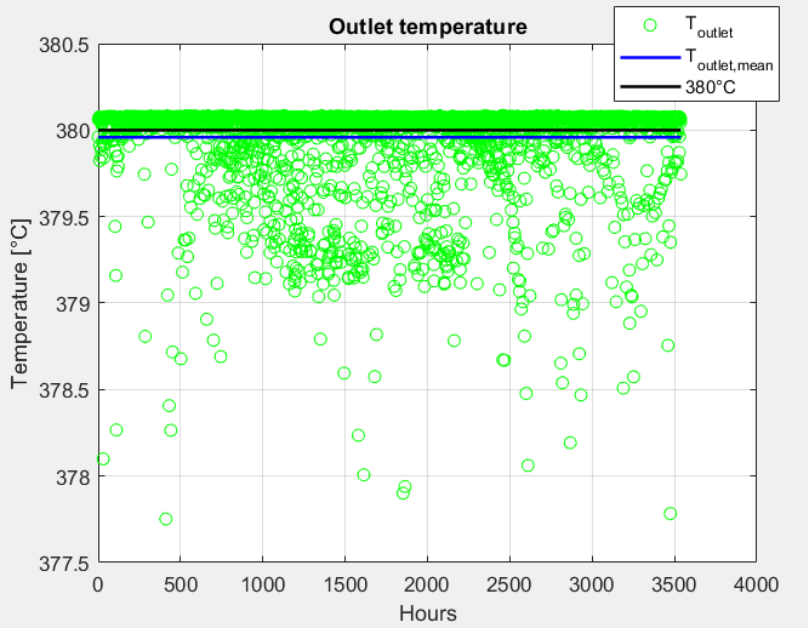

Figure 56 – First iteration temperatures map.

4.5 – Area estimation

The first objective of this Thesis work is the reflective area estimation. Once we know how to calculate the performances having the area as an input data, the best and straightforward way to estimate the area needed will be iterative.

The first thing to do is setting the width and length of the collectors (collector element), the number of parallel rows and the distance (spacing) between each of them. The transversal occupied space is:

$$Field\ Width = W + p * (N_{rows} - 1)$$

After this setup, a "`while`" cycle is used: the process starts by calculating the performance of a plant with only one element in each row, the code checks the result and if the power requirements are not satisfied the code will repeat the calculation adding one collector element in each row. The run finishes when all the requirements are satisfied.
A delicate aspect of this procedure is the choice of the collector element length. As mentioned before the longer an element is ,the more inaccurate the results will be but an excessive short collector length choice would lead to a very long computational time.

5 – Results

In this section the results of the simulation are shown. The main result achieved is the calculation of the needed reflective area, however, a further analysis about the main factors affecting the performances of a Parabolic Troughs (and every CSP) Field has been done and discussed.

5.1 – Input values

Here in this paragraph all the input values are listed:

Solar field geographic location:

$Latitude$	$Lat = 27.571$
$Longitude$	$Long = 35.537°$
$Standard\ meridian$	$L_{st} = 30°$

Collector parameters:

$Collector\ element\ length$	$L = 10\ m$
$Collector\ width$	$W = 5.774\ m$
$Focal\ length$	$f = 1.70\ m$
$Rim\ angle$	$\varphi_R = 80.67°$
$Absorber\ external\ diameter$	$D_a = 0.07\ m$
$Envelope\ outer\ diameter$	$D_{co} = 0.125\ m$
$Envelope\ inner\ diameter$	$D_{ci} = 0.119\ m$
$Glass\ thermal\ conductivity$	$k_{glass} = 1.14\ W/mK$
$Glass\ transmissivity$	$\tau_{glass} = 0.97$
$Glass\ emissivity$	$\varepsilon_{glass} = 0.88$
$Brackets\ effective\ diameter$	$d_{eff} = 2\ in = 0.0508\ m$
$Brackets\ square\ tubes\ (1in\ x\ 1in)$	$P_b = 0.2032\ m$
$Connection\ tabs\ \left(1in\ x \frac{1}{8in}\right) x2$	$A_{cs,b} = 1.613 * 10^{-4} m^2$
$Brackets\ thermal\ conductivity$ $(Plain\ carbon\ steel\ at\ 600\ K)$	$k_b = 48\ W/mK$
$Absorber\ (Solel\ UVAG\ Avg)\ absorptivity$	$\alpha_a = 0.955$
$Absorber\ (Solel\ UVAG\ Avg)\ emissivity$	$\varepsilon_a = 1.907 * 10^{-7}\mathrm{T}^2 + 1.208 * 10^{-4}\mathrm{T} + 6.282 * 10^{-2}$

$Mirror\ reflectivity\ (Flabeg\ Silver\ mirrors)$	$\rho_{refl} = 0.935$

HTF *Therminol VP-1* properties @340°C:

$HTF\ Density$	$\rho_f = 773\ kg/m^3$
$HTF\ Specific\ heat$	$c_{p,f} = 2425\ J/kgK$
$HTF\ Thermal\ conductivity$	$k_f = 0.0855\ W/mk$
$HTF\ Dynamic\ viscosity$	$\mu_f = 1.85 * 10^{-4}\ Pa\ s$

Air properties:

$Air\ Density$	$\rho_{air} = \frac{p_{air}}{R^*_{air} T_{air}}\ kg/m^3$
$Air\ Specific\ heat$	$c_{p,air} = 1006.5\ J/kgK$
$Air\ Thermal\ conductivity$	$k_{air} = 10^{-11} T_{air}^3 - 5 * 10^{-8} T_{air}^2 + 10^{-4} * T_{air} + 0.0003\ W/mk$
$Air\ Dynamic\ viscosity$	$\mu_{air} = 0.216 * 10^{-6} * T_{air}^{0.78}\ Pa\ s$

Annulus Hydrogen properties:

$H_2\ Density$	$\rho_{H_2} = \frac{p_{ann}}{R^*_{H_2} T_{ann}}\ kg/m^3$
$H_2\ Specific\ heat$	$c_{p,H_2} = 14550\ J/kgK$
$H_2\ Thermal\ conductivity$	$k_{H_2} = 0.315\ W/mk$
$H_2\ Dynamic\ viscosity$	$\mu_{H_2} = 0.18 * 10^{-6} * T_{ann}^{0.68}\ Pa\ s$
$Annulus\ pressure$	$p_{ann} = 700\ Pa$

5.2 – Area needed calculation

The main result is the area needed for the Solar Field.
Here the power requirements are reported again:

- $\dot{Q}_{use} = 3\ MW : 58\%\ of\ the\ year$
- $\dot{Q}_{use} = 4.5\ MW : 23\%\ of\ the\ year$

Several simulations has been run for this purpose, in order to understand which is the best tracking strategy to adopt in the current case and how the disposition and the movement of the collector affects the performances of the field. The needed area in both case (two tracking strategies) has been calculated.
A collector element length of 10 m has been chosen since is a good trade off between the calculation time and the accuracy achieved.
We are looking for the optimal disposition which satisfies the requirement and, at the same time, fits in the given space. As mentioned before a reduction of the distance between each row leads to a bigger influcence by the shading and a loss in the annual energy yield.

North-South axis strategy:

When this strategy is adopted, looking at the field, the collector rows are disposed vertically along the longer side of the rectangle.

The code returned as result:

Name	Value
Number of parallel rows	10
Spacing distance	$11.5\ m$
North - South extension	$160\ m$
East - West extension	$109.3\ m$
Reflective area needed	$9238\ m^2$
Average Useful power	$3.60\ MW$
Average Lost power	$0.41\ MW$
3 MW working time percentage	$69.36\ \%$
4.5 MW working time percentage	$28.02\ \%$
Average Thermal efficiency	0.88
Average Field mass flow rate	$18.67\ kg/s$
Annual energy collected	$1.221 * 10^7\ kWh$

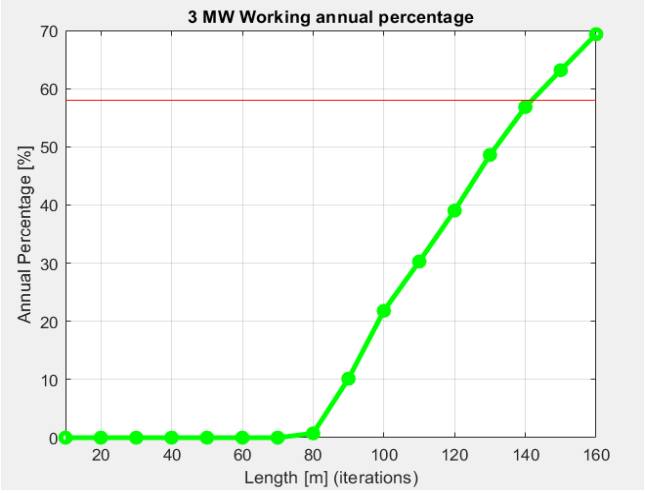

Figure 57 – North-South axis tracking strategy. (Left) 3 MW annual percentage at each iteration. (Right) 4.5 MW annual percentage at each iteration.

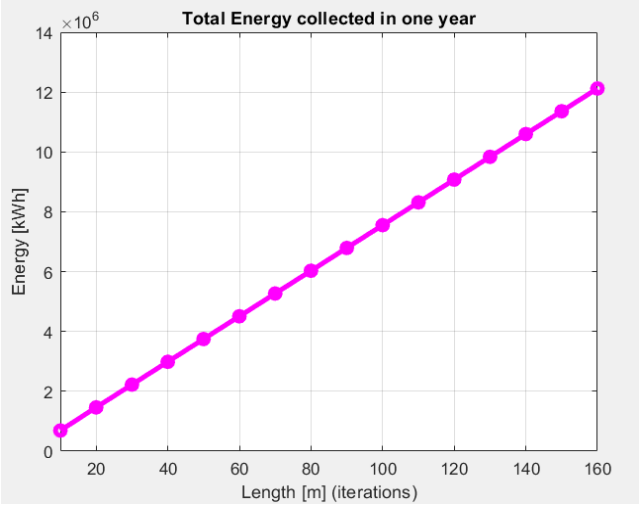

Figure 58 – North-South axis tracking strategy. (Left) Total energy collected in one year at each iteration. (Right) Average useful power at each iteration.

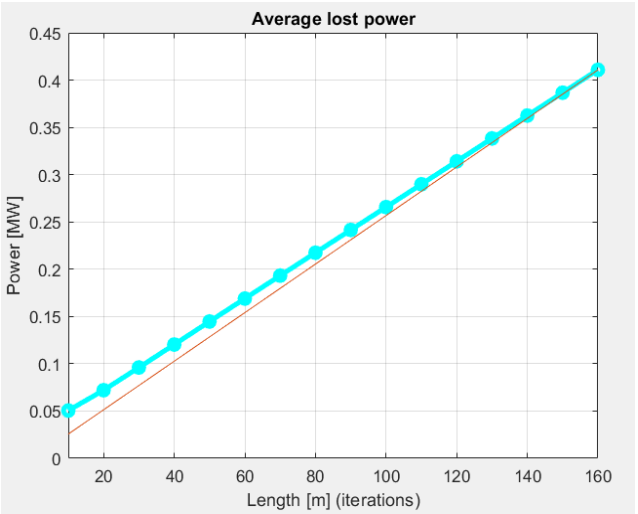

Figure 59 – North-South axis tracking strategy. (Left) Average lost power at each iteration. (Right) Average thermal efficiency at each iteration.

The 4.5 MW requirement turned out to be the most strict, indeed, the other one was satisfied with one less iteration.
Useful and Lost powers grow up almost linearly by increasing the length of each row, this can be explained quite easily:

$$\dot{Q}_{use} = A_{field}\ \dot{Q}''_{conc}\ \eta_{field}$$

$\dot{Q}''_{conc}$ of course doesn't change by increasing the area and so η_{field}. In particular:

$$\eta_{field} = \eta_{opt}\ \eta_{th}\ K(\theta)\ \eta_{sh}$$

In this equation only η_{th} changes a little: it slight increases as the area does the same. Indeed, this is the reason behind the little deviation from linearity.

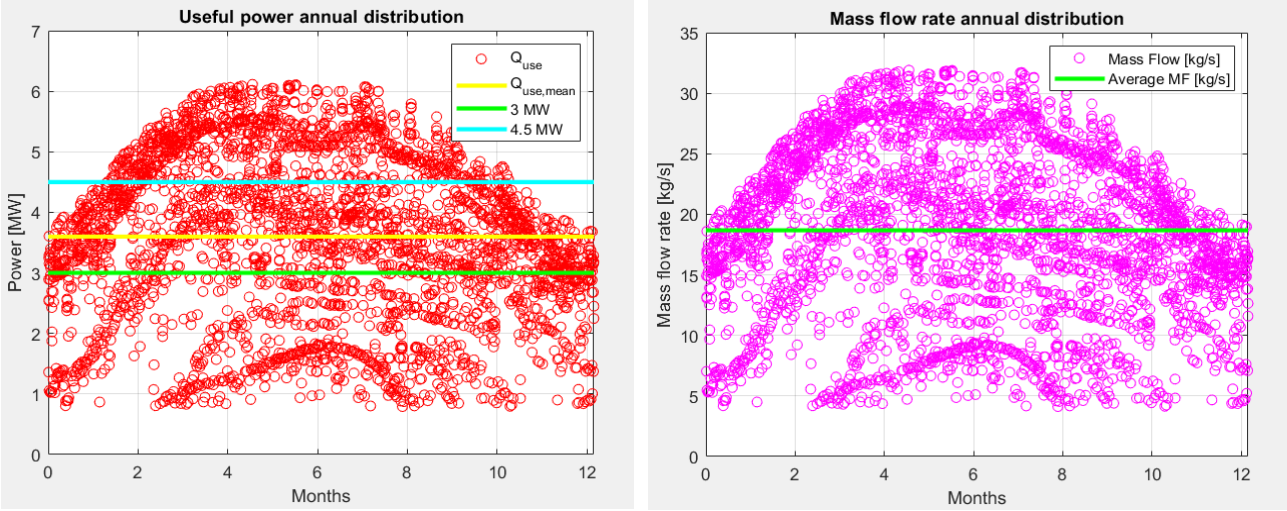

Figure 60 – North-South axis tracking strategy. (Left) Annual Useful power distribution. (Right) Annual mass flow rate distribution.

The distributions of the mass flow rate and of the useful power looks the same just because they are linearly correlated (since η_{th} is almost costant with $\dot{m}_f$). The shape of the distribution reflects the features of the tracking strategy used: according to the Sun Path Diagram, the Sun can be found closer to the E-W horizontal line in the summer rather than in the winter, thus most of the energy will be collected in that period. Overall, we could say it is a "daily consistent method" because $cos(\theta)$ doesn't decrease under certain values (the worst case is during winter time).

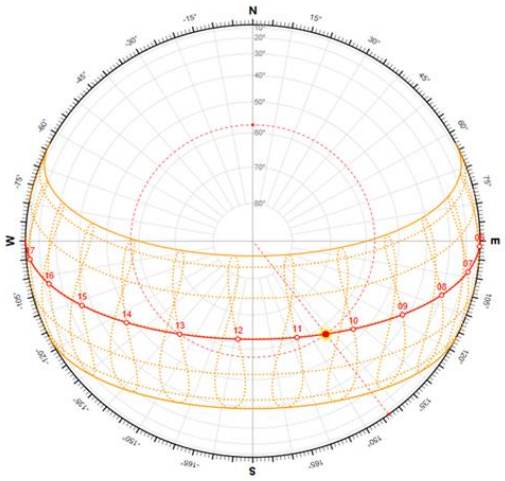

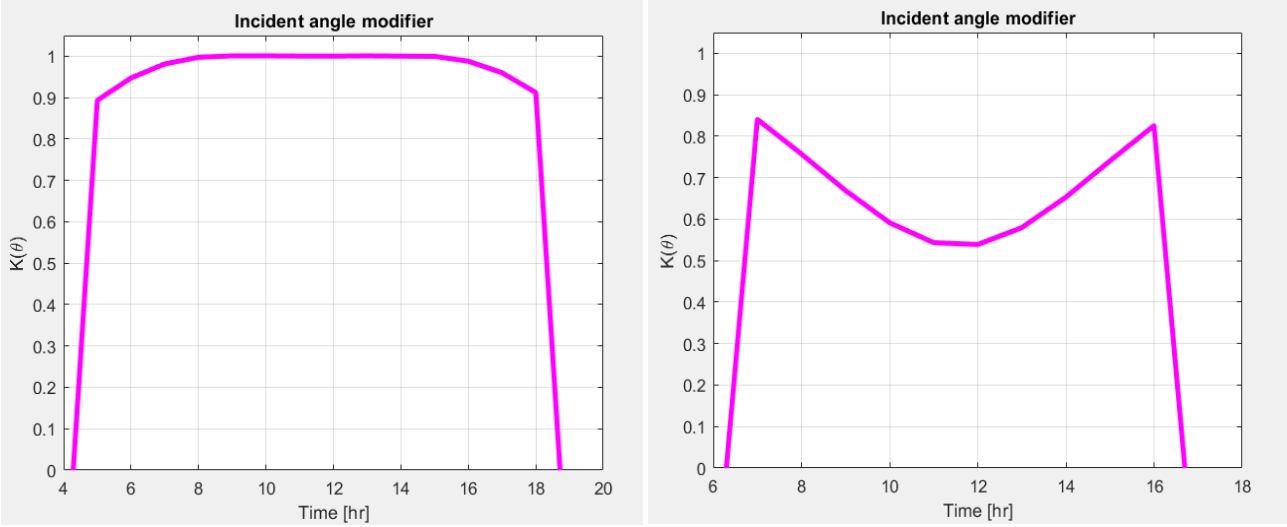

Figure 61 – Incident angle modifier, North-South axis tracking. (Left) 21st June. (Right) 21st December.

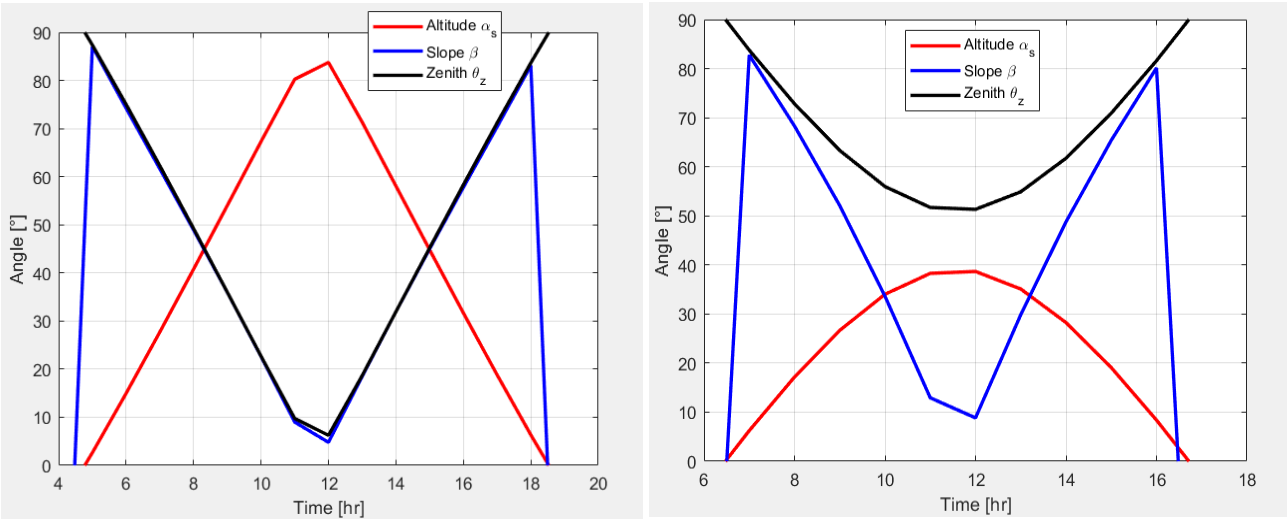

Figure 62 – Altitude angle, Slope and Zenith angle, North-South axis tracking. (Left) 21st June. (Right) 21st December.

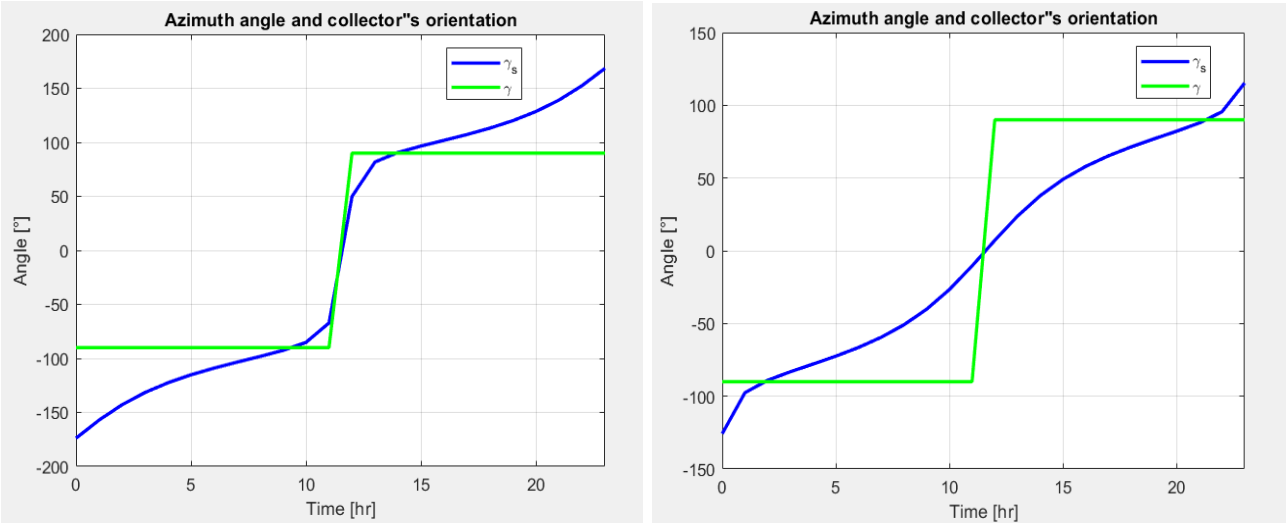

Figure 63 – Azimuth angle and collector orientation, North-South axis tracking. (Left) 21st June. (Right) 21st December.

Figures of merit are calculated:

- $Annual\ energy\ collected\ per\ unit\ reflective\ surface = \frac{1.212*10^7 \frac{kWh}{yr}}{9238\ m^2} = 1312 \frac{kWh}{m^2\ yr}$
- $Total\ annual\ energy\ from\ DNI = 2168 \frac{kWh}{m^2\ yr}$
- $Field\ efficiency = \frac{1312}{2168} = 0.60$
- $Reflective\ area\ per\ unit\ power = \left(1312 \frac{kWh}{m^2\ yr}\ \frac{1}{2974}\frac{yr}{h} * \frac{1}{10^3}\frac{MW}{kW}\right)^{-1} = 2266 \frac{m^2}{MW_{th}}$

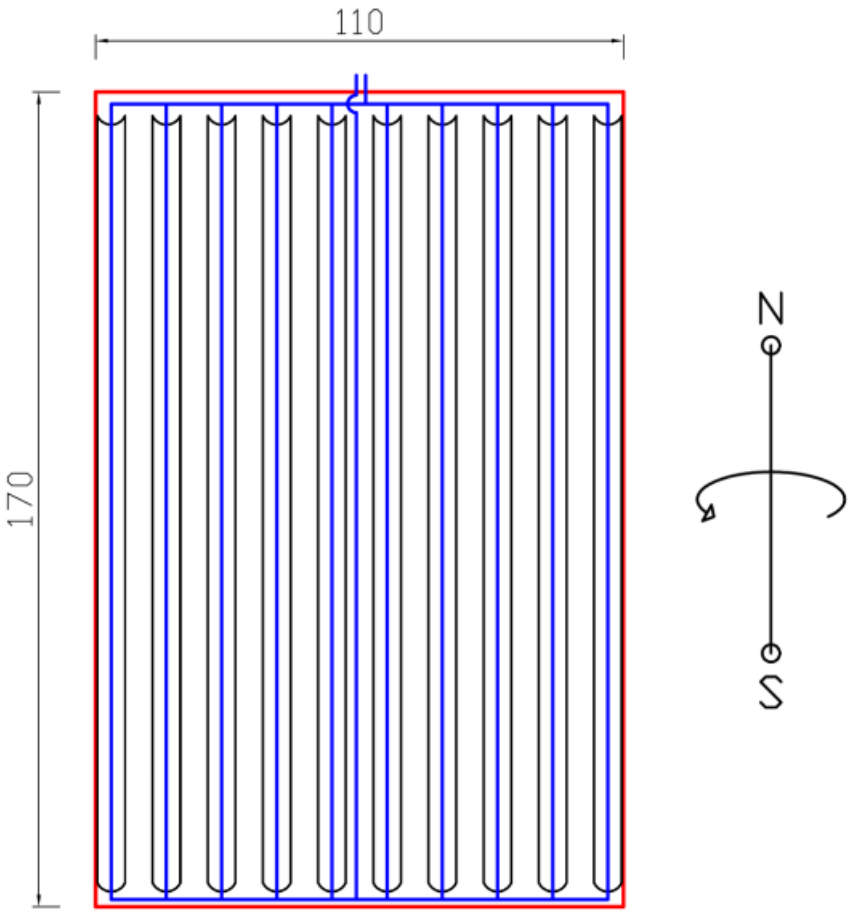

Figure 64 –North-South axis tracking strategy, final field configuration.

East-West axis strategy:

When this strategy is adopted, looking at the field, the collector rows are disposed horizontally along the shorter side of the rectangle.

The code returned as result:

Name	Value
Number of parallel rows	13
Spacing distance	$13.5\ m$
North - South extension	$167.77\ m$
East - West extension	$110\ m$
Reflective area needed	$8257\ m^2$
Average Useful power	$3.25\ MW$
Average Lost power	$0.38\ MW$
3 MW working time percentage	$58.54\ \%$
4.5 MW working time percentage	$27.24\ \%$
Average Thermal efficiency	0.87
Average Field mass flow rate	$16.94\ kg/s$
Annual energy collected	$0.967 * 10^7\ kWh$

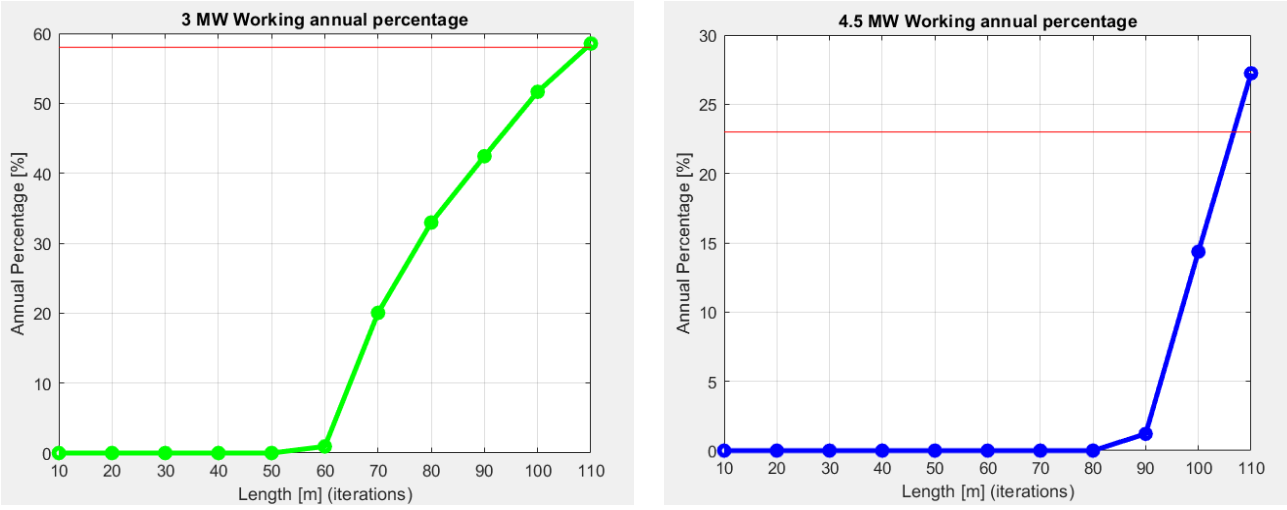

Figure 65 – East-West axis tracking strategy. (Left) 3 MW annual percentage at each iteration. (Right) 4.5 MW annual percentage at each iteration.

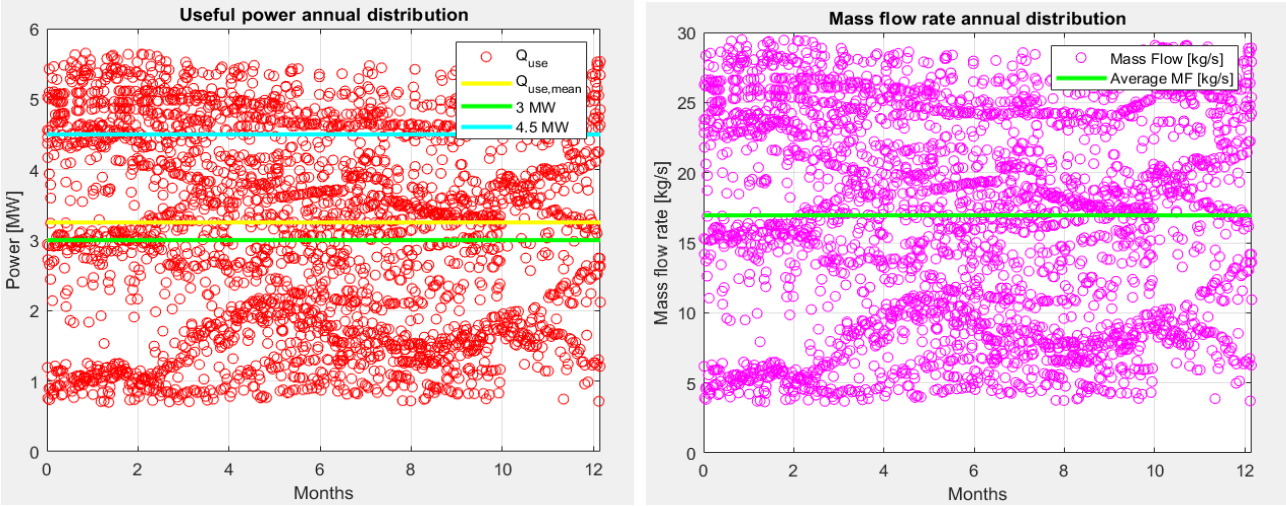

Figure 66 – East-West axis tracking strategy. (Left) Annual Useful power distribution. (Right) Annual mass flow rate distribution.

This time both the requirements are equally strict. The Useful Power scattered distribution looks more uniform with respect to the previous one although being less dense, especially in the summer time. This is happens mainly because the collectors point, most of the time, in the southward direction varying its slope between the horizon and the zenith. This means that a value of $\cos(\theta) = 1$ will be obtained for sure once per day, at noon (between 11 and 12 a.m.) to be precise, on the contrary the field won't be able to collect big amounts of energy the closer we get to the dawn and sunset ($\cos(\theta) \to 0$).

With all this said, we can say this is a "yearly consistent method" because this behaviour is constant during the year (it behaves slightly better in the winter time). Everything else works exactly like the other case, no difference has been detected in efficiencies and trends.

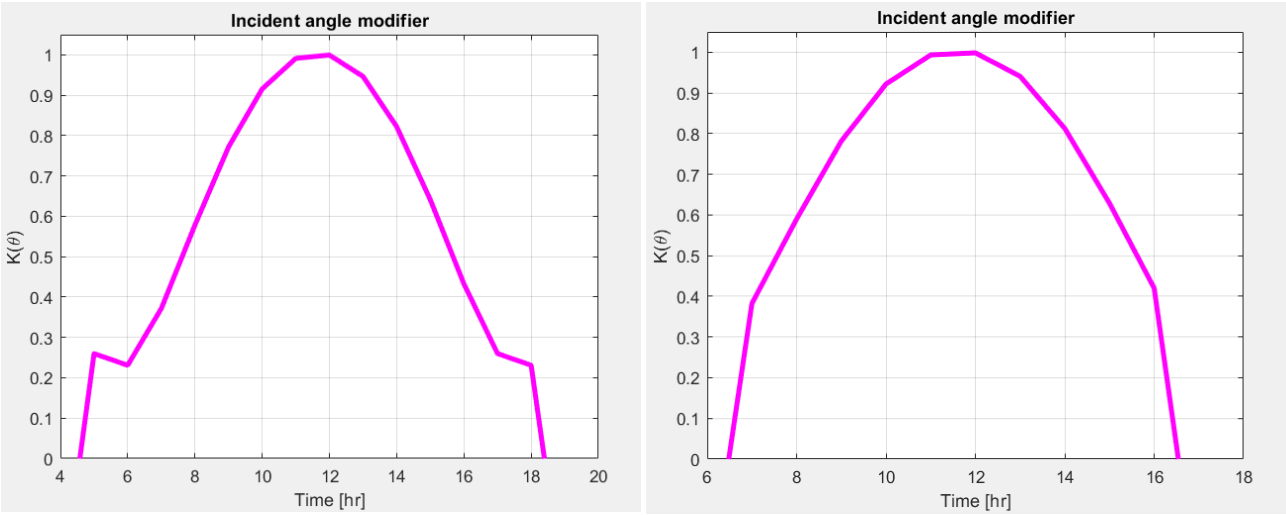

Figure 67 – Incident angle modifier, East-West axis tracking. (Left) 21st June. (Right) 21st December.

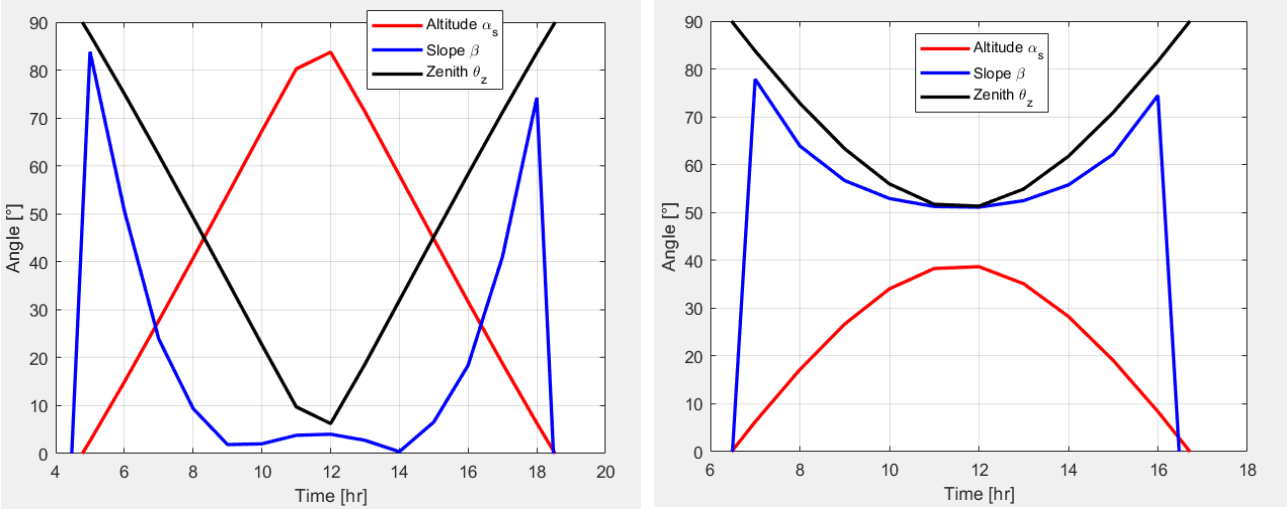

Figure 68 – Altitude angle, Slope and Zenith angle, East-West axis tracking. (Left) 21st June. (Right) 21st December.

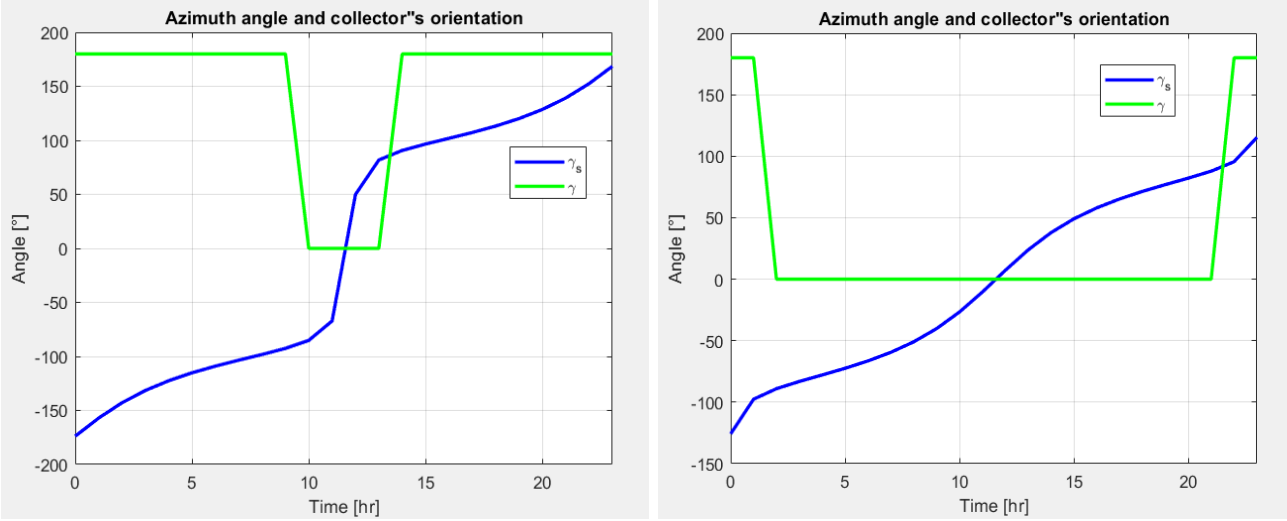

Figure 69 – Azimuth angle and collector orientation, East-West axis tracking. (Left) 21st June. (Right) 21st December.

Figures of merit:

- $Annual\ energy\ collected\ per\ unit\ reflective\ surface = \frac{0.967*10^7 \frac{kWh}{yr}}{8257\ m^2} = 1171 \frac{kWh}{m^2\ yr}$
- $Field\ efficiency = \frac{1171}{2168} = 0.54$
- $Reflective\ area\ per\ unit\ power = \left(1171 \frac{kWh}{m^2\ yr}\ \frac{1}{2974}\frac{yr}{h} * \frac{1}{10^3}\frac{MW}{kW}\right)^{-1} = 2540 \frac{m^2}{MW_{th}}$

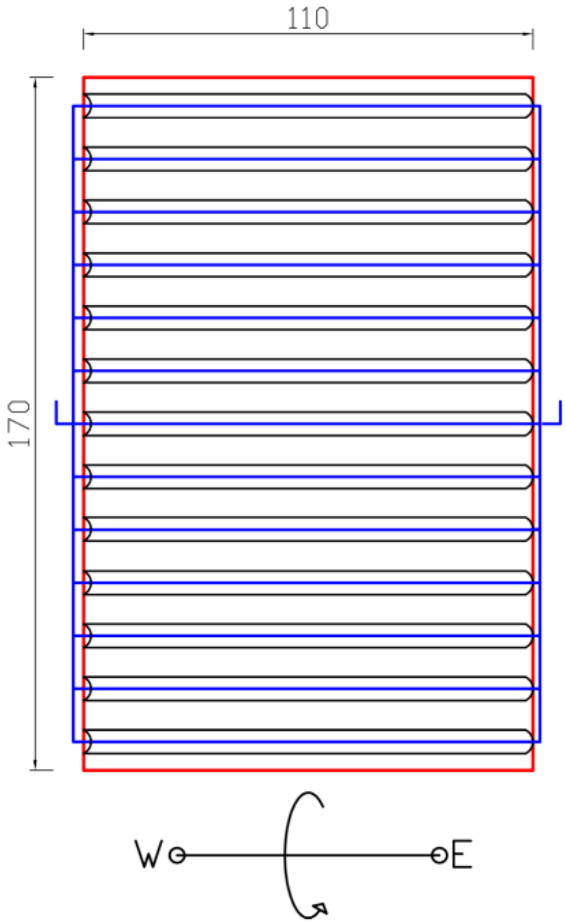

Figure 70 – East-West axis tracking strategy, final field configuration.

5.2.1 – Comparison between tracking strategies

In this small paragraph the two strategies will be compared. Most of the reasons behind the trends has been already explained in the previous paragraph but no mention on which is the best strategy has been done.
The figures of merit are now compared in a table:

Figure of merit	*North-South axis*	*East-West axis*
Specific annual energy	$1312\ kWh/m^2/yr$	$1171\ kWh/m^2/yr$
Field efficiency	0.60	0.54
Specific reflective area	$2266\ m^2/MW_{th}$	$2540\ m^2/MW_{th}$

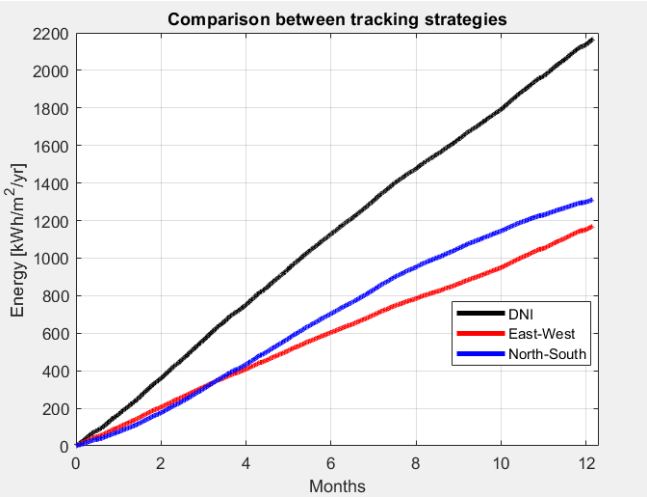

Figure 71 – (Left) Comparison of the specific energy yield throughout the year. (Right) Annual DNI distribution.

There is no unique answer to the question, because the smaller area satifying the requirements is obtained with the East-West axis strategy, however the table above speaks clearly about the better efficiency of the North-South axis strategy. This is due most likely to the location of the field on the map: it is found quite close to the equator and this makes the North-South method very reliable, allowing a bigger annual energy yield (with equal areas).

5.3 – Losses estimation

Here a detailed analysis of thermal losses is shown. The code solved is the one corresponding to the North-South tracking strategy simulation. The thermal scheme is reported again.

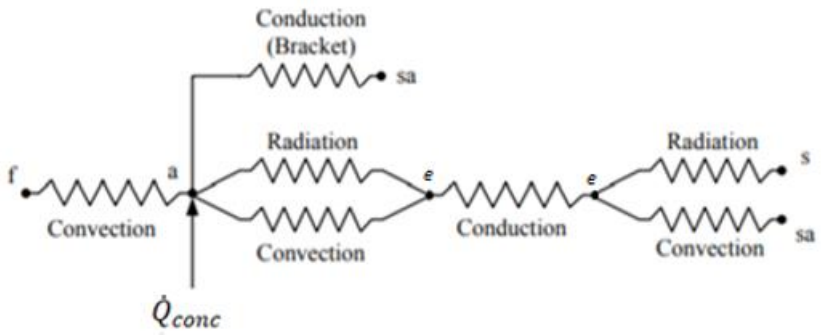

The following balance equation are valid:

$$\dot{Q}_{loss} = \dot{Q}_{cond-brackets} + \dot{Q}_{a-e,conv} + \dot{Q}_{a-e,rad}$$

$$\dot{Q}_{loss} = \dot{Q}_{cond-brackets} + \dot{Q}_{e,cond}$$

$$\dot{Q}_{loss} = \dot{Q}_{cond-brackets} + \dot{Q}_{e-s,rad} + \dot{Q}_{e-sa,conv}$$

It is very interesting the estimation of each of this components. We can expect a pretty high numerical value of the radiation losses between the absorber surface and the glass cover inner surface (sure thing as the other two components of $\dot{Q}_{loss}$ are expected to be very low). The annual average of each term is calculated:

Absorber – Envelope inner surface	***Envelope inner - outer surface***	***Envelope outer surface - Sky/Surrounding air***
$\dot{Q}_{cond-brackets} = 36564\ W$		
$\dot{Q}_{a-e,rad} = 360340\ W$	$\dot{Q}_{e,cond} = 375236\ W$	$\dot{Q}_{e-s,rad} = 95746\ W$
$\dot{Q}_{a-e,conv} = 14892\ W$		$\dot{Q}_{e-sa,conv} = 279490\ \mathrm{W}$

$$\overline{\dot{Q}_{loss}} = 0.41\ MW$$

As expected the radiative losses in the annulus are the biggest but the real interesting thing here are the losses by convection from the glass envelope to the surrounding, they are three times the amount of the radiative ones to the sky.

If we assume : $T_{co} = 320\ K$; $T_{air} = 297\ K$; $W_S = 3.6\ m/s$

We obtain, for the convection:

$$h_{sa} \approx 23\ W/m^2K.$$

For the radiation, instead:

$$\varepsilon_{glass}\sigma\left(T_{co}^2 + T_{sky}^2\right)\left(T_{co} + T_{sky}\right) \approx 6\ W/m^2K$$

Another predictable result is the increasing trend of the thermal losses along the field length because of the contextual temperature difference increase. For the same reason, the useful energy decreases.

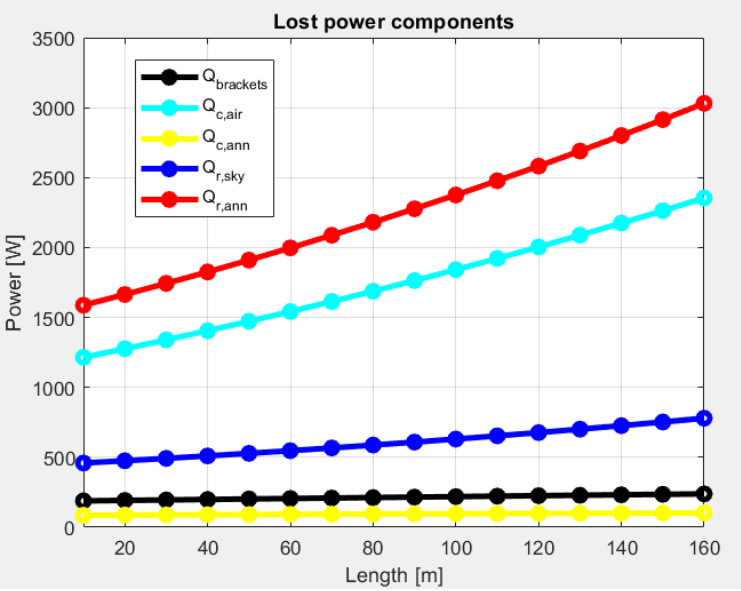

Figure 72 – Components of the lost power trends along the collector length.

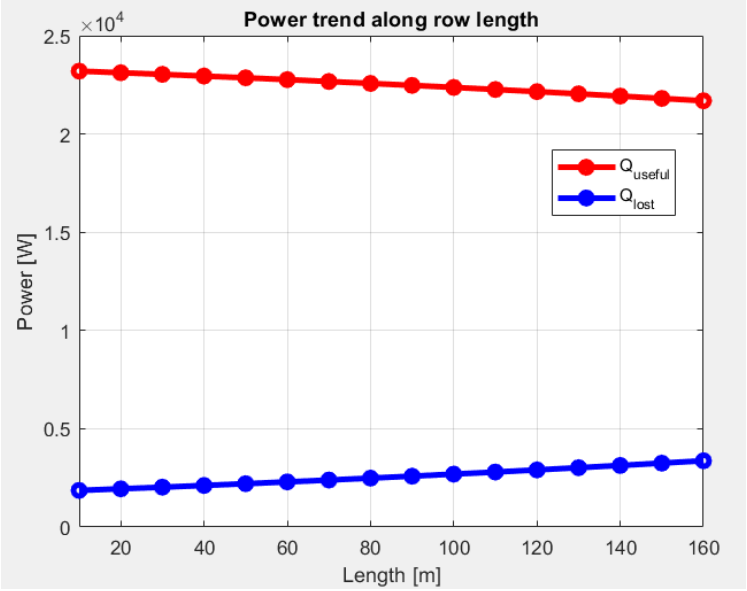

Figure 73 – Useful and lost power trends along the collector length.

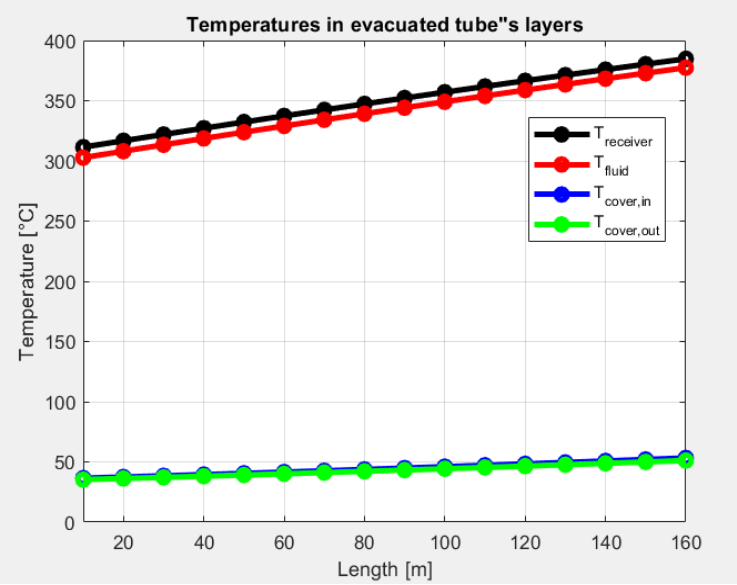

Figure 74 – Layer temperatures trends along the collector length.

5.4 – Spacing sensitivity analysis

The effect of the spacing on the energy is another key point of this Thesis work. It is very useful to understand how close two rows can be positioned without being affected heavily by the shading phenomenon. The analysis has been made by changing the distance between two rows parametrically. This study has been done again by comparing the effects of the two tracking strategies. The layout input data are the ones obtained by the previous sizing calculations.

	North-South axis	East-West axis
Number of rows	10	13
Coll. length	160 m	110 m
Spacing	11.5 m	13.5 m

North-South axis strategy:

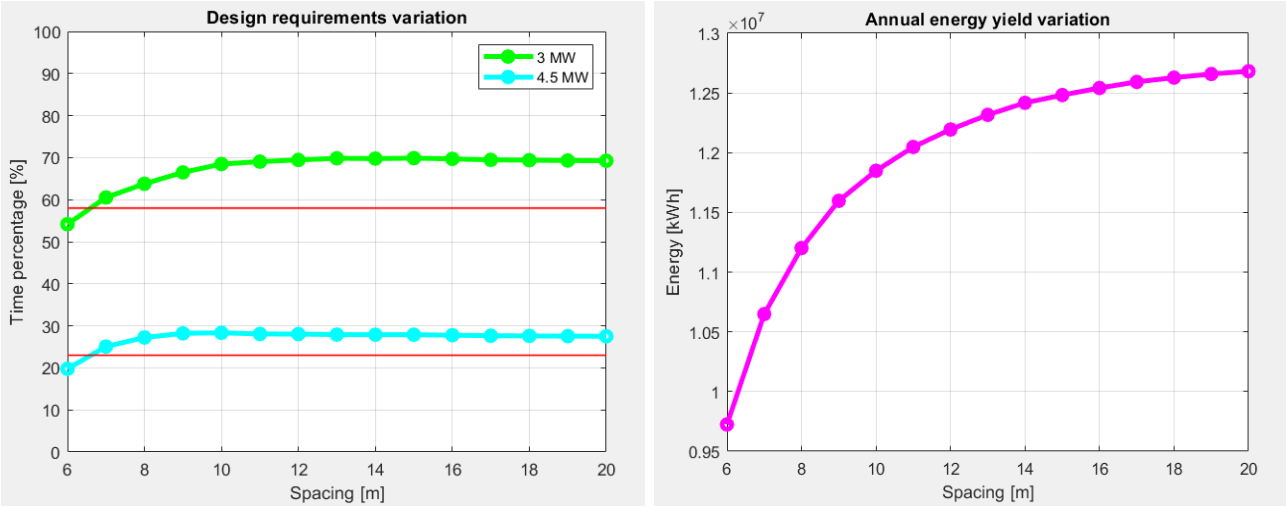

Figure 75 – North-South axis tracking strategy. (Left) Design requirements spacing analysis. (Right) Annual energy yield spacing analysis.

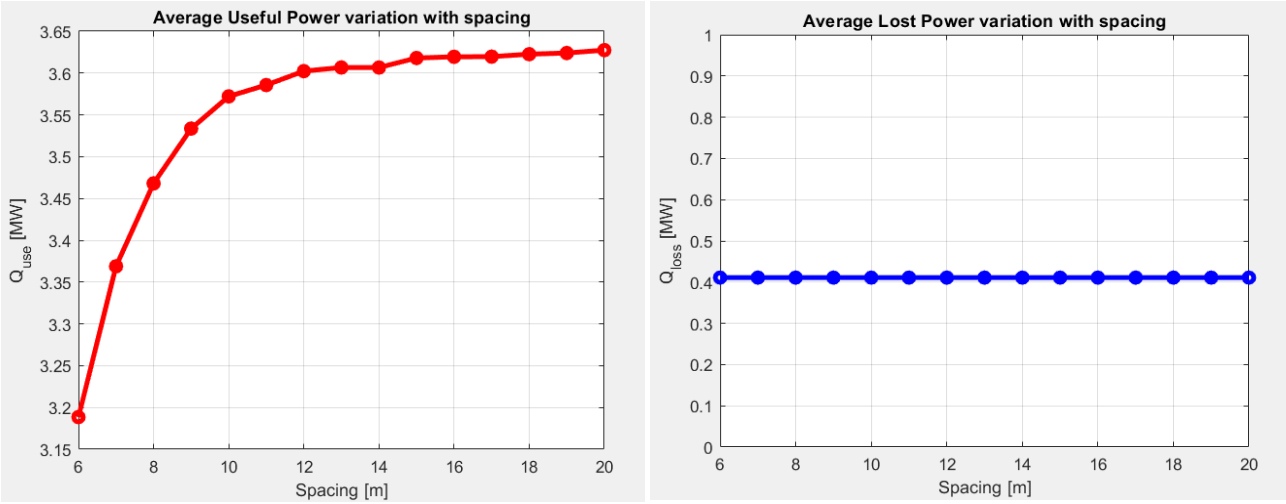

Figure 76 – North-South axis tracking strategy. (Left) Average Useful power spacing analysis. (Right) Average Lost power spacing analysis.

Extension [m]	*60*	*69*	*78*	*87*	*96*	*105*	*109*	*114*	*123*	*132*	*141*	*150*	*159*	*168*	*177*	*186*
Spacing [m]	*6*	*7*	*8*	*9*	*10*	*11*	*11.5*	*12*	*13*	*14*	*15*	*16*	*17*	*18*	*19*	*20*

As expected, by increasing the distance between each row, the shading phenomenon affects the system less and less and, obviously, there is no effect on the thermal losses. Regardless the distance,

if the Sun is about to set only the first row will receive energy, therefore increasing the spacing too much will not return a linear energy yield.

Of course, as expected, the thermal losses don't change at all by increasing the spacing, indeed, they only depend on the exchange surface, temperature and wind speed. A interesting results to highlight is the working time percentage at *4.5 MW*: it appears to be weakly affected by the spacing variation. The reason is easily explainable: we must remember that majority of the daily values of the useful power is absorbed at the noon, which is the time when shading doesn't exist.

East-West axis strategy:

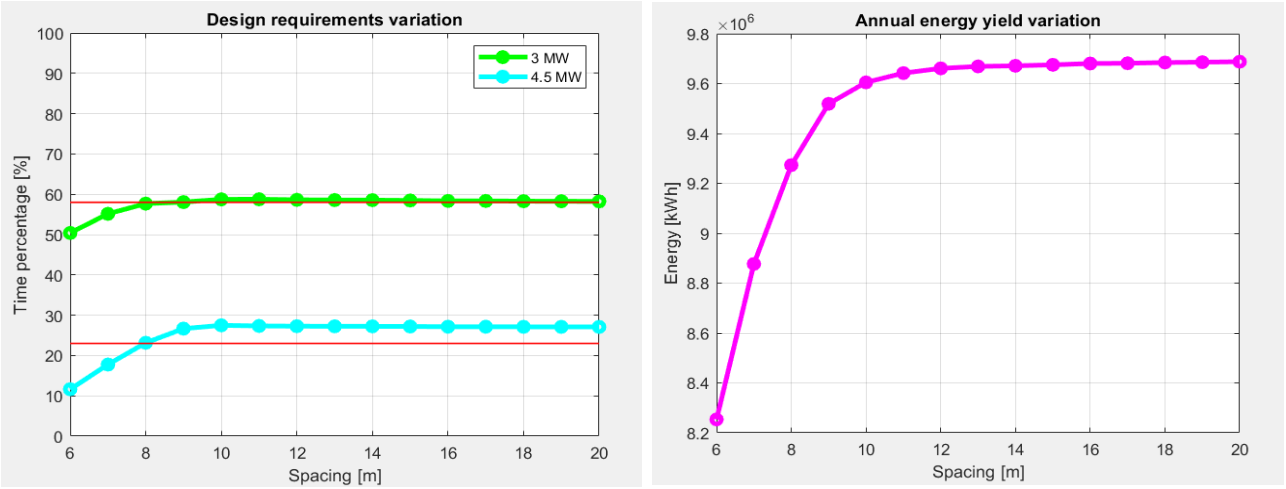

Figure 77 – East-West axis tracking strategy. (Left) Design requirements spacing analysis. (Right) Annual energy yield spacing analysis.

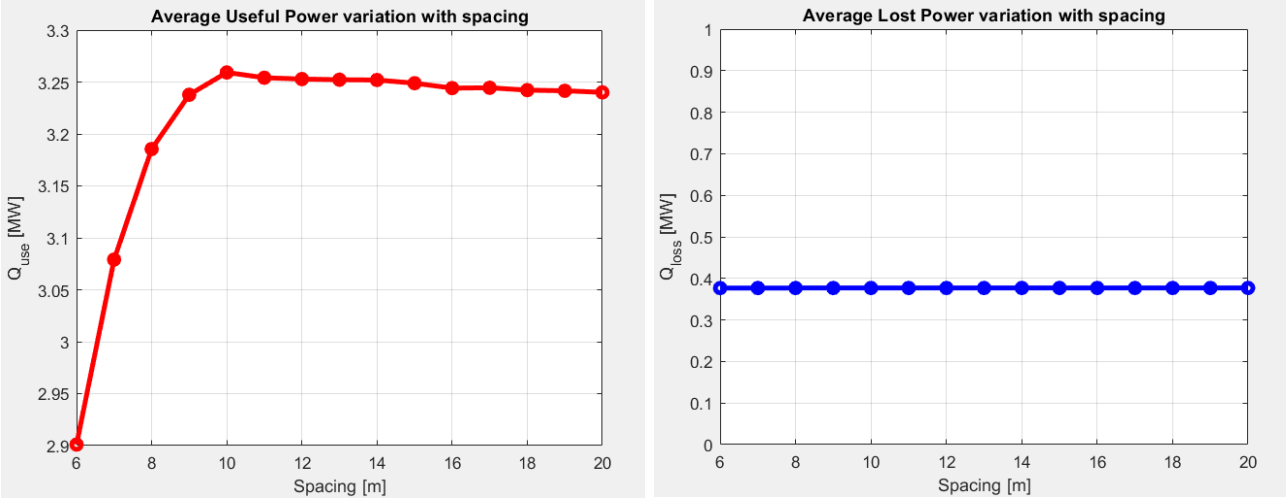

Figure 78 – East-West axis tracking strategy. (Left) Average Useful power spacing analysis. (Right) Average Lost power spacing analysis.

Extension [m]	*78*	*90*	*102*	*114*	*125*	*138*	*150*	*162*	*168*	*174*	*186*	*198*	*210*	*222*	*233*	*246*
Spacing [m]	*6*	*7*	*8*	*9*	*10*	*11*	*12*	*13*	*13.5*	*14*	*15*	*16*	*17*	*18*	*19*	*20*

For this case there are different kind of things to comment about. We must remember that the energy yield is pretty much uniform during the year, this means that (as we could see before) the system works equally as often at both powers (unlike in the other case) but of course 23% is easier to meet than 58%. Talking about the average useful power curve, unlike the previous one, it start decreasing when $p \geq 10\,m$ and this happens for the same reason as before: this field works homogeneously and the shading phenomenon affects the lowest power yields. As soon as the shading effect disappears, these yields appears and decrease the average of the higher power yields like *3 MW.*

5.5 – Validation of the results

In the end of this report the results obtained are compared with data taken from actual working parabolic troughs solar fields. The following table (from [22]), shows the main parameters of several SEGS solar fields (SEGS = Solar energy generating system) for electric energy production:

SEGS Plant	First year of operation	Net output [MWe]	Solar field outlet temperature [°C]	Solar field area [m^2]	Turbine efficiency [%]	Annual output [GWh_e]	Dispatchability provided by
I	1985	13.8	307	82 960	31.5/ n.a.	30	3 hours – thermal storage
II	1986	30	316	190,338	29.4/ 37.3	80	Gas fired superheater
III/IV	1987	30	349	230,300	30.6/ 37.4	93	Gas-fired boiler
V	1988	30	349	250,500	30.6/ 37.4	93	Gas-fired boiler
VI	1989	30	390	188,000	37.5/ 39.5	91	Gas-fired boiler
VII	1989	30	390	194,280	37.5/ 39.5	93	Gas-fired boiler
VIII	1990	80	390	464,340	37.6/ 37.6	253	Gas-fired heat transfer fluid heater
IX	1991	80	390	483,960	37.6/ 37.6	256	Gas-fired heat transfer fluid heater

These data have been processed in order to obtain the main figures of merit.

Solar Field site (California,USA)	Specific annual energy [$kWh_{th}/m^2/yr$]	Specific reflective area [m^2/MW_{th}]
Dagget (1985) I	1148	1894
Dagget (1986) II	1260	2116
Kramer Junction (1987) III/IV	1188	2610
Kramer Junction (1988) V	1092	2839
Kramer Junction (1989) VI	1257	2413
Kramer Junction (1989) VII	1243	2493
Harper Lake (1990) VIII	1449	2182
Harper Lake (1991) IX	1407	2275
NEOM North-South axis strategy	1312	2266
NEOM East-West axis strategy	1171	2540

By looking at the table, the results obtained in the current work appears similar and consistent. Unfortunately, since the available energy is unknown for the listed fields, it hasn't been possible to calculate the actual total efficiencies.

6 – Conclusions

A Matlab model for the estimation of the performances of a Parabolic Trough solar field has been developed. The results obtained reflect the real performances of such a Solar Field, taking into account to a good extent the main losses usually involved in the process. By using this model, the optimal reflective area has been as well estimated by analyzing the two main tracking strategy available. Very important in this regard has been the spacing parametrical analysis made on the variation of the main figures of merit. All the equation describing the phenomena reported have been discussed in detail.

Based on the climate data from NEOM a typical meteorological year (TMY) has been deduced, based on the years 2005-2017. A fundamental step has been the preliminary weather data analysis which allowed a better understand of the final results.

The Sun tracking model used gave consistent and realistic results, the East-West axis tracking strategy turned out to be the one to use to fulfill the requirement but the other one is the best according to the efficiency.

The model resulted to be useful to give a good feedback for the initial guess of the reflective area needed for the solar field currently in construction in NEOM, Saudi Arabia; some result was as well useful for the optimization of the final layout with the main purpose of maximize the collected energy during the year.

However the model considers every component of the system clean and working properly, with fixed requested temperature difference. In a practical working situation, these conditions are not always satisfied. Here possible further developments are listed for this model:

- Taking into account the effect on the performance of the field from dust and rain on the receiver/collector;
- Thermal storage could be included in the model, as well as time dependence and heat thermal losses calculation extended even for the thermal storage;
- Evaluation of different control strategies;
- Utilization of a safety coefficient for weather variability.

Acknowledgement

Now that my University studies are coming to an end some acknowledgement are necessary.
I would like to thank first of all my main supervisor, Professor Eliodoro Chiavazzo, for the opportunity given, allowing me to work in a foreign country. Of course a thank you goes as well to my Cranfield University supervisors: Professor Chris Sansom and Doctor Peter King, as they helped and supported me with this thesis work development during my stay in the United Kingdom.
I would like to thank also all my closest friends as their support was fundamental and decisive.
A “special” thank goes up to my English housemates Rylan and Hannah as they tried as much as they could to make me feel at home in very hard circumstances.

Last but not least I would like to thank all the negative and bad people I’ve met so far, after all it is because of them if this result has been achieved.

References

[1] J. A. Duffie, W.A. Beckman (2013). Solar Engineering of Thermal Processes, Fourth Edition. Hoboken, New Jersey: John Wiley and Sons.

[2] V.M. Sharma, J.K. Nayak, S.B. Kedare. Shading and available energy in a parabolic trough concentrator field. Solar Energy 90 (2013) 144-153.

[3] R. Forristall (2003). Heat Transfer Analysis and Modeling of a Parabolic Trough Solar Receiver implemented in Engineering Equation Solver. NREL/TP-550-34169.

[4] Incropera, DeWitt, Bergman, Lavine (2007). Fundamentals of Heat and Mass Transfer, Sixth Edition. New York, NY: John Wiley and Sons.

[5] S. T. Mohammad, H. H. Al-Kayiem, M. K. Assadi, O. Sabir, A. K. Khlief (2018). An integrated program of a stand-alone parabolic trough solar thermal power plant: Code description and test. Case Studies in Thermal Engineering 12 (2018) 26–37.

[6] Vasquez Padilla Ricardo, "Simplified Methodology for Designing Parabolic Trough Solar Power Plants" (2011). Graduate School Theses and Dissertations.

[7] K. Pottler, S. Ulmer, E. Lüpfert, M. Landmann, M. Röger, C. Prahl. Ensuring performance by geometric quality control and specifications for parabolic trough solar fields. Energy Procedia 49 (2014) 2170 – 2179.

[8] Iqbal, M., Solar Energy, 22, 87 (1979). ‘‘A Study of Canadian Diffuse and Total Solar Radiation Data — II Monthly Average Hourly Radiation.’’

[9] Iqbal, M., An Introduction to Solar Radiation, Academic, Toronto (1983).

[10] Temps, R. C. and K. L. Coulson, Solar Energy, 19, 179 (1977). ‘‘Solar Radiation Incident Upon Slopes of Different Orientations.’’

[11] Klucher, T. M., Solar Energy, 23, 111 (1979). ‘‘Evaluating Models to Predict Insolation on Tilted Surfaces.’’

[12] Lovegrove & Pye, 2012 Fundamental principles of concentrating solar power (CSP) systems (Book chapter), Woodhead.

[13] Fletcher, E. A., & Moen, R. L. (1977). *Hydrogen- and Oxygen from Water. Science, 197(4308), 1050–1056.*

[14] T. Politi. *Dispense di Calcolo Numerico*. Anno Accademico 2019/2020. Politecnico di Bari.

[15] Labban, A. H. (2016) Dust Storms Over Saudi Arabia: Temporal and Spatial Characteristics, Climatology and Synoptic Case Studies. PhD Thesis, RMIT University.

[16] Bendt P, Rabl A, Gaul HW, Reed KA. Optical analysis of line focus solar collectors. SERI/TR-34-092, Golden CO, 1979

[17] Dudley, V. E.; Kolb, G. J.; Mahoney, A. R.; et al. (December 1994). Test Results: SEGS LS-2 Solar Collector. SAND94-1884. Albuquerque, NM: SANDIA National Laboratories.

[18] Gnielinski, V. (April 1976). "New Equations for Heat and Mass Transfer in Turbulent Pipe and Channel Flow." International Chemical Engineering (16:2); pp. 359–363.

[19] Ratzel, A.; Hickox, C.; Gartling, D. (February 1979). "Techniques for Reducing Thermal Conduction and Natural Convection Heat Losses in Annular Receiver Geometries." Journal of Heat Transfer (101:1); pp. 108–113.

[20] Bejan, A. (1995). Convection Heat Transfer, Second Edition. New York, NY: John Wiley & Sons.

[21] S. Thappa, A. Chauhan, Y. Anand et al., Analytical comparison of two distinct receiver tubes of a parabolic trough solar collector system for thermal application, Materials Today: Proceedings, https://doi.org/10.1016/j.matpr.2020.04.257

[22] Price, H.; Lupfert, E.; Kearney, D.; Zarza, E.; Cohen, G.; Gee, R.; (May 2002). "Advances in Parabolic Trough Solar Power Technology." Journal of Solar Energy Engineering (Vol. 124); pp. 109–125.

[23] M.A. Geyer, R. Osuna, A. Esteban, W. Schiel (September 2003). "EUROTROUGH - Parabolic Trough Collector Developed for Cost Efficient Solar Power Generation". Conference SolarPACES.